

DIPLOMARBEIT

Geant4 Simulations for Ion CT Image Reconstruction

zur Erlangung des akademischen Grades

Diplom-Ingenieurin

im Rahmen des Studiums

Technische Physik

eingereicht von

Stefanie Kaser BSc

Matrikelnummer 01225146

ausgeführt am Atominstitut
der Fakultät für Physik der Technischen Universität Wien
in Zusammenarbeit mit dem Institut für Hochenergiephysik

Betreuung

Betreuer: Univ.Prof. Dipl.-Phys. Dr.rer.nat. Jochen Schieck

Mitwirkung: Dipl.-Ing. Dr.techn. Thomas Bergauer

Dipl.-Ing. Dr.techn. Albert Hirtl

Wien, am 10. Oktober 2019

(Unterschrift Verfasserin)

(Unterschrift Betreuer)



Die approbierte gedruckte Originalversion dieser Diplomarbeit ist an der TU Wien Bibliothek verfügbar.
The approved original version of this thesis is available in print at TU Wien Bibliothek.

Abstract

Ion therapy is used in many facilities throughout the world since it offers the possibility to selectively irradiate deep-seated tumours with accelerator-produced ions while healthy tissue can be spared. For accurate treatment planning it is essential to know the ion energy deposition per unit length (stopping power) inside the patient. One suitable method for achieving this is the ion Computed Tomography (CT). A large benefit of this method is that the same particle type can be used for the measurement of the stopping power inside the patient and patient treatment itself. This allows a higher accuracy in treatment planning and reduces range uncertainties which result from the calculation of the stopping power from imaging methods with other particles (such as photons).

For ion imaging, the setup usually consists of a tracking system to determine the ion entry and exit point to the patient and a calorimeter to measure the residual particle energy. Additionally, the ion path through the patient - which results from multiple Coulomb scattering - has to be estimated for accurate treatment planning. This can be done with different approaches like Straight Line (SL) or Most Likely Path (MLP). For the image reconstruction from ion path and residual energy, several different algorithms have been developed so far.

In this thesis, an overview of image reconstruction methods for ion CT will be given. Furthermore, data will be simulated using the Geant4 software framework. With these data, basic image reconstruction will be performed using a simple ion path estimate and an appropriate reconstruction algorithm. The algorithms are applied to simulated data and 3D reconstructed images are shown. Later these algorithms will be applied to data measured at MedAustron.

Zusammenfassung

Ionentherapie wird weltweit bereits in vielen Einrichtungen eingesetzt, da sie die Möglichkeit bietet, tief sitzende Tumore mit Ionen aus einem Beschleuniger zu bestrahlen und dabei das gesunde Gewebe zu schonen. Um die Planung für die Therapie möglichst exakt zu gestalten, ist eine genaue Kenntnis des Energieverlusts der Ionen pro Wegstrecke (Bremsvermögen, Stopping Power) innerhalb des Patienten nötig. Eine Möglichkeit diesen zu bestimmen, bietet die Ionen-Computertomographie (CT). Der Vorteil dieser Methode liegt daran, dass dieselbe Teilchenart sowohl für Bildgebung (Bestimmung der Stopping Power) als auch für die anschließende Therapie verwendet werden kann. Dadurch kann die Genauigkeit der Therapie verbessert werden, da Ungenauigkeiten durch Umrechnung von anderen Methoden mit anderen Teilchenarten (wie beispielsweise Photonen) vermieden werden.

Der Aufbau für die Bildgebung mit Ionen besteht üblicherweise aus einem Tracking-System um Ein- und Austrittspunkt des Ions zu bestimmen und aus einem Kalorimeter, das die verbleibende Energie des Ions am Ende des Aufbaus misst. Zudem muss der Pfad des Ions durch den Patienten, welcher durch mehrfache Coulombstreuung zustande kommt, abgeschätzt werden. Hierfür gibt es unterschiedliche Ansätze wie den Straight Line (SL) oder den Most Likely Path (MLP). Um ein Bild aus diesen Informationen zu generieren, wurden bereits einige unterschiedliche Algorithmen entwickelt.

In dieser Arbeit soll ein Überblick über bereits vorhandene Methoden zur Bildrekonstruktion für Ionen-CT gegeben werden. Zudem werden mithilfe des Software Frameworks Geant4 Simulationsdaten für eine einfache Ionen-CT erzeugt. Mit diesen Daten wird eine einfache Bildrekonstruktion durchgeführt, indem ein simpler Ansatz für den Ionenpfad und ein entsprechender Rekonstruktions-Algorithmus gewählt werden. Die resultierenden 3D-Bilder werden in dieser Arbeit gezeigt. Die Algorithmen, welche für diese Rekonstruktion verwendet werden, sollen künftig auch auf reale Daten angewandt werden, welche durch Messungen am MedAustron mit einem vorläufigen Aufbau für ein einfaches Ionen-CT gewonnen werden.

Contents

1	Introduction	5
2	Physical and mathematical background	8
2.1	Interactions of ions and matter	8
2.1.1	Bethe-Bloch equation	8
2.1.2	Range of ions in matter	12
2.1.3	Multiple Coulomb Scattering	12
2.1.4	Nuclear interactions	13
2.1.5	Bragg curves	13
2.2	Medical applications of ions	15
2.2.1	Cancer treatment with ions	15
2.2.2	Ion imaging	17
2.2.3	Tomographic equation and projection definition	19
2.3	Path estimates	21
2.4	Image reconstruction algorithms	23
2.4.1	Filtered-backprojection	24
2.4.2	Iterative techniques in image reconstruction	26
3	Methods and materials	30
3.1	MedAustron facility and experimental setup	30
3.2	Software frameworks	32
3.2.1	Geant4	32
3.2.2	ROOT	36
3.2.3	TIGRE	37
3.2.4	ImageJ	39
3.3	Reconstruction process	40
3.3.1	Experimental setup with Geant4	41
3.3.2	Generation of data	43
3.3.3	Creation of projections	43
3.3.4	Reconstruction in TIGRE	47
3.3.5	Analysis of reconstruction data	49
4	Results and discussion	52
4.1	Application of different algorithms in TIGRE	52
4.2	Different number of particles and projections	58
4.3	Determination of the stopping power	60
4.3.1	Phantoms made of one material	61
4.3.2	Phantoms made of multiple materials	65
4.4	Image reconstruction with carbon ions	69
5	Conclusion and Outlook	72

6 Acknowledgements	75
Appendix	77
Projection data	77
Variation of SART iterations	81
Variation of OS-SART iterations and block size	81
List of Figures	87
Acronyms	88
References	89

1 Introduction

According to the World Health Organization [1], cancer still counts as the second leading cause for global death. In 2018, the number of newly diagnosed cases was estimated to be 18.1 million, 9.8 million death cases were expected. Statistically, one in five men and one in six women develops cancer during their lifetime. Although the population of Europe only accounts for about 9% of the global population, 23.4% of the cancer cases and 20.3% of cancer deaths can be assigned to this geographical region [2].

The problem with cancer is that this term actually describes a large group of different diseases which can affect every part of the body. These diseases all have the rapid growth of abnormal cells in common; these cells can spread from their origin to other parts of the body and develop malignant tumours, the so-called metastases [1].

Although cancer appears in different forms, three treatment methods have become standard in the clinical application: surgery, chemotherapy and radiotherapy. Considering radiotherapy, the most common treatment is done with X-ray beams, which are directed at the tumorous area from different angles in order to achieve a high dose in that area and a lower dose in the adjoining healthy tissue. Other radiotherapy methods are far less common in clinical practice. However, the number of patients being treated with protons or heavy ions is steadily rising. Facilities who want to provide this treatment are in need of a complicated and expensive equipment in order to provide particles at the crucial energies and lead them to the patient. On the other hand, the typical dose deposition of the respective particles can be used for a more efficient therapy - a higher dose can be applied to the tumorous area without increasing the dose to the healthy tissue compared to X-rays (see Figure 1.1), which is a main advantage especially regarding deep-seated tumours [3].

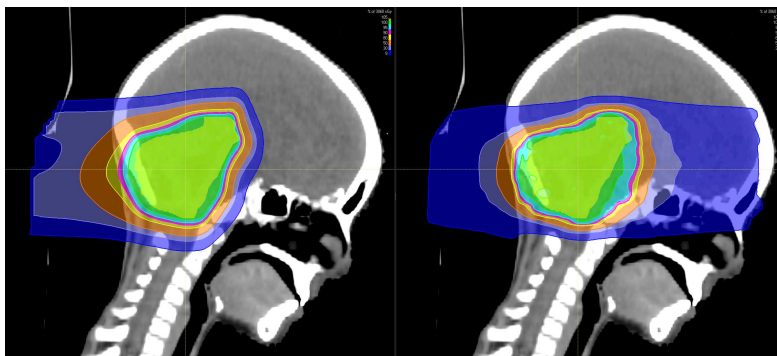


Figure 1.1: Dose distribution of proton radiotherapy (left) compared to X-ray radiotherapy (right) of a brain tumour [4].

For these reasons, there are already several facilities in Europe offering hadron radiotherapy, as it can be seen in Figure 1.2. Most of them offer therapy with protons, only a few of them use other ion types such as carbon ions.

Although radiotherapy with hadrons is already applied more often in clinical practice, the imaging with protons and heavy ions is still subject to research. This mainly comes

from the fact that - besides the costly equipment - the imaging with these particles is far more complicated than the conventional imaging process with photons since ions are subject to Multiple Coulomb Scattering (MCS) and therefore do not pass through matter on a straight path. On the other hand, the treatment planning of ion therapy with an X-ray CT results in the necessity of conversions and hence to range uncertainties. To make the treatment planning as accurate as possible it is therefore important to further investigate the ion imaging process. This especially gains importance when treatment planning includes a treatment near a sensitive area (e.g. optical nerve) that has to be irradiated or for children, where the probability of secondary cancer can be reduced with a more accurate treatment planning (i.e. lower dose to the healthy tissue is applied).

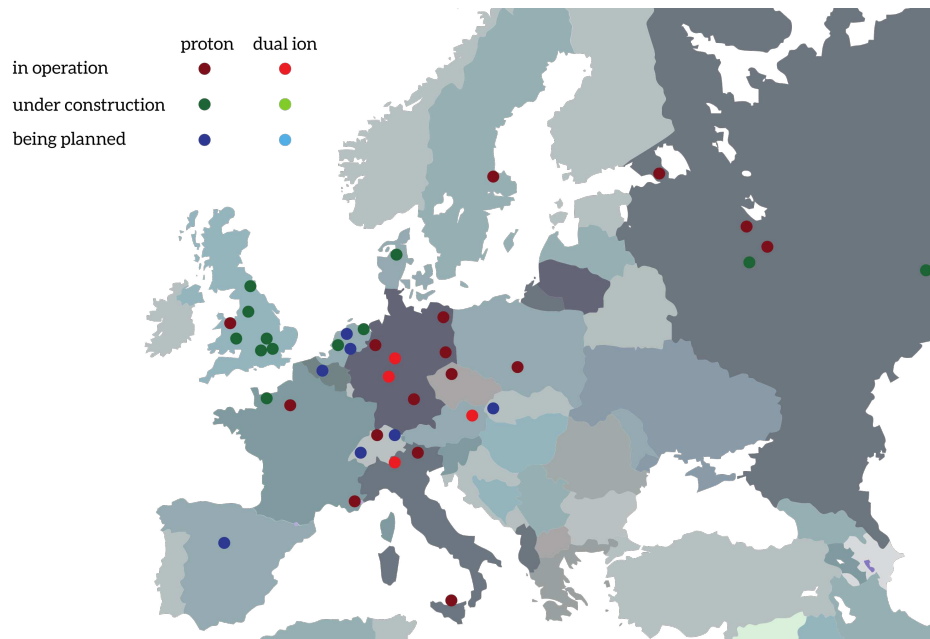


Figure 1.2: Hadron therapy facilities in Europe in 2016 [5].

The MedAustron ion beam [6] in lower Austria, which will be further described in Section 3.1, already offers radiotherapy. Furthermore it has an irradiation room for non-clinical research only. There, a setup of four detectors and a phantom has already been used for tracking experiments and is planned to be modified to a full ion CT setup. As preparatory work to this real setup, the focus of this thesis lies on simulations of an ion CT and the subsequent image reconstruction.

Section 2 contains the physical processes and mathematical backgrounds of this thesis. These include the interaction of ions and matter, the medical applications and finally reconstruction algorithms and path estimates for ions in matter. Section 3 introduces the MedAustron facility, the software frameworks used in this thesis and gives an overview on the whole image reconstruction process. Finally, Section 4 displays and discusses the results of this thesis and Section 5 gives a short summary and an outlook on the next steps.



Die approbierte gedruckte Originalversion dieser Diplomarbeit ist an der TU Wien Bibliothek verfügbar.
The approved original version of this thesis is available in print at TU Wien Bibliothek.

2 Physical and mathematical background

In this section, an overview on the physical and mathematical principles used for image reconstruction will be given. Since the focus of this thesis lies on the imaging process using a proton beam, the interactions and methods described in this Section are also mostly pointed out for protons. Section 2.1 gives a short introduction to interaction processes of ions with matter. Section 2.2 gives an insight on the use of heavy charged particles for medical imaging and therapy. In Section 2.4, the mathematical background and algorithms needed for the image reconstruction process are discussed.

2.1 Interactions of ions and matter

This Section introduces the physical interactions that take place when ions propagate through matter. Section 2.1.1 displays how the stopping power for ions can be calculated with only considering the most prominent interaction process of ions and matter. The range in matter is introduced in Section 2.1.2. Section 2.1.3 and Section 2.1.4 introduce interaction mechanisms that lead to the deflection of an ion from its originally nearly straight-line path or the reduction of ion fluence. As a result of these considerations, Bragg curves are discussed in Section 2.1.5.

2.1.1 Bethe-Bloch equation

Heavy charged particles such as protons can undergo different interaction processes when passing through matter. Dominant processes for the interaction of these particles with matter are Coulomb interactions with shell or nucleus (for the latter see Section 2.1.3), nuclear reactions (see Section 2.1.4) and bremsstrahlung [7].

In a first-order approximation heavy charged particles pass on nearly straight paths (due to their high mass) through matter losing energy due to inelastic Coulomb interactions with the electrons of atomic shells. However, when an ion passes near to an atomic nucleus, an elastic Coulomb interaction deflects the ion from its original path. For protons, also the less-frequent inelastic nuclear Coulomb reactions are possible. In that case, the proton enters the nucleus which may then emit one or more secondary particles. Proton Bremsstrahlung can be neglected at clinical energies [7]. The interaction processes (except for Bremsstrahlung) are shown for protons in Figure 2.1.

The energy loss caused by inelastic Coulomb interactions of an ion with charge Z_1e passing through matter can be approximately shown using a simple model: The ion can only transfer energy to an atomic electron, if the transferred energy is larger than the binding energy of the respective electron. After the process, the ion continues on its straight path and the electron can be regarded as free [8]. The momentum transferred to the electron can be calculated from the Coulomb force, which is given in Equation (2.1).

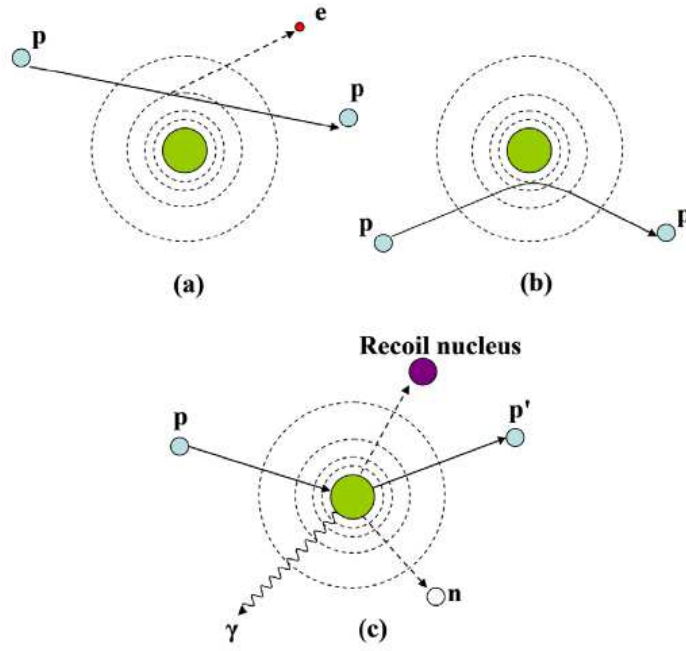


Figure 2.1: Interaction mechanisms of protons and matter [7]: (a) inelastic Coulomb interaction, (b) elastic Coulomb scattering with nucleus, (c) non-elastic nuclear reactions.

$$\vec{F}_C = \frac{Z_1 e^2}{4\pi\epsilon_0 r^2} \hat{r}, \quad (2.1)$$

where $Z_1 e^2$ is the product of ion and electron charge, ϵ_0 is the vacuum permittivity and r is the distance between ion and atomic electron [8]. Integration of the Coulomb force and use of the divergence theorem finally leads to the transferred momentum to an electron:

$$\Delta p = \frac{1}{2\pi\epsilon_0} \frac{Z_1 e^2}{vb}, \quad (2.2)$$

where Δp is the transferred momentum to an electron, v is the ion velocity and b is the standard distance between ion path (SL) and electron [8], as it can be seen in Figure 2.2.

From the equation for the momentum, the energy transfer to a single electron can be calculated as

$$\Delta\epsilon = \frac{\Delta p^2}{2m_e} = \frac{1}{8\pi^2\epsilon_0^2 m_e} \left(\frac{Z_1 e^2}{vb}\right)^2, \quad (2.3)$$

with the electron mass m_e [8]. Since not only the energy transfer to one electron but the energy loss of all interactions along a certain distance are to be calculated, an

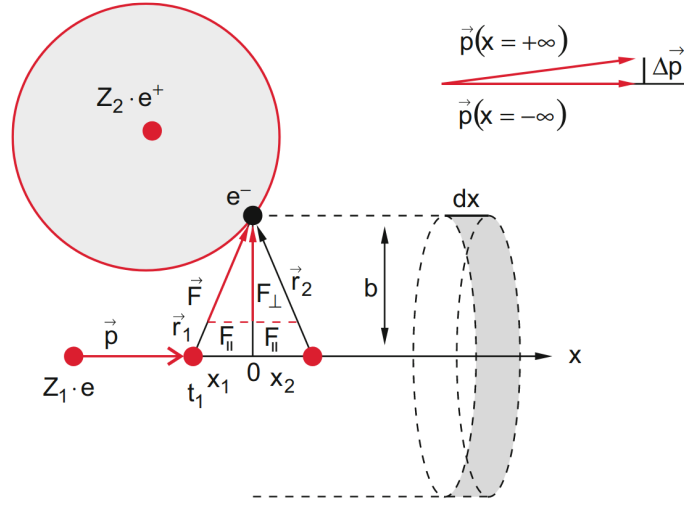


Figure 2.2: Parameters for the calculation of the Bethe-Formula [8].

integration over all impact parameters within the limits (b_{\min} , b_{\max}) of this model has to be done. This leads to the specific energy loss,

$$\frac{dE}{dx} = -\frac{Z_1^2 e^4 n_e}{4\pi \epsilon_0^2 v^2 m_e} \cdot \ln\left(\frac{b_{\max}}{b_{\min}}\right), \quad (2.4)$$

with the electron density n_e . Since b_{\min} and b_{\max} are again depending on the ion velocity and on the binding energy of the atomic electrons, Equation (2.4) can be further modified. A quantum mechanical calculation valid for relativistic particles has been done by Bethe, Lindhard, Scharf and Schiøt [8]. Several correction terms have been added afterwards to the equation so that finally the Bethe-Bloch equation, which determines the so-called stopping power S , can be written as [7]

$$S = -\frac{dE}{dx} = 4\pi \rho N_A r_e^2 m_e c^2 \frac{Z}{A} \frac{z^2}{\beta^2} \cdot \left[\ln \frac{2mc^2 \beta^2 \gamma^2}{I} - \beta^2 - \frac{\delta}{2} - \frac{C}{Z} \right], \quad (2.5)$$

where ρ is the material density, N_A Avogadro's number, r_e the classical electron radius and mc^2 is the mass energy of an electron. I is the mean excitation potential, Z the atomic number and A the atomic weight of the material. The variable z stands for the charge of the incident hadron in units of the electron charge. Finally, $\frac{\delta}{2}$ and $\frac{C}{Z}$ are the shell and density correction terms [7]. For some calculations, it is necessary to add further high order correction terms, such as the spin correction term [9].

The stopping power in Equation (2.5) can be expressed by a simplified term using the Bragg-Kleeman law [10],

$$-\frac{dE}{dx} = -\frac{E^{1-p}}{p\alpha}, \quad (2.6)$$

where α is a material constant and p is a constant that depends on particle type and velocity.

In the following, the correction terms introduced in Equation 2.5 will be briefly described.

Shell correction term This term refers to the interaction of atomic electrons with the atomic nucleus. It becomes significant for low energies and heavy atoms. The term can be expressed as

$$C = \sum C_\nu(\theta_\nu, \eta_\nu), \theta = \frac{J_\nu}{\epsilon_\nu}, \eta_\nu = \frac{\beta^2}{\alpha^2 Z_\nu^2}, \quad (2.7)$$

where ν stands for the nuclear shell, J_ν and ϵ_ν are the ionisation energy and the Bohr ionisation energy of the shell ν , α is the fine structure constant, β is the hadron velocity and Z_ν is the effective charge of the respective shell [9].

Density correction term This term takes into account that a material is likely to become polarized when a charged particle enters with a high velocity and atoms can no longer be regarded as isolated. This is the reason why this term becomes significant at high energies. To calculate the value of the term, the formulation from Sternheimer [11] can be used,

$$\begin{aligned} \delta(x) &= 0 \text{ for } x < x_0 \\ \delta(x) &= 4.606x - C + a(x_1 - x)^m \text{ for } x_0 \leq x < x_1 \\ \delta(x) &= 4.606x - C \text{ for } x \geq x_1, \end{aligned} \quad (2.8)$$

where x_0 and x_1 are depending on the material and x is the kinetic variable of the particle and defined as $x = \ln(\frac{\beta^2 \gamma^2}{4.606})$ [9, 12]. The material specific parameters to be calculated are [9]

$$\begin{aligned} h\nu_p &= \sqrt{4\pi n_e r_e \hbar c} \\ C &= 1 + 2 \ln\left(\frac{I}{h\nu_p}\right) \\ x_a &= \frac{C}{4.606} \\ a &= 4.606 \frac{(x_a - x_0)}{(x_1 - x_0)^m} \\ m &= 3, \end{aligned} \quad (2.9)$$

with the plasma energy of the material $h\nu_p$.

Referring again Equation (2.5), the left side is often divided by the absorber mass density ρ . It can be seen that except for this quantity, the rate of the ionisation loss does not depend strongly on the absorber material. The resulting function $\frac{dE}{\rho dx}$ therefore shows a very similar shape for all absorber materials [8, 13].

2.1.2 Range of ions in matter

Starting from Equation (2.5), the range can be defined as the distance at which half of the ions of a beam have come to rest. It is therefore an average value for a large number of particles and not a value representing a specific particle, since the energy loss of different particles shows some variations [7]. Assuming that the ions lose their energy continuously and on a SL path, the range can be written as

$$R(E_0) = \int_0^{E_0} \frac{dE}{dE/dx} \approx \sum_0^{E_0} \left(\frac{dE}{dx}\right)^{-1} \Delta E, \quad (2.10)$$

with the initial ion energy E_0 [8, 7]. Using the Bragg-Kleeman rule, the range can be simply rewritten as

$$R(E_0) = \alpha E_0^p, \quad (2.11)$$

with the material parameter α and p depending on the initial particle type and energy (see also Equation (2.6)). For protons, an initial particle energy of 11 MeV results in a range of approximately 1 mm, an energy of 220 MeV results in a range of approximately 30 cm in liquid water (similar density to human tissue). These are usually the range limits of interest for clinical applications [7].

Until this point, the energy loss of ions has been regarded as continuous and the path of the ions has been considered as straight. This is a sufficient approximation for many applications, however, the slight variation of the energy loss of primary particles influences the shape of Bragg-curves (see Section 2.1.5) and dose distributions. This effect is called range straggling. A detailed description of straggling effects can be found in [7].

2.1.3 Multiple Coulomb Scattering

As already mentioned in Section 2.1.1, an ion path through matter can only be considered as a SL in a first-order approximation. In reality, the ions in the energy range used for clinical applications are deflected from their original path due to MCS, which refers to the inelastic Coulomb scattering with atomic nuclei. These interactions lead to multiple small-angle deflections of the ions [14]. The exit angular distribution can be written for a mono-energetic parallel beam of protons for thin objects according to [15]:

$$\sigma(l, E) = \frac{13.6}{\beta(E)p(E)} \sqrt{\frac{l}{X_0}} [1 + 0.038 \cdot \ln(\frac{1}{X_0})], \quad (2.12)$$

where $\beta(E)$ and $p(E)$ are velocity and momentum of the proton, X_0 is the material radiation length and l is the length of the proton path. This model is only valid for protons going through thin objects, which means that X_0 has to be significantly smaller than l (otherwise, Equation (2.12) has to be integrated over the energy range within the object) [14].

The radiation length, i.e. the mean length in a material to reduce the energy of an electron due to bremsstrahlung by a factor of $1/e$, can be written for a single element using the empirical formula [14]

$$X_0 = \frac{716.4 \cdot A}{Z(Z+1) \cdot \ln\left(\frac{287}{\sqrt{Z}}\right)}, \quad (2.13)$$

with the element mass number A and the atomic charge numbers Z .

2.1.4 Nuclear interactions

Nuclear interactions of ions in matter lead to a decrease of fluence which depends on the thickness of the material. For protons the remaining particle fluence at a depth l within a material can be calculated using

$$\phi(l) = \phi_0 \cdot \exp\left(-\int_l \kappa(x, y, z, E) dl\right), \quad (2.14)$$

where $\kappa(x, y, z, E)$ is the nuclear cross Section of a proton at coordinates (x, y, z) within the material, which depends on the energy E of the incident proton. If a material consists of more than one element, the total nuclear cross Section for a charged particle can be calculated from knowing the cross sections of the single elements [14].

Additionally to the reduction of particle fluence, nuclear interactions can lead to the liberation of secondary particles. When a proton is absorbed by an atomic nucleus, a neutron can be liberated which can then again cause other nuclear reactions. Other possible secondary particles are secondary protons, which may be further transported, or heavy recoil fragments, which deposit their energy locally [14].

2.1.5 Bragg curves

Equation (2.5) already showed that the energy loss slightly decreases with a higher initial energy of the ion beam. For very small energies, the term dE/dx strongly increases. Therefore ions deposit most of their energy per distance in the last few mm of their penetration path, resulting in the typical Bragg-Peak shape [7, 16].

Figure 2.3 displays the typical Bragg peak shape for ions using the example of a proton beam. The peak shape depends on the ion type and is - for example - steeper for carbon ions than for protons. The areas of interest will be shortly discussed in the following using the example of a proton beam.

Electronic build up region This effect takes place in a region close to the surface of the absorbing material. Protons with high energy are able to liberate delta rays which may travel up to a few millimeters in the tissue and can lead to an increase of the dose in an area corresponding to the most penetrating recoil electron. However, this effect cannot always be observed and depends strongly on the absorber material [7].

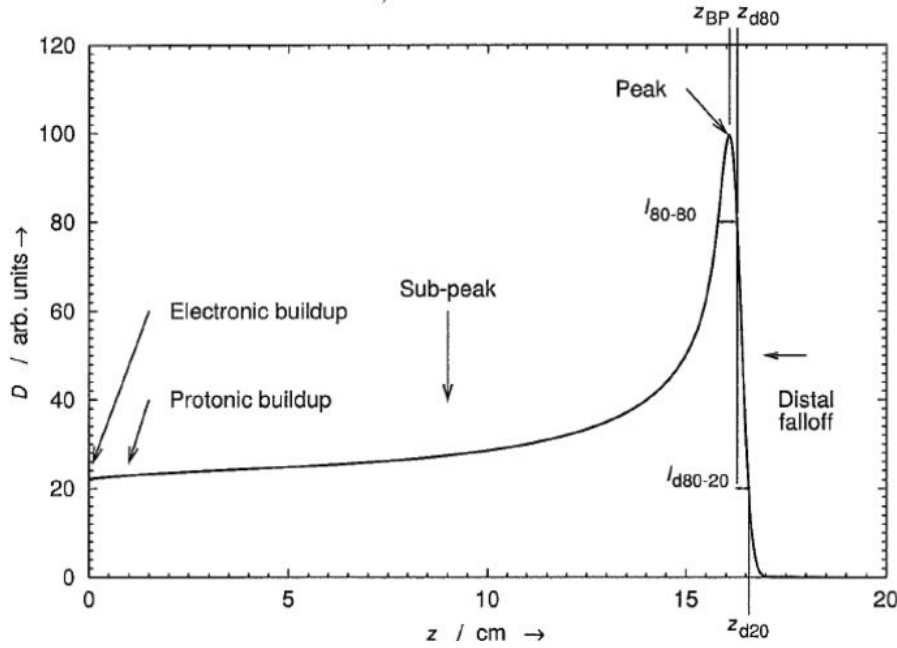


Figure 2.3: Bragg peak shape for protons [7].

Protonic build up region The dose near the surface of the absorbing material can also be increased due to secondary protons. The probability to observe this effect increases with higher incident proton energies [7].

Sub-peak region (Plateau) This region describes the plateau ranging from the surface of the absorber material until the very beginning of the actual Bragg peak. Its shape and depth is strongly influenced by the velocity of the primary protons, but also depending on removal of protons due to nuclear reactions, secondary particles or lateral deflections due to MCS [7].

Peak region The peak region is the area of the maximum dose rate and is located at the end of the proton beam range. Location and height of the peak are mostly defined by the stopping power and energy straggling. The depth of the Bragg peak, z_{BP} , can be defined with the range R :

$$z_{BP} = R \pm 4\sigma, \quad (2.15)$$

where σ is the distal falloff width [7].

Distal fall-off region This area refers to depths greater than the Bragg peak area (as defined in Equation (2.15)). It can be restricted to a threshold value, for example, to the depth where the dose falls under 1% [7].

2.2 Medical applications of ions

Regarding medical applications of ions, there are two separate use cases: the actual cancer treatment (radiotherapy), which is described in Section 2.2.1 or the imaging process, which will be discussed in Section 2.2.2.

2.2.1 Cancer treatment with ions

The standard treatment methods for cancer include surgery, chemotherapy and radiotherapy, where about two thirds of the patients receive the last-mentioned treatment. Within radiotherapy, the treatment with X-rays is still the most popular one. The treatment with high-energy charged particles is still an exceptional case - in 2014, this treatment was only applied to less than 1% of patients. One of the reasons therefore is that the treatment with ions requests an expensive equipment such as a synchrotron or cyclotron [17]. However, the number of applications is steadily increasing, with protons still being the most used particle type [3].

One of the main challenges in radiotherapy is to apply a high dose to the tumorous area, while keeping the dose to the healthy tissue as low as possible. For the conventional radiotherapy with X-rays this leads to a large number of beams, irradiating the patient from different angles [3]. This results from the typical dose profile of photons in tissue, resulting from the exponential decrease of intensity of photons passing through matter [18],

$$I_{\text{out}} = I_{\text{in}} \cdot \exp\left(-\int_{x_{\text{in}}}^{x_{\text{out}}} \mu \cdot dx\right) = I_{\text{in}} \cdot \exp(-\mu \cdot \Delta x), \quad (2.16)$$

with the linear attenuation coefficient μ , depending on the photon energy and the absorber material. Equation (2.16) is valid for a mono-energetic beam. For real beams, which consist of photons of different energies, an additional function, which describes the energy distribution, has to be added to the equation, leading to an additional integral [18].

Although a high dose to the tumorous area can be achieved with the irradiation from several angles, the cost is also a significant dose to the healthy tissue of the patient, which then again increases the risk of secondary cancer. Radiotherapy with protons and heavy ions on the other hand offers an advantage which can be easily understood with Figure 2.3. These particles deposit more of their energy per unit length with increasing depth. This allows radiotherapy with far less beams and makes this method also effective for deep-seated tumours [3].

To cover the whole tumorous area, a so-called Spread-Out Bragg Peak (SOBP), resulting from a number of particle beams with varying energy is used. The principle is displayed in Figure 2.4. Multiple Bragg curves are superposed, starting with a high beam energy and then decreasing the energy step-by-step. The result is a high dose in the tumorous area and a strong fall off edge whose location can be defined by the different energies used for the beams. The resulting SOBP for protons (orange curve) is compared to the typical dose distribution of a photon beam (green curve) in tissue

in Figure 2.4. Compared to radiotherapy with X-rays, there are two possibilities for ion radiotherapy: Either the dose in the tumorous area is set to a significantly higher value but resulting with the same dose to the healthy tissue as with X-rays. The other option is that the dose to the tumorous area is set as high as with X-rays, resulting in a significantly lower dose to the healthy tissue [3].

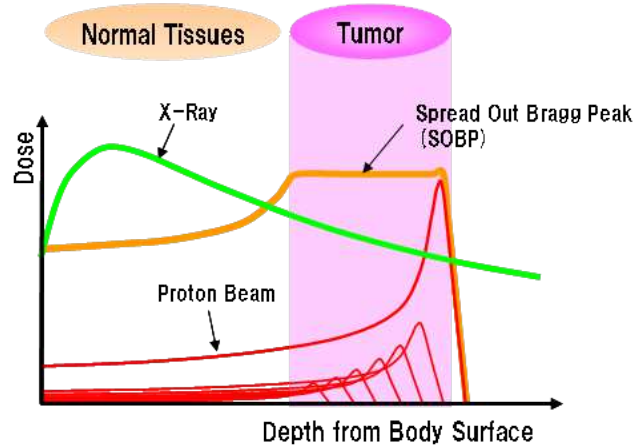


Figure 2.4: SOBP [7].

The dose is a typical value considered for treatment planning since it is defined as the total absorbed energy per mass:

$$D = \frac{d\bar{\epsilon}}{dm}, \quad (2.17)$$

where $d\bar{\epsilon}$ is the mean energy transferred through ionizing radiation to the mass element dm . The unit of the dose is J/kg but it is usually expressed using Gray (1 Gy = 1 J/kg) [14].

Another term to be introduced for radiotherapy with ions is the Water-Equivalent Thickness (WET). Water shows similar characteristics to human tissue when it is penetrated by an ion beam. Therefore it is often used as a reference material for range or dose calculations. In the clinical practice, the penetration power of an ion beam is therefore often defined by its penetration range in water. On the other hand, the thickness of absorbing objects in the beam path is commonly specified as if the objects were made of water, which can be seen in Figure 2.5. Here, an object made of a material m is penetrated by an ion beam of energy E_i . After passing the object, the residual beam energy E_f can be measured in a water tank. The WET of the object can now be understood by replacing the object with a block of water with length t_w , so that the residual beam energy E_f corresponds to the one of the actual object. By performing this calculation, range losses can be easily added or subtracted from one another [7].

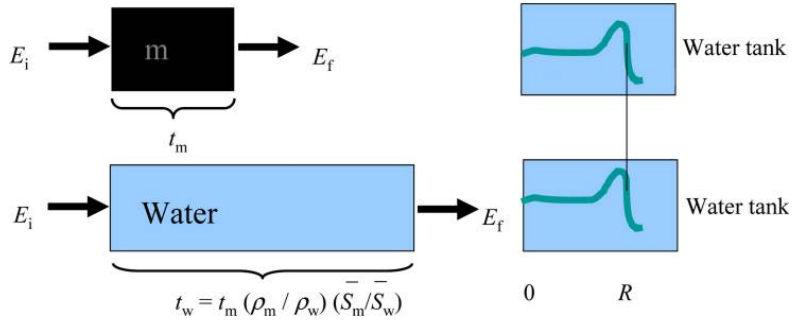


Figure 2.5: Demonstration of water equivalent thickness [7].

The International Atomic Energy Agency (IAEA) proposed to approximate the WET as

$$t_w = t_m \frac{R_w}{R_m}, \quad (2.18)$$

with the actual material thickness t_m and the ranges in water (R_w) and the material (R_m). Since the ranges R_w and R_m correspond to the total energy loss within water and absorber material, Equation (2.18) is only valid for stopping-length objects [7]. An exact equation for the WET applicable for thin objects was therefore given by [19] as

$$t_w = t_m \frac{\rho_m \bar{S}_m}{\rho_w \bar{S}_w}, \quad (2.19)$$

with mass densities of water (ρ_w) and the material (ρ_m) and the mean mass stopping powers again for water (\bar{S}_w) and the material (\bar{S}_m). The mean stopping power is hereby defined as [19]

$$\bar{S} = \frac{\int_E S dE}{\int_E dE} \quad (2.20)$$

2.2.2 Ion imaging

There are two applications for imaging with ions: One is the process of 2D imaging called radiography, the second one is the ion CT, consisting of several radiography images taken from different angles and being reconstructed to a full 3D image. The idea to use ions for CT imaging first came up in the 1960s [17].

In spite of the fact that this application for ions has been known for a while, radiotherapy treatment planning is usually still based on an X-ray CT, whether the treatment is done with X-rays or with heavy ions. The reason why ion radiography and CT are not often applied clinically lies i.a. within the expensive equipment needed and the reduced image quality due to MCS [17]. The values in an X-ray CT are usually given in Hounsfield Units (HU) [14],

$$HU = \frac{\mu_m - \mu_w}{\mu_w} \cdot 1000, \quad (2.21)$$

with the linear attenuation coefficients of the material (μ_m) and water (μ_w). Although the X-ray CT values are correlated to the Relative Stopping Power (RSP) of ions in matter (due to the material electron density influencing them both), the conversion from HU to the RSP leads to range uncertainties in the resulting ion radiotherapy treatment planning [14]. A method for the conversion of HU for radiotherapy was demonstrated in [20]. Real tissue was approximated with tissue substitutes to measure the relationship between HU and proton stopping power. Since the chemical composition of such substitutes varies from real tissue, this step is a possible source of error. To minimize this error, the measured HU of the substitutes were combined with the chemical composition of real tissue.

Nevertheless, the uncertainties from this conversion can become essential when a tumour near a sensitive area has to be irradiated [3]. If, for example, a tumour near the optical nerve has to be irradiated, the imaging process with ions becomes a reasonable application. In contrast to radiotherapy, ions need to fully pass the patient for imaging purposes. The residual energy is then measured by an energy detector. Although different energies are used for radiotherapy and imaging, the measured energy loss of the ions in the imaging process can be directly linked to treatment planning. The reason is that the stopping power ratio (ratio of stopping power at a distinct point relative to that of water) for a material within the human body is approximately constant with energy and its slow variation has already been investigated [17]. This has been shown in [21], where the mass stopping power ratio of air and bone (represent the minimal and maximal mass densities in the human body) at 200 MeV to that at an energy E has been compared to the mass stopping power ratio of water at the same energies. The error percentage was shown to be less than 0.6 % over the considered energy range.

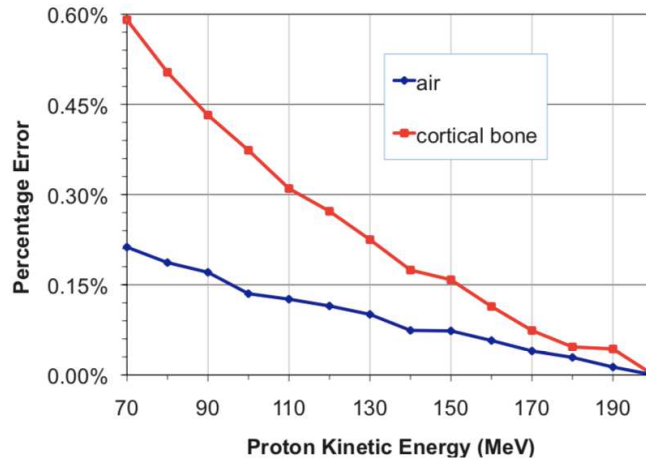


Figure 2.6: Percentage error of the mass stopping power ratio of 200 MeV and energy E for air and bone compared to that of water [21].

Figure 2.7 shows a typical setup for imaging with ions. An ion beam is directed through two front tracker planes, a patient or a phantom, two rear tracker planes and finally lead in an energy measurement device (e.g. a calorimeter). The tracker planes are position-sensitive detectors, used to investigate the ion path, which is affected by MCS. Out of the four hit positions, the ion path can be approximately calculated, as it will be discussed in Section 2.3. The measurement of the residual ion energy is then used to create image contrast [3].

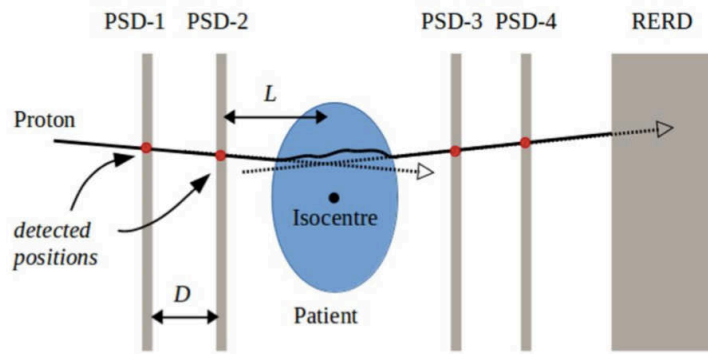


Figure 2.7: Schematic overview of ion imaging setup (PSD - Position Sensitive Detector, RERD - Residual Energy Resolving Detector) [17].

The setup in Figure 2.7 could be used for a radiography. For a ion CT the setup would have to rotate around the patient, generating projections at several angles. To reconstruct a full 3D model from the projections, a reconstruction algorithm will be applied. These algorithms will be discussed in Section 2.4.

In conclusion, advantages and disadvantages of a proton CT, which are also valid for other ions, have been described in [22]. The main advantages over the conventional X-ray CT are given as the lack of beam hardening artefacts and the significantly lower dose (see [23]) to be applied for the same density resolution. Furthermore, fast scanning may be possible, since the number of ions needed for imaging can be provided in a short time interval (with tracking system properties being a limiting factor). On the other hand, the application of ion CT, requires a costly and complicated equipment and it is also more complicated to deliver the ion beam to the patient than an X-ray beam. Another disadvantage of ion CT is the effect of MCS, that was already discussed. The use of heavier particles (such as carbon ions) reduces this effect. For an improved contrast in X-ray CT, contrast agents are often applied. However, they cannot be applied for ion CT, since the stopping power does not depend on Z effects as strongly as the attenuation coefficient [22].

2.2.3 Tomographic equation and projection definition

The following derivation of the tomographic equation was originally presented in [24] for a proton CT reconstruction with an iterative algorithm. Corresponding to Equation

(2.5), the linear stopping power S per path length dl at a path point (x, y) equals the energy loss dE of a fast, charged particle with energy E ,

$$-dE = S(x, y, E)dl. \quad (2.22)$$

Making use of the mass stopping power S/ρ , Equation (2.22) can be extended and transformed to

$$-\frac{S}{\rho}(x, y, E_0)dE = \frac{S}{\rho}(x, y, E_0)\frac{S}{\rho}(x, y, E)\rho(x, y)dl, \quad (2.23)$$

where E_0 is a reference energy where the stopping power is known (e.g. the initial particle energy). Dividing Equation (2.23) by the mass stopping power, one obtains

$$-\frac{\frac{S}{\rho}(x, y, E_0)}{\frac{S}{\rho}(x, y, E)}dE = S(x, y, E_0)dl. \quad (2.24)$$

Since the ratio on the left side of Equation (2.24) does not strongly depend on the material composition (see Figure 2.6), it can be replaced by the stopping power ratio measured for liquid water,

$$-\left[S(H_2O)\right]_E^{E_0} = S(x, y, E_0)dl. \quad (2.25)$$

An integration along the ion path finally leads to the tomographic equation

$$-\int_{E_{in}}^{E_{out}} \left[S(H_2O)\right]_E^{E_0} = \int_{\text{path}} S(x, y, E_0)dl, \quad (2.26)$$

where the path can be approximated by the approaches described in Section 2.3. A discretization of the problem (dividing the phantom in N pixels) finally leads to the definition of the CT projections:

$$p_i = -\int_{E_{in}}^{E_{out}} \left[S(H_2O)\right]_E^{E_0} = \sum_{i=j}^N w_{ij}S_j(E_0), \quad i = 1, \dots, M, \quad (2.27)$$

with the ion i trajectory length w_{ij} at pixel j . This set of linear equations is then solved (with an iterative reconstruction algorithm) for the stopping power $S_j(E_0)$ [24].

In the following, another definition of the projections using a SL approach for a proton CT will be demonstrated. It is the definition that will be finally used for the projections in Section 3.3.3 (see also Equation (3.14)). Starting point is the Bragg-Kleeman law, which has already been introduced in Equation (2.6). Although the parameter p depends on the particle velocity, it can be seen in [25] that it is close to 1.7 for all protons in the clinical energy ranges. Considering this value to be fixed, the only unknown parameter remains the material constant α , which depends for a SL approach parallel to a coordinate axis only on the position (x, y) within the material. As a result, Equation (2.6) can be written as

$$\frac{dE}{ds} = \frac{E^{-0.7}}{\alpha(x, y)1.7}, \quad (2.28)$$

where the path element ds corresponds to a path element parallel to the axis of beam direction. Rearranging the equation and applying an integral over the energy range within the irradiated object leads to

$$1.7 \cdot \int_{E_{\text{in}}}^{E_{\text{out}}} E^{0.7} dE = \int_{x_{\text{in}}}^{x_{\text{out}}} \frac{1}{\alpha(x, y)} ds. \quad (2.29)$$

Calculating the value of the left side and approximating the integral on the right side of Equation (2.29) leads to

$$E_{\text{in}}^{1.7} - E_{\text{out}}^{1.7} \approx \left| \sum \frac{1}{\alpha(x, y)} \Delta s \right|, \quad (2.30)$$

which corresponds to the projection theorem applied for the projection definition in X-ray CT imaging, where the projection at an angle θ is defined as [18, 26]:

$$p(\theta, x, y) = \int \mu(x, y) ds \approx \sum \mu(x, y) \Delta s, \quad (2.31)$$

and the application of a reconstruction algorithm returns the unknown function $\mu(x, y)$. For ions, the term $1/\alpha$ is the unknown function that will be defined by the reconstruction process.

2.3 Path estimates

As already mentioned in Section 2.1.3 and Section 2.2.2, ions undergo the process of MCS when they are propagating through matter, which deflects them from their original path. To take this effect into account for the generation of projections, there are three common ways of approximating the ion path.

The simplest approximation approach is the SL path, which was also applied for the reconstruction work within this thesis. For example, this path can be defined by only one point (exit point measured at a rear detector, see Figure 2.8 (a)). In this case, the SL path is chosen to be parallel to the coordinate axis of beam direction. Another form SL approach uses two points for definition, one measured at a front detector, one at a rear detector (Figure 2.8 (b)). These two points are simply connected to obtain the approximated ion path. A third option for a SL approximation is given in 2.8 (c), where positions and directions upstream and downstream from the object have to be known.

Another possibility of approximating the ion path is the cubic spline. Here, particle hit positions from the two front detectors are used to calculate the entry point of the phantom, respectively, the particle hit positions of the two rear detectors are used to calculate the phantom exit point (convex hull of the phantom has to be known first). Between entry and exit point, the ion path is approximated with a smooth polynomial [27].

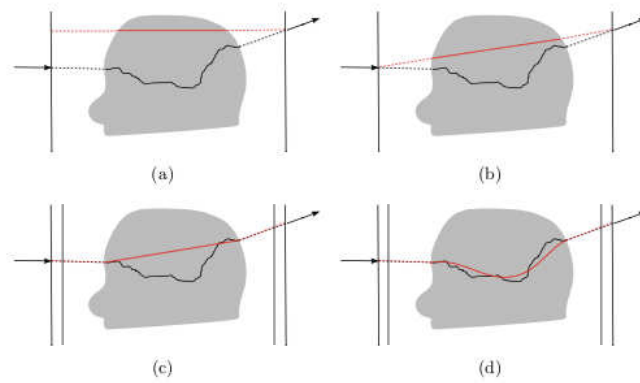


Figure 2.8: Overview on some possible path estimates (red) compared to the real ion path (black) from [14] (adapted): (a) SL using only one hit position of a rear detector, (b) SL using hit position from a front and a rear detector, (c) several SLs using hit positions and particle directions in front of and behind the phantom and (d) a most likely path approach using positions and directions before and after the phantom.

The cubic spline is defined as

$$t'(u) = a + bu + cu^2 + du^3, \quad (2.32)$$

where the parameters a, b, c and d , that define position and slope of the polynomial, are set in respect to exit and entry point of the phantom [27].

A third approximation method for the ion path is the MLP (see Figure 2.8 (d)), which is also the most complicated approach of the methods mentioned. As for the cubic spline, entry and exit point of the phantom as well as the particle directions are used. Within the phantom, there is an infinite number of possible ion paths which follow certain a probability distribution [27]. For protons, the calculation of a proton probability map, which can be used to calculate the MLP of a proton for each point through an object has been shown in detail in [21] and will only be briefly demonstrated.

In [21], a proton beam in direction of the z -axis is assumed. Within a uniform medium, the distribution function $F(x, z, \theta)$ describes the probability that a proton is deflected into lateral position x and direction θ in the zx -plane. For the definition of the function, different approaches (like brute force in Monte Carlo simulations) can be used. However, in [21], the formulation defined by Fermi [28] was used,

$$F(x, y, \theta) = \frac{\sqrt{3}\omega^2}{2\pi z^2} \exp\left(-\omega^2\left(\frac{\theta}{z} - \frac{3x\theta}{z^2} + \frac{3x^2}{z^3}\right)\right), \quad (2.33)$$

where z is the depth in the medium, x is the lateral deviation at z projected to the xz -plane, θ is the direction at the given depth with respect to the z -axis and ω is depending on the energy of the proton. One problem with Fermi's formulation was that ω is assumed to be a constant value, which is not valid for protons. Therefore is was

replaced by a depth-dependant function $u(z)$, which can be obtained by simulations at different depths [21].

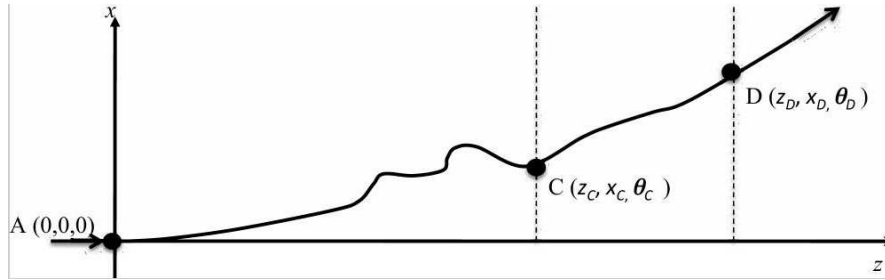


Figure 2.9: For the definition of the MLP: Entry point A and exit point D of the proton are known. The probability of the proton passing the intermediate point C is to be estimated [21].

The resulting distribution function, $F_u(x, z, \theta)$, can then be used to calculate the path probability of a proton with a known initial energy. If the material entry point $A(x_A, z_A, \theta_A)$ and the exit point $D(x_D, z_D, \theta_D)$ (see Figure 2.9) are known, the probability of a proton passing point $C(x_C, z_C, \theta_C)$ within the material can be established using [21],

$$P(A \rightarrow C|D_\theta) = \frac{\int F_u(A \rightarrow C_\theta)F_u(C_\theta \rightarrow D_\theta)d\theta_C}{F_u(A \rightarrow D_\theta)}, \quad (2.34)$$

where $P(A \rightarrow C|D_\theta)$ stands for the conditional probability and can be rewritten as [21]

$$P(A \rightarrow C|D_\theta) = \frac{P(A \rightarrow C)P(C \rightarrow D_\theta)}{P(A \rightarrow D_\theta)}, \quad (2.35)$$

where the subscript θ illustrates that the conditions C and D are valid for a specific direction of the proton.

In [29], a comparison of the path estimates that have been presented in this Section has been performed. A SL, a cubic spline and a MLP approximation has been calculated for protons passing through a 200 mm water phantom. Furthermore, a simulation of 10 000 protons passing through the same phantom has been performed and each step has been monitored. Therefore a value for the real proton path could be established to which the approximations could be compared.

Figure 2.10 shows the results of the calculations. The RMS deviation of the different approaches from the real (simulated) proton is compared. As expected, the SL approach performs worst. On the other hand, cubic spline and MLP show similar results [29].

2.4 Image reconstruction algorithms

In this section, several different algorithms for CT image reconstruction will be discussed. In Section 2.4.1, the Filtered Backprojection (FBP) method will be introduced, which

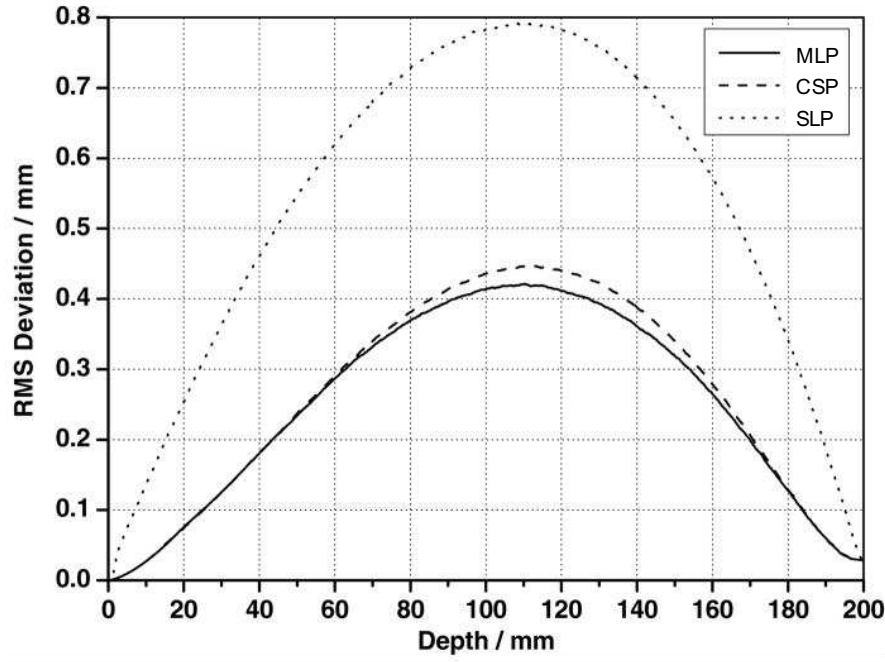


Figure 2.10: Comparison of different path estimates [29] (adapted): Root-Mean Square (RMS) deviation from real path to MLP - most likely path, CSP - cubic spline path and SLP - straight line path.

is a really fast method compared to the iterative algorithms described in Section 2.4.2. However, these methods generate superior results compared to the first approach, as it can be seen in the reconstruction results of this thesis (see Section 4).

2.4.1 Filtered-backprojection

The backprojection method is an approach that can be used to determine the linear attenuation coefficient $\mu(x, y)$ in an X-ray CT. This coefficient equals an unknown spacial distribution function $f(x, y)$ - in the case of ion CT, this function can also describe the material parameter $\alpha(x, y)$ as it is described in Section 2.2.3. To determine the unknown function $f(x, y)$, the projection slice theorem can be used. Starting from an object irradiated at an angle φ (see Figure 2.11) and at orthogonal distance r to the origin, the Radon transform can be defined as

$$R_f(\varphi, r) = \int_{\substack{(x \\ y) \cdot \begin{pmatrix} \cos \varphi \\ \sin \varphi \end{pmatrix} = r}} f(x, y) ds, \quad (2.36)$$

and can be understood as the integral of the unknown function $f(x, y)$ along the path ds through the object [30].

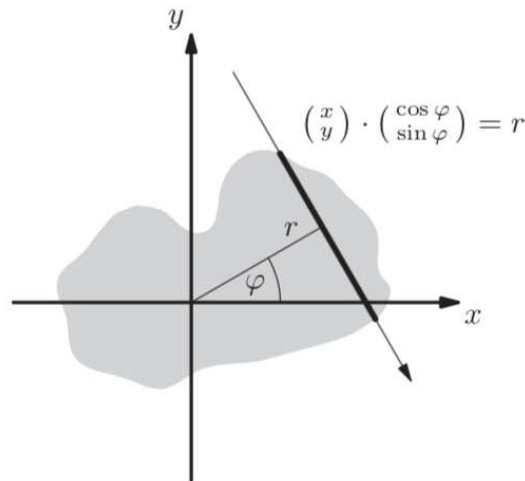


Figure 2.11: An object is irradiated at an angle φ relative to the x -axis and an orthogonal distance r to the origin [30].

A CT therefore measures the Radon transform for different angles φ and many different radii. The result is the so-called sinogramm, which is displayed for the simple example of a disc in Figure 2.12 [30].

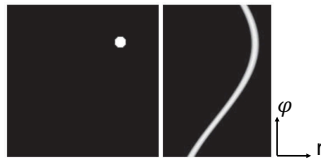


Figure 2.12: Radon transform (right) of a disc (left). The abscissa represents the different radii (from 1 to 128), the ordinate represents the different values of φ (from 0 to 179 degrees) [30].

The projection slice theorem connects the Radon transform to the Fourier transform. This process is illustrated for $\varphi = 0$ in Figure 2.13, where axes and angle are defined according to Figure 2.11. Taking the 2D Fourier transform of f and then taking the slice at $x = \varphi = 0$ equals the process of taking the Radon transform along the y -axis (perpendicular to the x -axis) and applying a 1D Fourier transform to the result. This relation can be written as

$$\hat{f}(k, 0) = \frac{1}{2\pi} R_f(\widehat{0, \cdot})(k), \quad (2.37)$$

where $R_f(\widehat{0, \cdot})(k)$ is the Fourier transform of the Radon transform defined in Equation (2.36) [30].

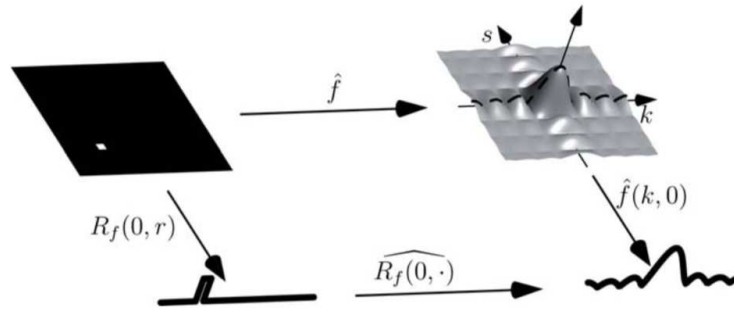


Figure 2.13: Projection slice theorem for $\varphi = 0$ [30].

Using the relation of Equation (2.37) and starting from a 2D inverse Fourier transform of \hat{f} , it has been shown in [31] that the function of interest, f , can finally be obtained from

$$f(x, y) = \frac{1}{2\pi} \int_0^\pi \left[\frac{1}{\sqrt{2\pi}} \int_{-\infty}^{\infty} \widehat{R_f(\varphi, \cdot)}(r) |r| \exp^{ir \begin{pmatrix} \cos \varphi \\ \sin \varphi \end{pmatrix} \begin{pmatrix} x \\ y \end{pmatrix}} dr \right] d\varphi. \quad (2.38)$$

The expression in the squared brackets is the inverse Fourier transform of $\widehat{R_f(\varphi, \cdot)}(r) |r|$ evaluated at $\begin{pmatrix} \cos \varphi \\ \sin \varphi \end{pmatrix} \begin{pmatrix} x \\ y \end{pmatrix} = x \cos \varphi + y \sin \varphi$. In [30] it is shown that this corresponds to a filtering operation of the function $R_f(\varphi, r)$, interpreted as a function of r , a fixed angle φ and a filter with frequency response of $|r|$ (called ramp filter) which is therefore justifying the name of the method [30].

2.4.2 Iterative techniques in image reconstruction

Iterative algorithms have been used in image reconstruction since the early 1970s at the time when the first X-ray Computed Tomography scanner was developed by Hounsfield. Commonly, the algorithms redefine a discrete estimate of the reconstructed object step by step. Therefore the simulated projection data (based on a current image estimate) is compared with the real projection data and the difference between these two is calculated and reduced in each step. The estimated image can be a blank one or one that was obtained with a faster but less precise method (such as the FBP). The algorithms differ on how the difference between simulated and real projection data is measured and how the current image estimate is updated [32].

However, they all must meet the same main requirements, as they are stated in [32]:

- *Algorithms must reflect accurate modeling of the physical processes involved in the imaging modality.*
- *The algorithm needs to efficiently handle large, sparse, inconsistent data sets.*
- *Computation time must not be a hindrance in the clinical setting.*

The fact that the physical processes are involved in the imaging process is a main advantage for proton CT image reconstruction, since the proton path through the material, that is affected by MCS can be included in the reconstruction. This allows a higher spatial resolution in the reconstruction than with analytic reconstruction techniques such as the FBP where the proton path is seen as a simple SL. One of the main challenges in the application of iterative reconstruction techniques remains the memory consumption and the calculation time. To reduce this time, parallel computing environments are often used when these algorithms are applied [32].

The aim of proton CT is to ascertain the RSP within the imaged object to further use it for treatment planning. Therefore the proton energy loss during the traversal of the imaged object is required. Considering the energy loss of I protons and a square matrix of J pixels in which the RSP is to be reconstructed, leads to a matrix equation

$$Ax = b, \quad (2.39)$$

where A is the $I \times J$ system matrix describing the interSection length of the i^{th} proton with the j^{th} pixel and b is an I -dimensional vector containing the water equivalent path lengths of I proton measurements. The elements of A can be obtained by the proton tracking and the respective path estimate, the vector b can be determined from the energy loss measurements. The J -dimensional vector x contains the estimated RSPs and is therefore refined with each step of the iterative algorithm [32].

There exist many different iterative approaches to solve Equation (2.39). One of them Algebraic Reconstruction Technique (ART) is a sequential reconstruction algorithm which starts with the definition of an initial image x^0 , the forward projections b_i are then calculated according to Equation (2.39) [26]. The current RSP estimate is corrected using the iterative equation that was introduced by [33],

$$\mathbf{x}^n = \mathbf{x}^{n-1} - \lambda_n \frac{\mathbf{x}^{n-1} \mathbf{a}_i - p_i}{\mathbf{a}_i (\mathbf{a}_i)^T} (\mathbf{a}_i)^T, \quad (2.40)$$

where \mathbf{a}_i are the entry vectors of the system matrix A and λ is a relaxation parameter leading to a faster convergence of the algorithm. The value of p_i is given by

$$p_i = \sum_{j=1}^J a_{ij} x_j \text{ and } i = 1, \dots, I \quad (2.41)$$

which is the product of a certain row of A with the solution vector x and corresponds to the Radon transform [26]. The iterative steps of Equation (2.40) are repeated until the difference between measured projections and calculated estimates is smaller than a given threshold.

Two adaptations of the ART have been used for the image reconstructions within this thesis: the Simultaneous Algebraic Reconstruction Technique (SART) and the Ordered Subset SART (OS-SART). The SART usually leads to numerical accuracy and good image quality in only one iteration. In contrast to the ART, where only one constraint is used per iteration, this algorithm uses all equations (or inequalities or constraints)

simultaneously per iteration. The OS-SART belongs to the category of block-iterative reconstruction methods. A fully-simultaneous iteration is performed using only the constraints whose indices are specified by the respective block B_t , which is a subset of $\{1, 2, \dots, I\}$ [32].

A full mathematical description of the SART and OS-SART would be beyond the scope of this thesis and can be found in [32] and [33].



Die approbierte gedruckte Originalversion dieser Diplomarbeit ist an der TU Wien Bibliothek verfügbar.
The approved original version of this thesis is available in print at TU Wien Bibliothek.

3 Methods and materials

In this section, an overview of all methods and materials used for the final image reconstructions will be given. Section 3.1 gives a short overview on the MedAustron facility, where the experimental setup, that was the underlying model for the simulations in this thesis, was built up and used. Section 3.2 contains all software frameworks that have been used for simulation of data (Geant4, ROOT), application of a reconstruction algorithms (TIGRE) and further displaying and analysis of data (ImageJ). Section 3.3 gives a detailed overview of the whole reconstruction process and how the tools introduced before are used.

3.1 MedAustron facility and experimental setup

The MedAustron [6] facility is a centre for ion therapy and research. It is located in Wiener Neustadt in Lower Austria, approximately 50 km south of Vienna. Construction of the facility started in March 2011, about one and a half years later, the staff was able to move to the newly built rooms. Clinical operation as well as research operation in the non-clinical research room started in 2016 [34, 35].

The accelerator was built with materials from more than 230 different manufactures from 22 different countries. The particle types which are used at MedAustron are protons and carbon ions, coming from three particle sources and then being pre-accelerated in a Linear Accelerator (Linac). Afterwards, they are injected to the synchrotron (circular accelerator) where they reach their final speed (about 200 000 km/s). Finally, the particles can be extracted from the synchrotron in the so-called extraction lines, which lead the particles to the irradiation rooms using strong magnetic fields [36].

MedAustron has four irradiation rooms, three of them are reserved for patient treatment and the fourth is exclusively dedicated to non-clinical research. This allows research in the fields of biology, medical physics and general particle physics. The different Irradiation Room (IR)s offer different beam types and energy ranges [36, 35]:

- IR 1** This is the IR for non-clinical research. A fixed horizontal beam is used. Protons can be used in the energy range from 60-800 MeV and carbon ions from 120-400 MeV/u.
- IR 2** The first IR for patient treatment offers a horizontally and a vertically fixed beam. Protons from 60 MeV to 250 MeV can be used. Carbon ions are again available from 120 MeV/n to 400 MeV/n.
- IR 3** A horizontally fixed beam is used. Available particle energies correspond with the ones from IR 2.
- IR 4** Irradiation takes place through a proton gantry. Particle energies from 60 MeV to 250 MeV are available.

All IRs have a robotic positioning system so that results from non-clinical research can be applied and compared easier to patient treatment [36]. An overview of the IRs and the accelerator system can be seen in Figure 3.1.

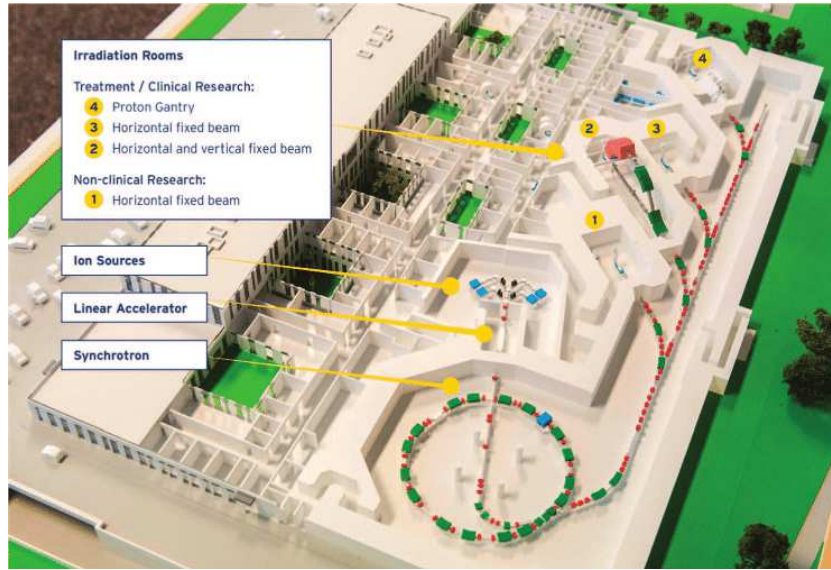


Figure 3.1: MedAustron facility [37].

The experimental setup (see [38]) that was used as a model for the simulations in this thesis can be seen in Figure 3.2. It consists of four silicon-strip-detectors with a side length of 25.6 mm and a thickness of 0.3 mm. First experiments for proton tracking as a basis for a full ion CT has already been done with this setup. This setup has been used until the middle of 2019 and is currently updated.

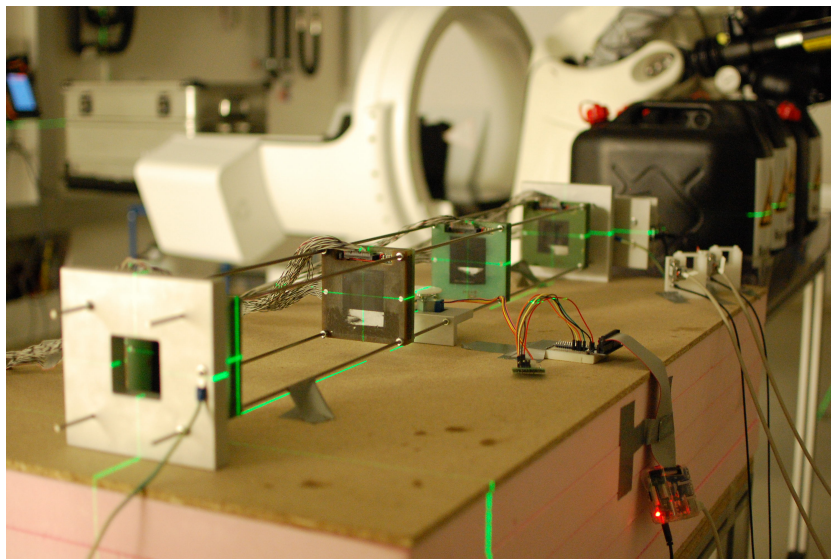


Figure 3.2: Experimental setup at MedAustron [39].

3.2 Software frameworks

In this Section a short overview on the software used for simulation of projection data (Geant4, ROOT), the application of reconstruction algorithms (TIGRE) and the post-processing (ImageJ) of the reconstructed data will be given.

3.2.1 Geant4

Geant4 [40] is a software toolkit written in C++ which was developed in 1993 by CERN and KEK. It uses a combination of composition and rejection Monte Carlo methods for the simulation of several particle physics problems. This method aims to solve a mathematical problem (such as particle transport through matter) by setting up a stochastic model using random numbers. The model can be understood by considering the basic principle of the Monte Carlo method for particle transport as presented in [41]. A particle moving through space travels short distances and is interrupted by events such as scattering or decay. There are n different events (E_1 to E_n) which the particle is sensitive to. The probability of each of these events to happen next is given by p_i so that

$$\sum_{i=1}^n p_i = 1. \quad (3.1)$$

The probability of an event can, for example, be defined by using its respective cross Section relative to the cross sections of all available events,

$$p_i = \frac{\sigma_i}{\sigma_t}, \quad (3.2)$$

where σ_i is the cross Section for an event i and σ_t is the total cross Section for all available events so that

$$\sigma_t = \sum_{i=1}^n \sigma_i. \quad (3.3)$$

Since only one of the n possible events can be selected as the one happening next, a random number ξ , where $0 \leq \xi < 1$, is chosen by a respective algorithm. ξ satisfies

$$p_1 + p_2 + \dots + p_{i-1} \leq \xi < p_1 + p_2 + \dots + p_i, \quad (3.4)$$

and can therefore be used to determine the event E_i . Using a Monte Carlo model as described above, Geant4 can be used in the fields of radiation physics, nuclear medicine, space science and other fields of particle physics which require complex detector simulations with a high number of particles. Due to the size and complexity of the software toolkit itself it was necessary to partition it into smaller pieces, leading to Geant4's modular and object-oriented structure. This simplifies the process of adding new parts to the software framework, parallel development and improves overall transparency and organization of Geant4. Because of that, the user is able to reuse most of the existing

code parts and only modifying some parts to his/her specific application needs. The substructures of the Geant4 framework are called class categories. The class categories are depending on each other in a hierarchical, uni-directional way. The class categories themselves contain classes with a close relationship [40, 42].

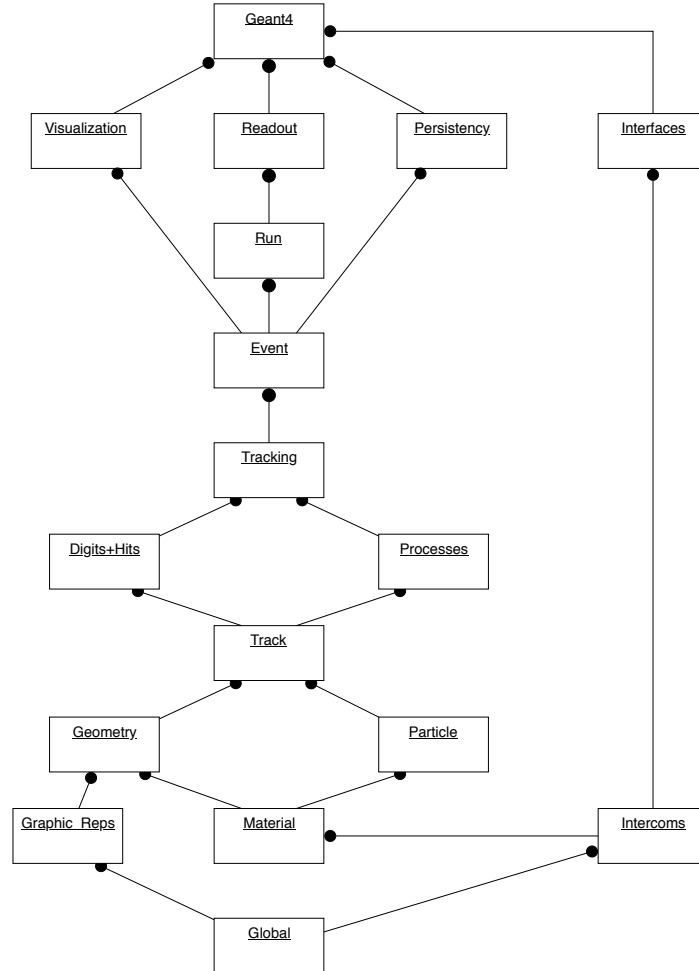


Figure 3.3: Geant4 structure [42].

Figure 3.3 shows an overview of Geant4 class categories. Bottom class categories are used by all virtually higher class categories. One bottom category is for example *Global*, which contains i.a. the unit system and constants. The next two layers contain *materials*, *particles*, *geometry representations* and *geometry*. These class categories include all features for the navigation in the geometry model and detector description. *Intercoms* allows the communication between modules that would usually not depend on one another, the interaction with Geant4 through the user interface and furthermore is a repository of abstract interfaces for plug-ins. The next layers of class categories

such as *track*, *processes* and *tracking* contain physical models to describe the physical processes that particles undergo as well as all features for the description of the particle tracking itself. *Event* collects the tracks from the categories below and *run* collects all events sharing the same beam and the same detector geometry. The top class categories contain all features for visualisation and user interfaces but also the *persistency* class category [40].

The circle in the diagram shows the direction of the dependency. The class category with the circle uses the attached class category [40].

In the following, some parts of the architectural design which are crucial to understand the behavior and structure of the Geant4 toolkit will be briefly described. A more detailed study on these aspects can be found in [40].

Events An event is defined through the generation of primary particles which are obtained through an abstract interface to external physics event generators. Since these generators are special classes which are not depending on one another, this allows the user to adapt the code to his/her own needs. This includes for example the change of beam parameters (such as angular distribution or initial particle energy) at run-time or implementing particles which are not treated by Geant4 (such as quarks) [40].

The event is the main unit of the simulation. Before the processing of the event it contains the information on the primary particles and vertices, after processing its objects include information obtained through the simulation such as hits, particle trajectories and digitisation. The user has to decide on which objects to save using his/her own conversion to persistent classes, since the class objects of the *Event* classes themselves are not permanently storable due to performance reasons [40].

Geometry and detector representation The *geometry* classes offer all features to create a physical environment and let particles propagate through it. When creating such an environment, the principle corresponds to that already existing in Geant3 (precursor of Geant4, written in FORTRAN [43]). A logical volume is an element of a certain shape that contains information independent on its location such as material or detector behavior. The physical volume is the actual placement of a logical volume in a global mother volume. Each logical volume can contain or be attached to other logical volumes. For enhanced memory efficiency, repetitive structures can be represented by specialised physical volumes [40].

A logical volume contains a separate entity defining the shape of it. Geant4 already offers code for simple shapes of such as spheres, boxes or cylinders, more complex shapes have to be defined by their boundary surfaces [40].

Tracking One focus of this class category has to lie on the overall performance, which is strongly depending on the time CPU spends for moving a particle by one step. In Geant4 particles are not considered as self-moving but are being transported by the eponymous transport process step-by-step. The *tracking* category steers the invocation of this process. Since physics processes are regarded in a generic way,

tracking does not depend on particle type or specific physics processes. To acquire the crucial tracking precision, the smallest value out of the maximum allowed step (defined by the user) and the proposed step value by all included processes is taken for tracking step size. Three different actions can be included in a physics process, which have to be handled by the *tracking* category: Actions for particles at rest (such as decay), along-step actions (energy loss or other phenomena which can happen continuously during a step) and post-step actions (such as decay or generation of secondary particles at the end of the step). The *tracking* has to scan all processes and including actions for a particle and decide on which have to be applied. The physics processes to be scanned can be influenced by the choice of the physics list in Geant4 [40, 42].

Physics Although all physics processes share the same basic interface, the sub-domains have been designed accordingly to the complexity of the process to be described. The actions that can be included in a physics process are [40]:

Particle decay The step length (or time for particles at rest) can easily be calculated from the mean life of a particle, whereas the generation of decay products is more difficult. Usually a decay mode corresponding to a particle is chosen from a decay table. For heavy flavour particles, two approaches are used for this problem: The external decayer approach, where a certain class attached to a particle decides type and momentum of secondary particles and the pre-assigned decay mode approach, where secondary particles are generated by the primary particle source and attached to their parent particles [40].

Electromagnetic physics This package consists of a set of categories describing and managing all electromagnetic interactions of leptons, photons, hadrons and ions such as bremsstrahlung, multiple scattering, photo-effect, ionisation, Compton scattering or Raleigh scattering. A detailed description of the physics of these processes can be found in the Geant4 *Physics Reference Manual* [9]. The package can be divided into six categories. The *standard* category describes basic electromagnetic processes of electrons, positron, photon and hadrons, *low energy* covers the processes where additional models have to be used due to the low particle energy. Muons, X-rays and optical photons are each treated in their own category with particle-specific code. The remaining category is the *utils* category, which collects utility classes used by the other categories [40].

Hadronic physics The aim of this code implementation is to describe hadronic interactions by providing the inclusive cross-sections and final state generation for given particles and materials. The way of receiving the cross sections can be a simple equation or a sophisticated parameterisation using large data tables. The cross-Section is then used to calculate the physical interaction step length [40, 42]. Underlying physical models used for the calculation were already described in Section 2.1 and can be found in [9].

Gamma-nuclear and lepto-nuclear processes These processes require hybrid models both containing hadronic and electromagnetic interactions. So far, interactions including neutrinos are not yet included in the framework [42].

Particles and materials This class categories include all information necessary to describe to interaction between particles and matter. These are for particles parameters such as charge, mass or cuts information. It is also defined to which physical processes the particle is sensitive. The definition of materials regards its elemental composition: the material can consist of one element or a mixture; the elements themselves can consist of a single isotope or a mixture of them. Physical properties of the material can be given directly through parameters such as density or can be calculated from the elemental composition. Elemental and isotope composition of a material are also used to calculate other parameters of interest such as the coefficients of the Bethe-Bloch formula [40].

3.2.2 ROOT

The ROOT framework [44] was developed in the scope of the CERN NA49 experiment [45], when old data analysis systems reached their limits at the processing of large amounts of data. Since the NA49 experiment produced about 10 TB of raw data per run, a new analysis tool had to be found which could benefit from the newly made progress in computer sciences at that time - especially in the field of object orientation [46, 47].

ROOT is written in C++ and offers a large set of possibilities for data analysis (such as histograms, fitting or error bars) but also the possibility to acquire data or do detector simulations, event generation or reconstruction [46]. As previously stated, it is an object-oriented framework and therefore intended to make it easier to extend and apply for the user because the majority of code should be reusable and only needs to be extended or adapted to the user's needs. The modular structure is intended to make this step easier and more clear. Still, the framework is developed in the so-called 'Bazaar Style', which relies on the user's - mostly physicists - diverse and deep talent [47].

The part of ROOT used in the scope of this thesis is the ROOT file format, since the data received from the simulations performed in Geant4 were stored in this file type. Since ROOT was intended to be used with large amounts of data, a special data structure has been implemented within ROOT: the so-called ROOT Tree. The Tree is designed to be memory-efficient and offer a fast access to the data. The so-called Leaf data of a Tree are stored in the branch buffers of the Tree and only written to the memory disk when a branch is full. Since the object to be compressed is a buffer containing a lot of same-class data, the compression can be made more efficiently than with individually memorized objects [47].

The ROOT Object Browser can be called directly from the command line and is a fast way to display acquired data in a user interface offering different plot options (2D and 3D presentation of data, histograms).

3.2.3 TIGRE

TIGRE, short for Tomographic Iterative GPU-based REconstruction toolbox [48], is a MATLAB/CUDA based toolbox which was originally intended for cone beam X-ray CT image reconstruction. The GPU (Graphics Processing Unit) is an additional computing unit that can be used to perform general-purpose computations outside of the central processor's traditional data processing pipeline. CUDA (Compute Unified Device Architecture) is a GPU architecture which was developed by the company NVIDIA [49]. The architecture is designed in a way to avoid limitations for general-purpose computations on a GPU which restricted previous graphic processors from being useful for such calculations [50].

From the underlying principle the intended X-ray CT reconstruction is equal to a simple SL ion CT reconstruction (with only the values resulting from reconstruction having a different meaning), particularly since the option of a parallel beam geometry has been added to the TIGRE toolbox. In both cases, 2D images of the object are taken from different angles and an algorithm is calculating the 3D image from the data [51].

TIGRE offers a large set of algorithms for image reconstruction, following the two standard methods (see Section 2.4): solving the inverse Radon transform (FBP or Feldkamp, David and Kress (FDK) algorithm) or solving a minimization problem (iterative algorithms). The first approach is fast and easy to calculate and performs quite well with ideal data (such as simulations). However, this method often only produces poor results for less ideal data (due to noise, lower image quality etc.). The latter approach is able to outperform FBP and FDK in the resulting image quality, however, the effort in computation is a lot more. This is a large problem for medical application, where images are needed rapidly and there is no time for calculations in the order of hours or even days. On the other hand, complicated algorithms that improve the computation performance are often difficult to understand and apply [51].

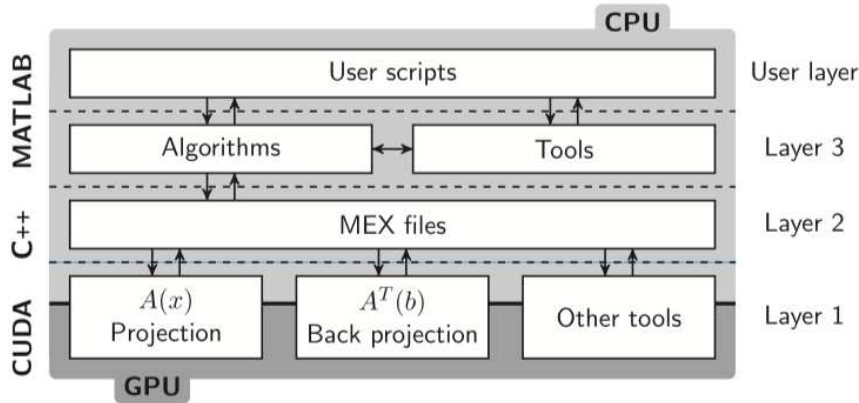


Figure 3.4: Structure of TIGRE [51].

The solution within the TIGRE toolbox is therefore to split the problem. The higher-level MATLAB is used to make algorithms easy to apply and to write while this layer is

connected via the communication layer to the underlying CUDA code, which contains projection and backprojection operators. The structure of TIGRE can be seen in more detail in Figure 3.4.

As already mentioned, Layer 1 contains the projection and backprojection operator, which are used for iterative reconstruction. The projection operator is for the intended use of X-ray CT a matrix that contains a linearization of a model which describes the photon attenuation (or, for ion CT, the material parameter α) measured over the given projection area. The backprojection operator can be interpreted as 'smearing' over the projection area with a weighting factor [51].

There are many different approaches to obtain the projection and backprojection operators. In TIGRE, two methods have been implemented to obtain the projection operator: The first one is the voxel-ray intersection, which is based on the Siddon ray-tracing algorithm [52]. The distance between a voxel and an infinitesimally narrow X-ray beam is calculated and multiplied by the voxel intensity. However, this can lead to problems with a larger voxel size due to discretization square-block artefacts coming from the finite size of the voxels. Therefore, the second method has been implemented: In trilinear interpolation, the path is evaluated at every given Δl and image values are calculated using interpolation with advanced texture memory. Δl can be set through the variable *geo.accuracy* which should be 0.5 or lower. This value sets Δl as a fraction of the actual voxel size. To obtain the backprojection operator, two similar approaches are used. In both of them, the ray from source to a specific voxel and then to the detector is calculated. Then, bilinear interpolation is used to read the given value and attach it with a weight to the voxel. The weight is now different for both approaches: Either the FDK weight is applied or a matched weight, which is crucial for the use of Krylov subspace methods, is used [51].

While Layer 3 of TIGRE is optimized for GPU computing using CUDA, Layer 2 is the communication layer and written in C++. The so-called MEX-functions are connecting Layer 1 with Layer 3, in which the algorithms are coded in the high-level language MATLAB [51].

TIGRE introduces four main reconstruction algorithm families (for a detailed description of filtered backprojection and SART-type family, please consider Section 2.4) which are [51]:

Filtered backprojection family In TIGRE, only the FDK algorithm is implemented.

SART-type family SIRT, OS-SART and SART are implemented.

Krylov subspace method family The conjugate gradient least squares (CGLS) is implemented. This method family represents methods to solve linear equations based on the iteration through Krylov subspaces and minimization of eigenvectors in the descending orders. A Krylov subspace is hereby defined by the linear combination of the k first powers of A acting on b (see also Equation (2.39)),

$$K_r(A, b) = \text{span}\{b, Ab, A^2b, \dots, A^{k-1}b\}. \quad (3.5)$$

Total variation regularization family ASD-POCS, OSC-TV, B-POCS-TV- β and SART-TV are implemented. They offer a lot more parameters to adjust and therefore often need to be tested several times. They use one of the previously mentioned algorithms to minimize the data and afterwards minimize the total variation. The difference between the given algorithms lies within the tools used in the minimization steps.

On top of these layers, there is the user layer, which allows to write scripts using the already existing algorithms and all other underlying layers.

For this thesis, only the MATLAB implementation of TIGRE has been used. However, there is already a fully supported Python version which could be used for future application [53].

3.2.4 ImageJ

ImageJ [54] is a public domain Java program for analysis, editing and processing of images. Since it runs on Windows, MacOS and Linux and can open the most spread medical image data formats it has been considered a suitable tool to display the images obtained through the reconstruction process. The image formats that are initially supported are TIFF, GIF, JPEG, PNG, DICOM, BMP, PGM and FITS. Many other image types can be opened with plugins or via the RAW option (such as Interfile) [55].

Many Plugins have been developed for ImageJ so far. In order to not have to install many of them manually, there is already an ImageJ distribution called Fiji [56] ('Fiji is just ImageJ'). Its installation already contains Java, Java 3D and a set of useful plugins [55].

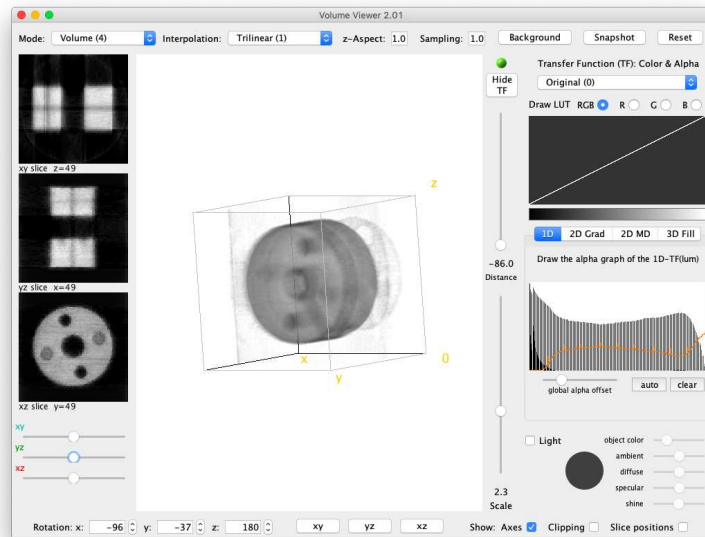


Figure 3.5: ImageJ Volume Viewer.

Opening the DICOMs obtained through the reconstruction in TIGRE, ImageJ starts a 2D view of the single image slices. The direction of the cuts (i.e. the axis) can be changed in the menu. A toolbar allows to make selections, draw, zoom and other features. Using this toolbar, a part of the image can be selected and the respective grey values can be extracted from the image using it in combination with the menu option 'Analyze' [55].

The plugin *Volume Viewer*, which is already pre-installed in Fiji offers the possibility to display the reconstructed object in 2D slices and in 3D at once. Figure 3.5 shows a screenshot of the viewer.

On the left side, the slices along the xy -, xz - and yz -planes can be seen and selected via scroll bar (bottom). In the middle, the object is shown in 3D. The rotation angles can be changed and an offset can be defined, so that the object can be better separated from the background.

3.3 Reconstruction process

After introducing the tools that have been used in the scope of this thesis in Sections 3.2.1 to 3.2.4, this Section now gives a general overview on how these tools can be used and work together to conduct a whole image reconstruction, beginning from the simulation process. The whole process of image reconstruction for ion CT can be summarized in five steps, as it can be seen in Figure 3.6. These steps will be discussed in detail in the following.

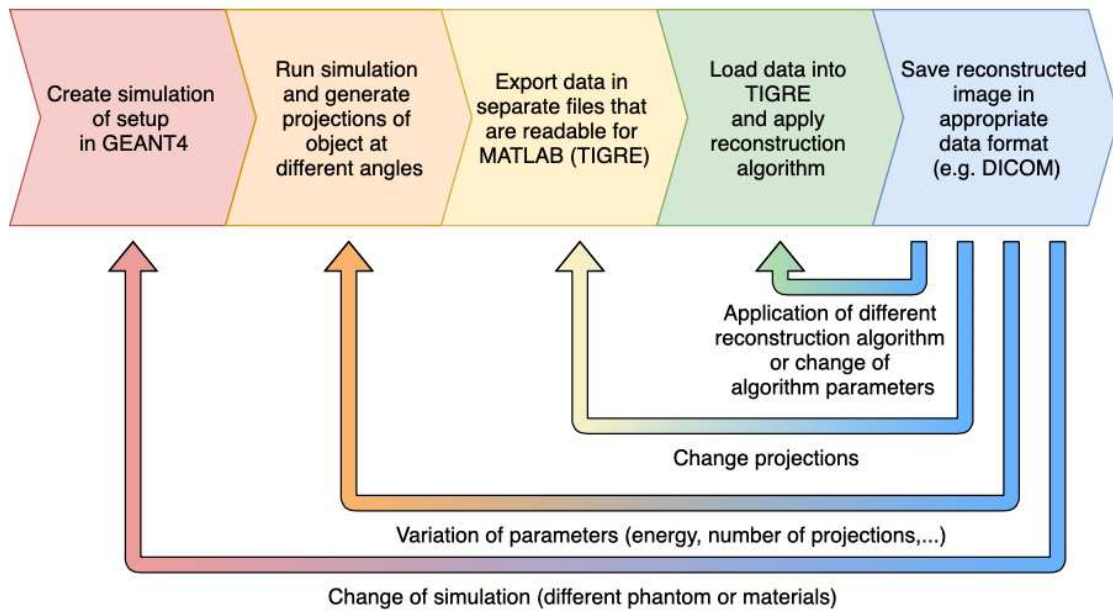


Figure 3.6: Overview of image reconstruction process.

3.3.1 Experimental setup with Geant4

For the modelling of the experimental setup in Geant4, the simulation already used in [57] has been used as a starting point and adapted to the needs of the image reconstruction. The simulation already contained four silicon detectors in the correct size (2.56 cm × 2.56 cm). The most important adaptations that have been made are:

Beam geometry The original simulation had a beam shape representing the actual one at MedAustron, which is a Gaussian distribution with a standard deviation $\sigma = 0.175$ cm [57]. However, this geometry was changed to a more ideal one for the simulations in this thesis. The initial particles are now equally distributed over the whole detector area (an area of 2.56 cm × 2.56 cm), so that the phantom is evenly irradiated. As in the old simulation, a parallel beam geometry was chosen.

Phantom A phantom was added to the simulation. Since two pieces of the Pololu mounting hub [58] have already been irradiated once at the MedAustron experimental setup and since they provide some internal structure, they were considered to be a suitable object for the initial reconstructions. The mounting hubs are made from Aluminium, they were connected through a plastic filling (NYLON-6-6) going through two of the mounting hub holes. One of the mounting hubs has a diameter of 19 mm and a thickness of 5 mm. The real object and the simulated version can be seen Figure 3.7.

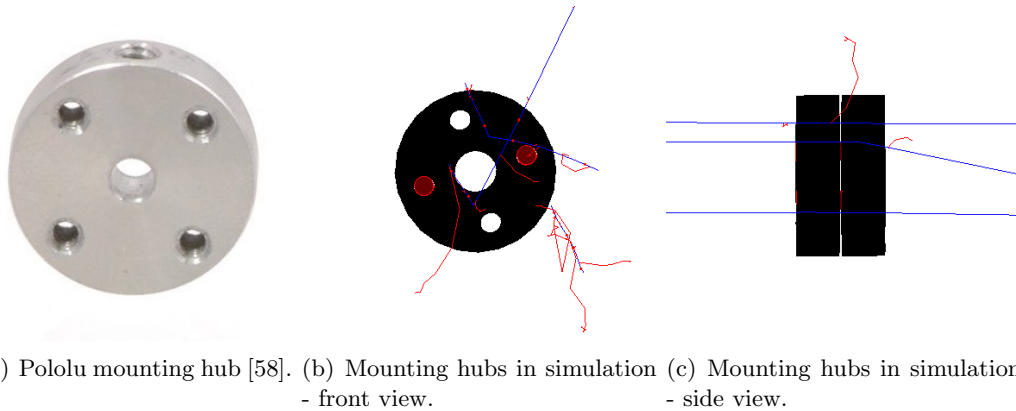


Figure 3.7: Initial phantom in the Geant4 simulation.

Phantom rotation In order to do projections at different angles easily and automatically, a new user interface (UI) command had to be written. The Geant4 UI manager has been used to create the respective command that could then be implemented to a macro file that starts several runs of the simulation at different irradiation angles.

Newly stored data To prepare the crucial values needed to create the projections after the actual simulation, a simple SL approach, similar to the one presented in [59]

was used within the Geant4 model. Although there are four detectors in the simulation (in reality a particle trajectory is only stored if the particle hits all four detectors, which was kept the same in the simulations), only the particle positions on detector 2 and detector 3 (see Figure 3.8) are used. The difference of the hit position on detector 2 and detector 3 is calculated according to

$$d_x = \text{abs}(\text{hit position}_{d2,x} - \text{hit position}_{d3,x}), \quad (3.6)$$

$$d_y = \text{abs}(\text{hit position}_{d2,y} - \text{hit position}_{d3,y}), \quad (3.7)$$

where d_x and d_y are the difference in mm between the hit position on detector 2 (hit position_{d2,x/y}) and detector 3 (hit position_{d3,x/y}) in x and y direction. An additional value, the tolerance $t_{x,y}$ is implemented. The ion path is regarded as straight if the following inequalities are fulfilled:

$$d_x < t_{x,y} \quad (3.8)$$

$$d_y < t_{x,y} \quad (3.9)$$

The tolerance was set as a default to 1 mm. If Equation (3.8) and Equation (3.9) are not fulfilled, the ion path is neglected. Otherwise, the ion path is defined as a SL parallel to the z-axis and with the following x and y coordinates, calculated as an average of the hit position vectors on detector 2 and detector 3,

$$\text{Position}_{x,y} = \frac{(\text{hit position}_{d2} + \text{hit position}_{d3})}{2}. \quad (3.10)$$

Since the silicon strip detectors used at MedAustron have a strip width of 50 μm in x direction and a width of 100 μm in y direction, the Position_{x,y} has to be modified to the particle strip position that is given according to

$$\text{Strip}_x = \text{Int}((\text{Position}_x + 0.5 \cdot \text{Detector Dimension}_x) / \text{Pitch}_x), \quad (3.11)$$

$$\text{Strip}_y = \text{Int}((\text{Position}_y + 0.5 \cdot \text{Detector Dimension}_y) / \text{Pitch}_y), \quad (3.12)$$

where Strip_{x/y} is the strip number, position_{x/y} is the calculated particle hit position from Equation (3.10) in the global Geant4 coordinate system, detector dimension_{x/y} is the size of the detector and pitch_{x/y} is the size of one strip. Each of these values is defined for x- and y-directions (orthogonal directions to beam axis).

Checking Equation (3.8) and Equation (3.9) for each ion hitting the detectors, two additional hit maps have been added to the Geant4 simulation. The first one (H1) collects the number of particles per area (number of hit positions per pixel) over the area of a detector (2.56 cm \times 2.56 cm) using the resulting Strip_{x,y} values obtained from Equation (3.10) to Equation (3.12). The second hit map (H2) displays the accumulated residual particle energy of all the particles that are already displayed

in the first hit map at the same pixels as H1. The values for the residual energy are taken from a measurement directly at detector 3. This is a simplification of reality, since no energy measurement device has been added to the real setup at MedAustron and therefore the measurement of the residual energy is regarded as an ideal one that takes place directly at detector 3 in the simulations. The hit maps H1 and H2 are defined with a size of 128×128 pixels, which means that one pixel has a size of $0.2 \text{ mm} \times 0.2 \text{ mm}$.

Multithreading Geant4 allows to assign different jobs of a simulation to several cores. This reduces the running time of the simulation which is a crucial step when a high number of primary particles and a large number of projections is used.

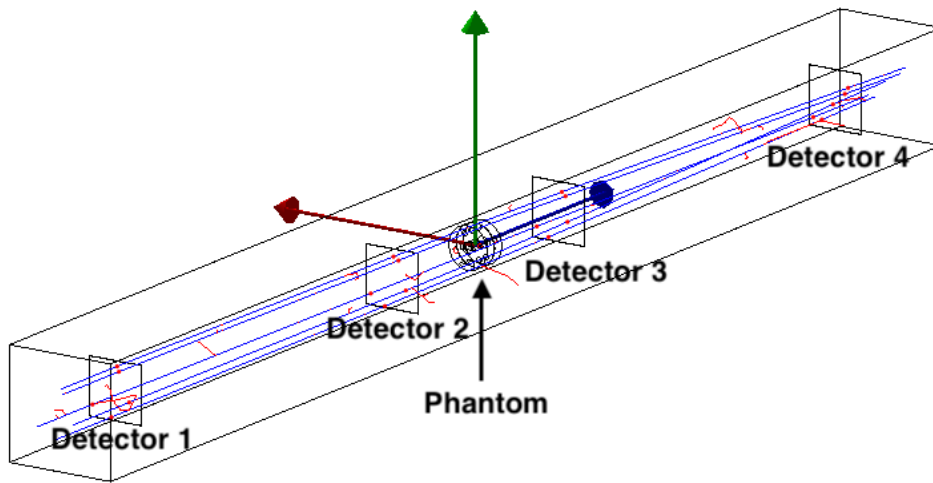


Figure 3.8: Experimental setup in Geant4.

The resulting geometry can be seen in Figure 3.8 as it is displayed in the Geant4 visual mode.

3.3.2 Generation of data

The simulation was run on a server of the Institute of High Energy PHYSics (HEPHY) with 48 cores (Intel(R) Xeon(R) CPU E5-2650 v4 @ 2.20GHz). A simulation of 90 projections and 5×10^5 protons per projection took about 25 minutes. Since the executed macro file that runs through all the projection angles and starts a new run in Geant4 after each angle, no further input is needed during the simulation.

3.3.3 Creation of projections

The projections are created after the actual simulation. This process could be included in the simulation itself in the future. However, it was decided to leave this as a separate

step so that it would not be necessary to run the whole simulation again if only a change in the projection values (e.g. use of a different function to display the projection values) is needed.

To read out the crucial values from the ROOT file that contains the simulation data (see also Section 3.3.1), an additional C++ file was written. Two hit maps have to be read out: one containing number of ions that hit a certain pixel and one that contains the accumulated residual energy of all these ions per pixel. The average residual energy per pixel can then easily be calculated using

$$E_{\text{res,avg}}(x, y) = \frac{E_{\text{total}}(x, y)}{N_{\text{total}}(x, y)}, \quad (3.13)$$

where $E_{\text{res,avg}}(x, y)$ is the average residual energy at a certain pixel measured at detector 3, $E_{\text{total}}(x, y)$ is the accumulated residual energy of all ions that hit the respective pixel and $N_{\text{total}}(x, y)$ is the total number of particles that hit pixel (x, y) . As it was shown in Section 2.2.3, the projection value a pixel can finally be defined as

$$p(x, y, \theta) = E_{\text{init}}^{1.7} - E_{\text{res,avg}}(x, y, \theta)^{1.7}, \quad (3.14)$$

where $p(x, y, \theta)$ is the projection value for an angle θ at a certain pixel with x and y coordinates, E_{init} is the initial particle energy and $E_{\text{res,avg}}(x, y, \theta)$ is again the average residual energy at a certain pixel measured at detector 3. The projection values are stored in *.txt* files since they can be read and processed by MATLAB.

The tolerance value $t_{x,y}$, that was introduced in Equation (3.8) and Equation (3.9), was set to three different values: 0.5 mm, 1 mm and infinite tolerance. The object that was already presented in Section 3.3.1 was then irradiated in the simulation at 0° , 45° and 90° using 10^6 primary protons with an energy of 100 MeV to receive a first comparison of projections generated with different values of $t_{x,y}$ (whereas for a full reconstruction, more projections would be needed). The projections taken at 0° is shown in Figure 3.9, the projections at other angles can be found in the Appendix.

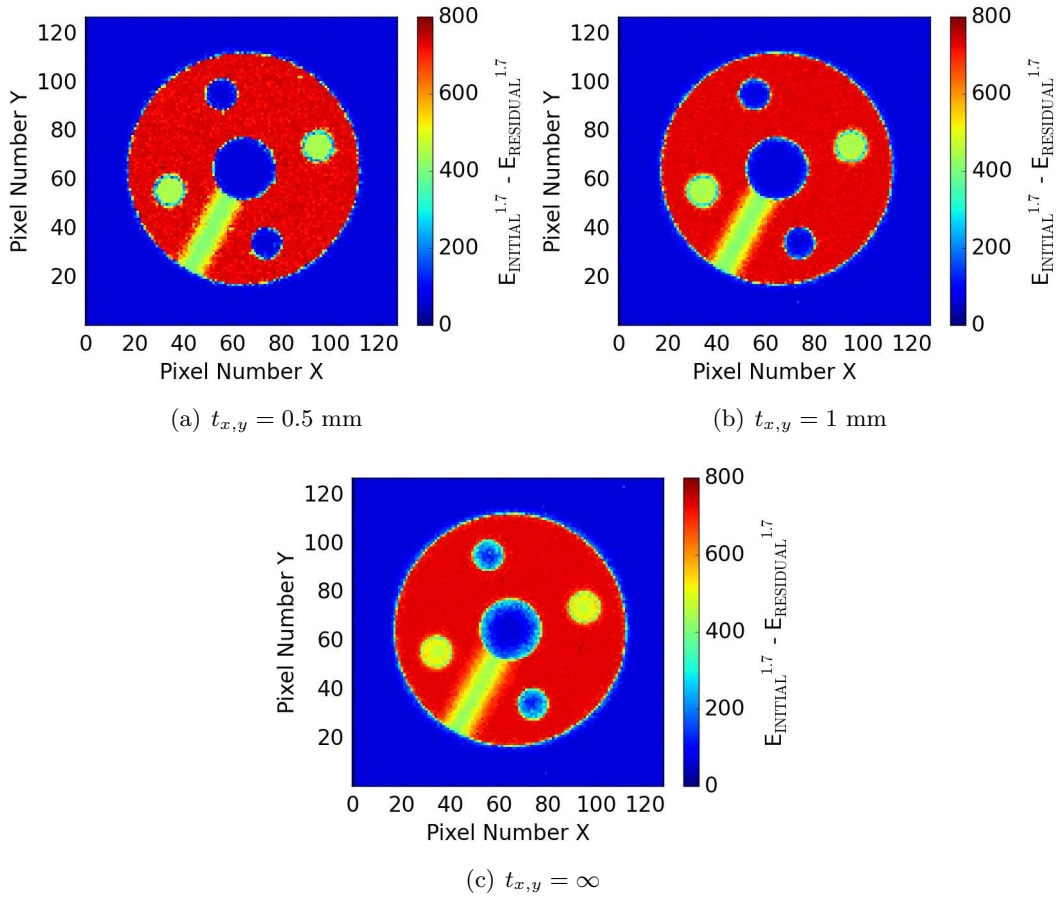


Figure 3.9: Projections with 10^6 protons at 100 MeV at 0° using different values for $t_{x,y}$ (projections according to Equation (3.14)).

Figure 3.9 shows that edges and small structures can be seen clearer if $t_{x,y}$ is set to a smaller value (especially at the small air-filled holes within the object). However, for $t_{x,y} = 0.5$ mm, only approximately 235.000 from the original 10^6 protons could be used for the projections since they fulfill Equation (3.8) and Equation (3.9). For $t_{x,y} = 1$ mm, about 500.000 protons could be used for the projections. For $t_{x,y} = \infty$, 735.00 protons contributed to the projections (the remaining ones did not hit all four detectors and were therefore not used). Not to lose too much information by rejecting many ion paths but also receive qualitative projections, $t_{x,y}$ was therefore set to 1 mm for further projections.

Another simulation with the fixed value for $t_{x,y}$ was performed. Again, the object was irradiated at 0° , 45° and 90° with 10^6 initial protons. This time the initial particle energy was changed for each simulation run. Results at an angle of 0° can be seen in Figure 3.10.

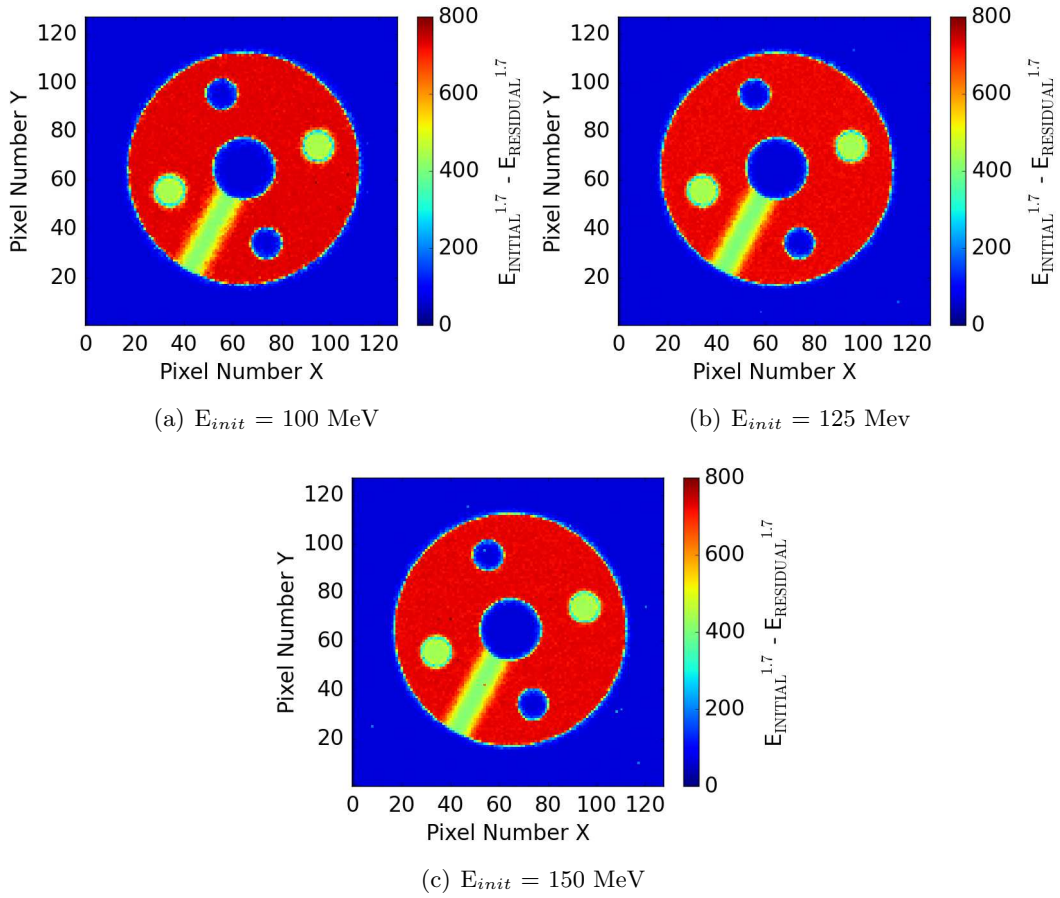


Figure 3.10: Projections with 10^6 protons at different energies at 0° ($t_{x,y} = 1$ mm, projections according to Equation (3.14)).

These simulations were performed in steps of 25 MeV from 75 MeV to 175 MeV. The lower limit was chosen because at 50 MeV, not enough particles could transfer the object with a small enough deviation from a SL to generate a projection. The results from all angles and energies can be found in the Appendix. Figure 3.10 shows no remarkable difference between the variation of the initial particle energies. This can be explained by the energy interval and small distances (small phantom) used, in which the absolute energy loss is very similar for all initial particles. However, a difference can be seen if, for comparison, the projection values are changed to the average relative energy loss:

$$E_{\text{loss,rel}}(x, y, \theta) = \frac{E_{\text{init}} - E_{\text{res,avg}}(x, y, \theta)}{E_{\text{init}}}, \quad (3.15)$$

where $E_{\text{loss,rel}}(x, y, \theta)$ is the average relative energy loss of a particle for a projection pixel (x, y) taken at the angle θ , E_{init} is the initial particle energy and $E_{\text{res,avg}}(x, y, \theta)$ is the residual particle energy as already defined in Equation (3.14).

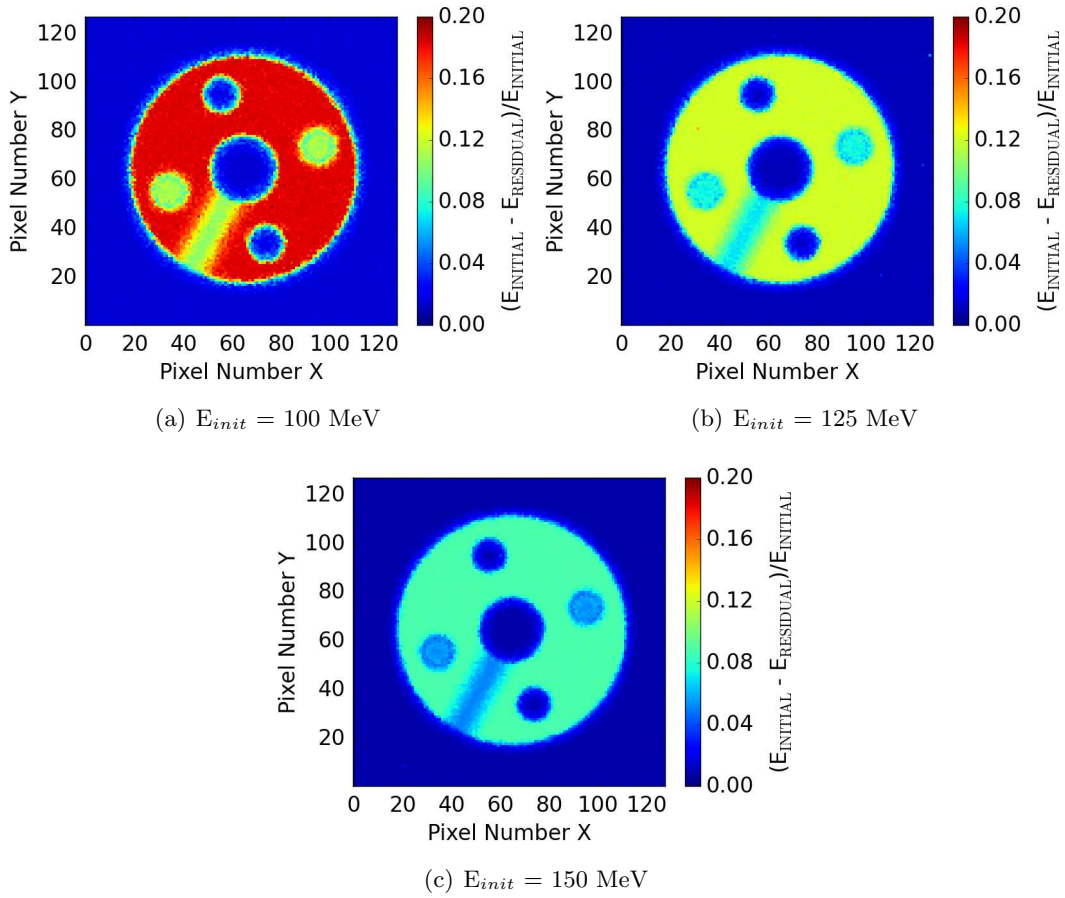


Figure 3.11: Projections with 10^6 protons at different energies at 0° ($t_{x,y} = 1$ mm, projections according to Equation (3.15)).

The results shown in Figure 3.11 are again given for projections simulated at 0° , other angles can again be found in the appendix.

It was decided to generate all further projections and perform the subsequent reconstruction of this object for protons with 100 MeV, since the first simulated projections already delivered radiographs with the phantom clearly visible. Furthermore, this proton energy was chosen for comparison reasons with other methods, since the object has already been irradiated at this energy at MedAustron. A radiography for the real data as well as for simulated data has been generated using the proton scattering angle distribution within the object and can be found in [38].

3.3.4 Reconstruction in TIGRE

The reconstructions were run on a GPU server, using one of four Nvidia Geforce GTX 1080 Ti (3584 kernels each).

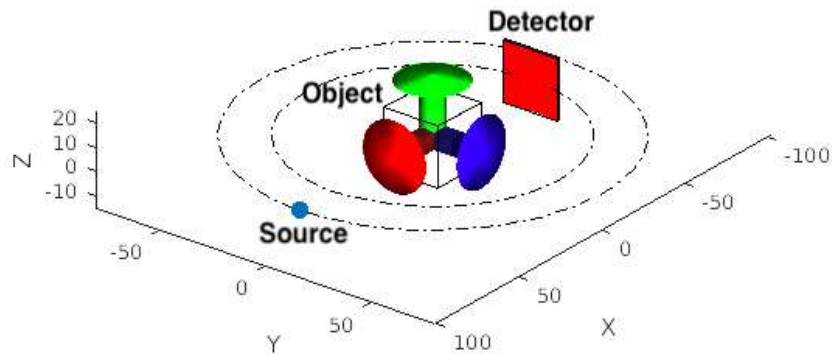


Figure 3.12: Geometry definition in TIGRE.

For a SL approach, TIGRE has already implemented all necessary features for a full reconstruction. Only MATLAB code is needed for application. As a first step, the geometry of the setup has to be defined. Only one detector is defined (the one where the projection is measured). Distances between particle source, object and detector have to be defined. This is an important step for cone beam CT, since the reconstructed object would have the wrong size after the reconstruction if the distances are not given correctly. But also for the parallel beam type that was used for the ion CT, these parameters have to be set. Furthermore, detector size and reconstruction volume as well as voxel and pixel sizes (all of them in mm) have to be defined, which can be seen in the following code fragment. Optional parameters as well as offsets have been removed from the code fragment.

```

geo.DSD = 140;           % distance source-detector
geo.DSO = 80;           % distance source-origin

geo.nDetector=[128; 128]; % number of pixels
geo.dDetector=[0.2; 0.2]; % size of each pixel
geo.sDetector=geo.nDetector.*geo.dDetector; % total size of the detector

geo.nVoxel=[128;128;128]; % number of voxels
geo.sVoxel=[25.6;25.6;25.6]; % total size of the image
geo.dVoxel=geo.sVoxel./geo.nVoxel; % size of each voxel

... % offsets etc.

geo.mode='parallel'; % or 'cone'
plotgeometry(geo,0); % plot geometry

```

The given code results in a simple geometry consisting of source, object and detector and can be seen in Figure 3.12, with the arrows describing the local coordinate system in TIGRE.

After the geometry definition, the projections need to be loaded in the TIGRE folder and an algorithm can be applied. The actual reconstruction command is then only a one-liner as it can be seen in the next code snippet.

```
addpath('Projections');           % add path to projections
for index = 0:59
    ...                             % defining projection names
                                   % for correct loading
    result_array(:,:,index+1) = load(projectionname);
end;

im = single(result_array);         % correct datatype for reconstruction
angles = [0:3:177]*pi/180;        % define the angles

% apply FDK algorithm and plot result
imgFDK = FDK(im, geo, angles);
plotImg(imgFDK, 'Dim', 'Z');

% apply SART algorithm and plot result
imgSART = SART(im, geo, angles, 20);
plotImg(imgSART, 'Dim', 'Z');

% apply OS-SART algorithm and plot result
imgOSSART = OS_SART(im, geo, angles, 5, 'BlockSize', 10, 'Init', 'none');
plotImg(imgOSSART, 'Dim', 'Z');
```

The result of the reconstruction is then a MATLAB 3D array which can be stored in any other data format afterwards. For medical images, DICOM or Interfile offer a good possibility for data storing.

3.3.5 Analysis of reconstruction data

The data resulting from the TIGRE reconstruction was exported in 16-bit DICOM files which can then again be opened and analyzed with Fiji. 3D models and sectional views can be generated. Furthermore, grey values of areas of interest can be exported in a *.csv* file and the stopping power can be approximately calculated according to Equation (2.6) in Section 2.1.

After all these steps, one reconstruction is finished. Depending on the outcome of the steps before, there are several options:

- The reconstruction was already successful and delivered the necessary results.

- The reconstruction algorithm did not deliver the expected output but the simulation data does not have to be changed. Therefore (or simply for comparison) a different reconstruction algorithm is applied.
- The projection itself can be changed without changing or running the whole simulation again by simply changing the function in the C++ file that generates the projection values.
- The simulation has to be repeated with other simulation parameters (primary particle energy, number of projections or number of primary particles can be changed). Again, this can be done for comparison reasons or due to a non-satisfactory reconstruction result. These changes can be done by simply editing the macro file which defines the simulation parameters.
- The setup itself can be changed. Therefore, the Geant4 C++ code has to be edited in some way. This can be the case if another phantom is going to be irradiated or if the phantom material should be changed.



Die approbierte gedruckte Originalversion dieser Diplomarbeit ist an der TU Wien Bibliothek verfügbar.
The approved original version of this thesis is available in print at TU Wien Bibliothek.

4 Results and discussion

In the following Sections, the results of the reconstruction process will be presented. In Section 4.1, the projections, that were generated according to Equation (3.14) and using protons as primary beam particles, were reconstructed using different algorithms. To show the differences of the algorithms, a phantom with an internal structure/several materials was needed, which is why two of the Pololu mounting hubs, that were already presented in Section 3.3.3 were used. Since it could be shown that the OS-SART provides a good image quality, this algorithm was used in the subsequent Sections. In Section 4.2, the number of initial ions used per projection and the total number of projections used for the reconstruction were varied (60 or 90 projections). With this preparatory work, the algorithm was finally applied to simple cylindrical phantoms of one or more materials to determine the stopping power of these phantoms. The results of these reconstructions can be found in Section 4.3.

4.1 Application of different algorithms in TIGRE

Although TIGRE offers an even larger set of algorithms, three of them could be seen to handle the proton CT projections best. The reconstruction results of these algorithms will therefore be presented and compared in the following. For each reconstruction, 90 projections (0° to 178° in steps of 2°) and 5×10^5 protons with an initial energy of 100 MeV were used.

Table 1 shows the computation time (on the Nvidia Geforce GTX 1080 Ti) of different reconstruction configurations that were performed in the scope of this thesis. The configurations depend on the algorithm and its parameters as well as on the number of projections.

Algorithm	Iterations	Blocksize	Nr. of Projections	Runtime
OS-SART	5	10	90	21s
OS-SART	5	10	60	12s
OS-SART	5	5	90	36s
OS-SART	20	10	90	1min 20s
OS-SART	20	5	90	2min 24s
SART	5	/	90	2min 56s
SART	20	/	90	11min 47s

Table 1: Computation time of SART and OS-SART changing algorithm parameters and number of projections

The first algorithm that was applied to the projections was a simple FDK algorithm, which is actually the FBP implementation for a cone beam shape. However, if the parallel beam mode is selected in TIGRE, the reconstruction also works with this algorithm.

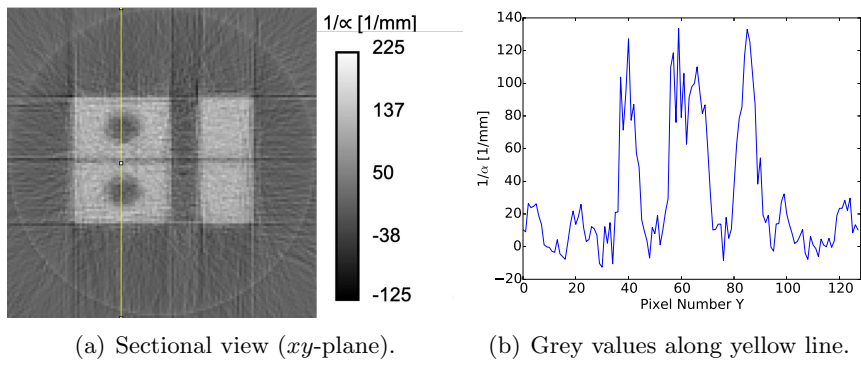


Figure 4.1: FDK algorithm, slice $z = 36$.

Figure 4.1 and Figure 4.2 show sectional views of the reconstructed object. One sectional view actually represents the DICOM values of 128×128 voxels of the size of $0.2 \text{ mm} \times 0.2 \text{ mm} \times 0.2 \text{ mm}$. Two slices (xy -plane at $z = 36$ and $z = 60$) were selected for the representation of the phantom. It has to be noted that the coordinate system used in TIGRE and ImageJ is different to the one in GEANT4. The z -axis defines the axis from bottom to top of the phantom (so the presented sectional views are the xy -plane) and y -axis is the axis of beam direction.

The first sectional view of the reconstructed image to be shown is the xy -plane at $z = 36$. This slice was selected, because it very well shows some of the substructures of the irradiated object. The yellow line in Figure 4.1 (a) runs through the air outside the phantom, through the aluminium part, the two side air drills and the the small air gap between the two mounting hubs. In Figure 4.1 (b), the grey values - which represent the reciprocal of the material parameter α - along this yellow line, can be seen.

The grey values show that the aluminium parts can be differentiated from the background. However, the curve is not very smooth which makes it hard to define exact borders of the object or to determine small structures like the small air gap between the mounting hubs.

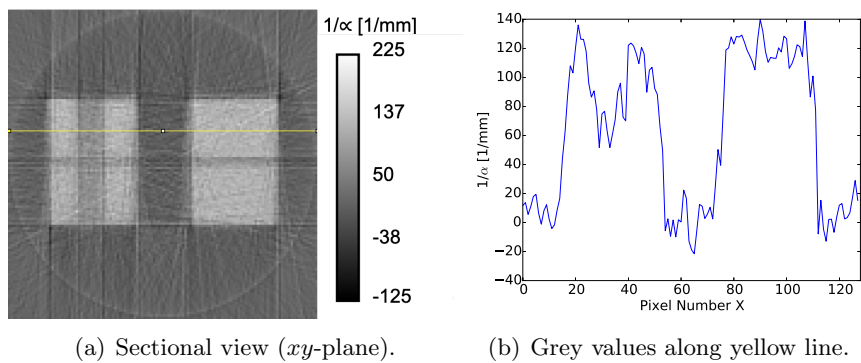


Figure 4.2: FDK algorithm, slice $z = 60$.

The second sectional view of the reconstructed image to be presented is slice $z = 60$. This xy -plane was selected since it not only contains the aluminium parts of the mounting hubs but also the plastic filling. Again, the grey values along the yellow line in Figure 4.2 (a) are shown in Figure 4.2 (b). The reciprocal of α should be lower for nylon than for aluminium, which can be seen in the curve of the grey values by a decrease and subsequent increase of the value in an area between $x = 20$ and $x = 40$. However, the curve is once again not very smooth which makes it difficult to determine the exact size of the plastic filling using this algorithm.

Another problem of the FDK algorithm is, that due to the missing iteration part to refine the image, the grey values cannot be used to define the material parameter α , because the reconstructed values in the image are not determined accurately enough. This can be seen if, for example, the air around the object is investigated. According to [60] and [25], the value of α should be around 30 mm for air for protons with an energy of 100 MeV. Since the reciprocal of the material parameter is obtained in the reconstruction, a value close to zero ($1/30 \approx 0.033$) should be received through the reconstruction process. However, the value for the air area can be seen to go up to a value close to 20 multiple times and sometimes even fall to a value under zero.

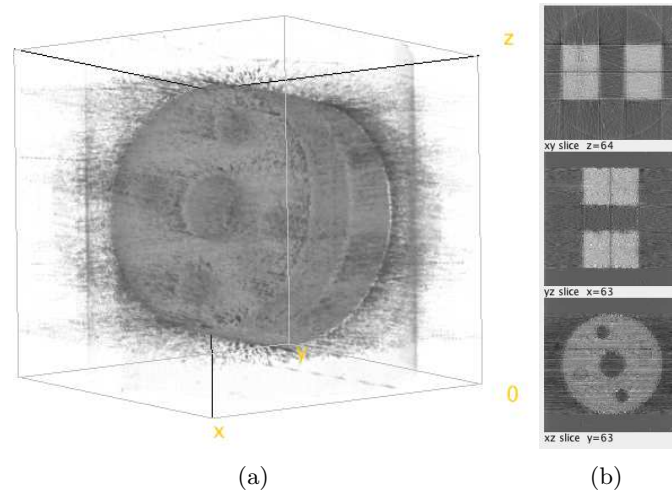


Figure 4.3: 3D representation (a) and sectional views (b) of FDK reconstruction (created with ImageJ Volume Viewer).

Finally, a volume representation of the reconstructed object was created with ImageJ. This 3D object and the xy -, yz - and xz -sectional views in the middle of the object can be seen in Figure 4.3 (a) and (b). As it could already be predicted from the previous cross-sections, the air background of the object is a little blurry. However, the original object can be clearly seen in the reconstruction.

The second algorithm that was applied is the SART, which offers the possibility to change the number of iterations to influence and improve the final result. With regard to later clinical application, the number of iterations was set to 5, since time is one of

the key parameters of the reconstruction. However, a reconstruction using 20 iterations can be found in the Appendix. The computing time for the algorithms can be found in Table 1.

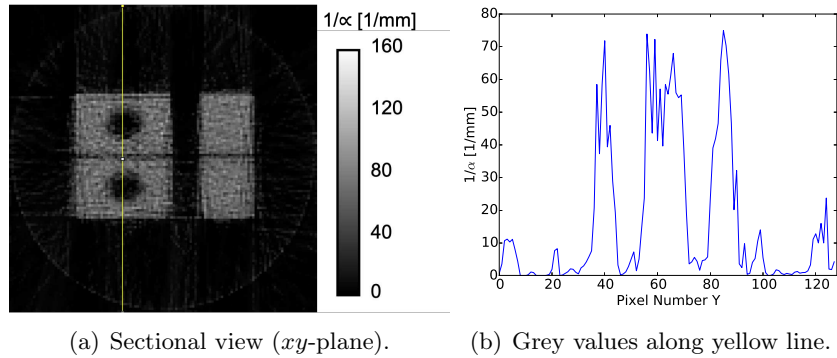


Figure 4.4: SART, slice $z = 36$.

Again, the slices $z = 36$ and $z = 60$ (Figure 4.4 (a) and Figure 4.5 (a)) are shown as a representation of the reconstructed object and grey values along the yellow lines are depicted in Figure 4.4 (b) and Figure 4.5 (b). In contrast to the FDK algorithm, the reciprocal values for α are now a lot more accurate. In the area of air around the object, the curve shows some outliers (in particular at the edges) but are over all a lot smaller than with the previous algorithm. Furthermore, there are no negative values for $1/\alpha$. The grey value for aluminium fluctuates around a value of approximately 70, which is the right order of magnitude (see Section 4.3) for the reciprocal of the material parameter. However, it is unfavourable that no smooth curve is received with the algorithm, which makes it hard to define the borders of the object and its substructures.

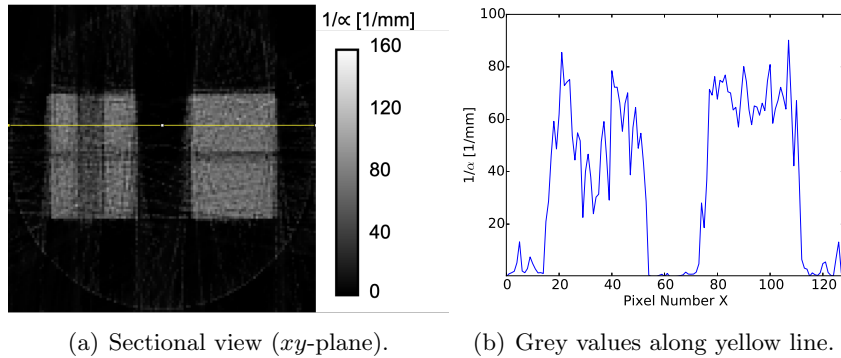


Figure 4.5: SART, slice $z = 60$.

Figure 4.6 shows again a 3D representation of the reconstructed object and the central sectional views. In contrast to the FDK algorithm result, the object does not blend in that much with the surrounding air material. However, the effect that the grey value is

higher at the borders - as it was seen in Figure 4.4 and Figure 4.5 - results in the upright cylindrical shape surrounding the actual object as a side effect of the algorithm.

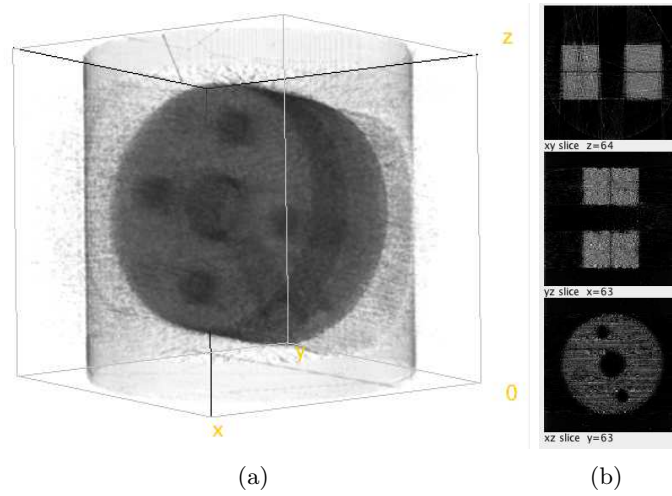


Figure 4.6: 3D representation (a) and sectional views (b) of SART reconstruction (created with ImageJ Volume Viewer).

The last algorithm that has been applied was the OS-SART. To be time-efficient, the number of iterations was again set to 5, block-size was determined to be 10. Other combinations can be found in the Appendix and the approximate computing time is again given in Table 1.

The results of the reconstruction are shown in Figure 4.7 and Figure 4.8. Compared to the FDK algorithm and SART, a really smooth curve is obtained using OS-SART. Regarding the sectional view of $z = 36$, even the small air gap between the two mounting hubs can be seen (at the area of $y = 64$ in Figure 4.7 (b)).

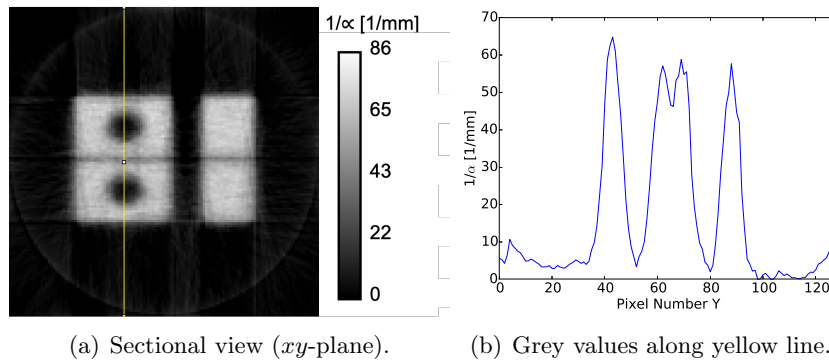


Figure 4.7: OS-SART, slice $z = 36$.

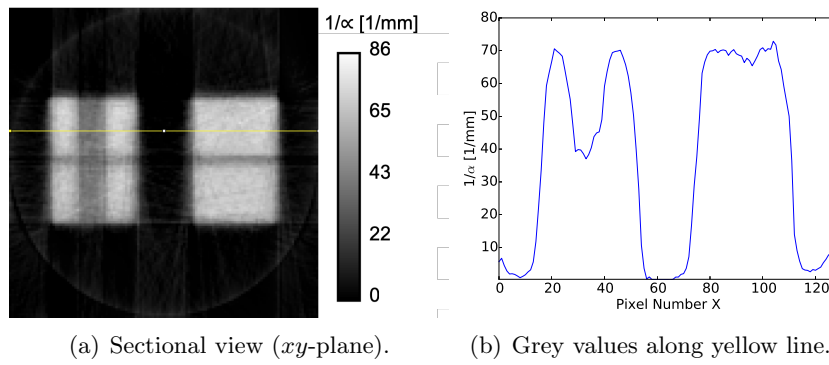


Figure 4.8: OS-SART, slice $z = 60$.

Figure 4.8 shows that there is a clear difference between the aluminium and plastic material within the phantom. This can be seen by the drop of the grey value in the respective area from approximately 70 to 40.

Both sectional views show a similar effect as the SART reconstruction at the edges, namely that the grey values are increased in that area. This can again be seen in the 3D representation of the reconstructed object (Figure 4.9) as the cylindrical shape surrounding the reconstructed object. Nevertheless, this algorithm was regarded as the most promising one for further reconstructions, since it is faster than SART but generates a smoother result with the gray values being in the correct scale.

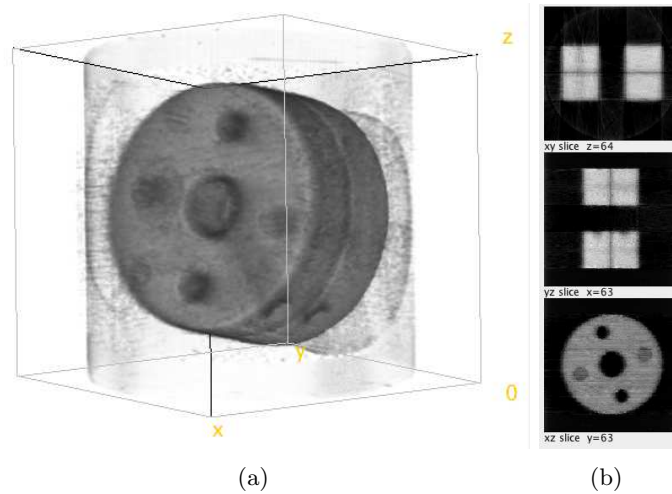


Figure 4.9: 3D representation (a) and sectional views (b) of OS-SART reconstruction (created with ImageJ Volume Viewer).

4.2 Different number of particles and projections

To be more time-efficient on the simulation and/or the reconstruction side or to receive a higher image quality on the other hand, some input parameters of the reconstruction were changed, namely the number of initial protons and the number of projections used for the reconstruction. The OS-SART was then applied to the projections with 5 iterations and a blocksize of 10.

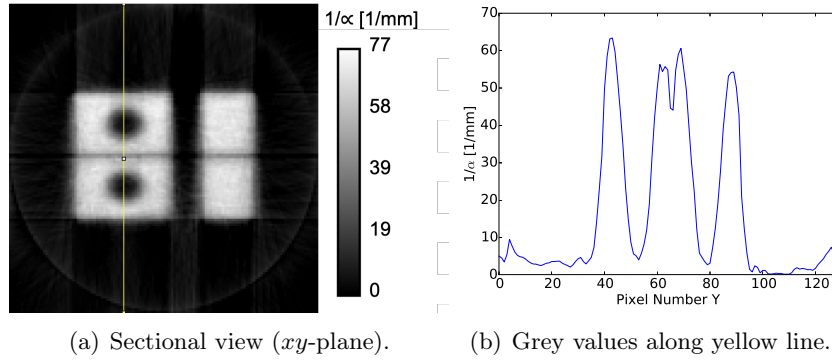


Figure 4.10: 90 projections using 10^6 primary protons \rightarrow OS-SART, slice $z = 36$.

Whereas for the reconstructions in the previous Section 5×10^5 initial protons were used, now the number was increased to 10^6 . Again, 90 projections were used for the reconstruction - because of that, only simulation but not reconstruction time was changed. The resulting cross-sections of the object can be seen in Figure 4.10 and Figure 4.11.

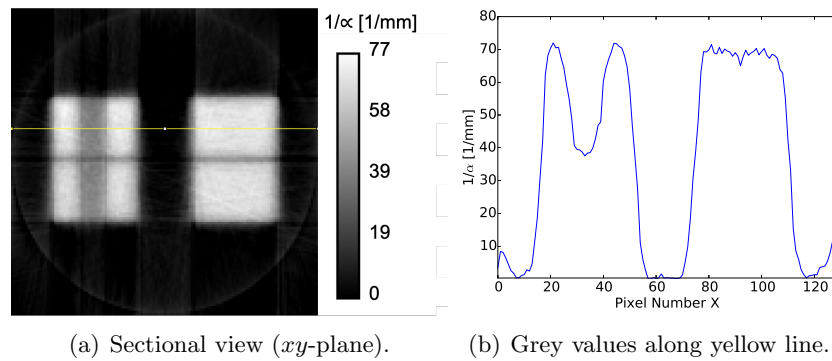


Figure 4.11: 90 projections using 10^6 primary protons \rightarrow OS-SART, slice $z = 60$.

Compared to Figure 4.7 and Figure 4.8, no clear improvement of the curves for the grey values can be seen. Again, substructures of the object, such as air holes and plastic filling can be seen very well. However, neither the scale of the grey values nor the edge structures were clearly changed.

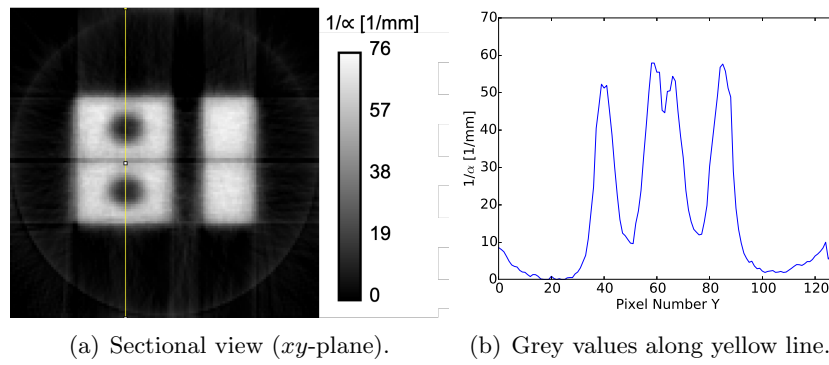


Figure 4.12: 60 projections using 10^6 primary protons \rightarrow OS-SART algorithm, slice $z = 36$.

This indicates that the statistics for the projections (average of all residual energies of protons hitting one pixel) are already sufficient and therefore the number of initial particles does not have to be increased (which would result in twice the time for performing the simulations).

As a second step, the reconstruction was performed using only 60 projections using 10^6 (Figure 4.12 and Figure 4.13) and 5×10^5 (Figure 4.14 and Figure 4.15) primary protons. In both cases, the computing time for the reconstruction is cut by one third; the simulation time in the first case is twice the simulation time than for the second case.

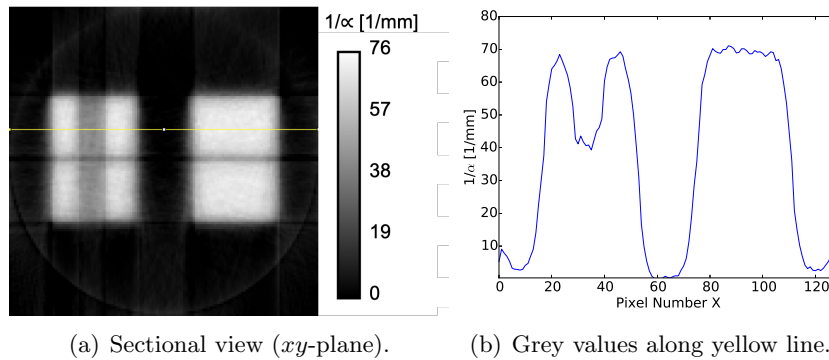


Figure 4.13: 60 projections using 10^6 primary protons \rightarrow OS-SART algorithm, slice $z = 60$.

As it could already be seen for the reconstructions with 90 projections, there is no significant difference in the reconstructed images if 10^6 or 5×10^5 primary protons are used, since the curves for the grey values do not differ remarkably in shape and height. This confirms the assumption that the statistics are already sufficient with the smaller number of primary ions.

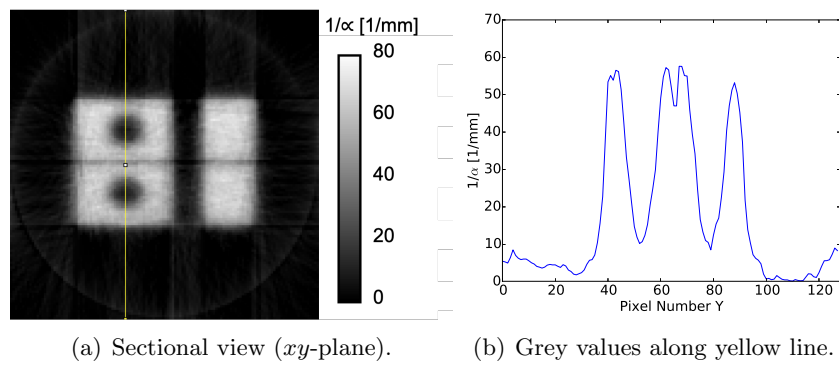


Figure 4.14: 60 projections using 5×10^5 primary protons \rightarrow OS-SART algorithm, slice $z = 36$.

Again, a smooth curve showing the object's substructures is obtained in the reconstruction. However, some small difference to the reconstruction of 90 projections can be seen, especially regarding the grey values of slice $z = 36$ (Figure 4.12 and Figure 4.14). When it comes to really small structures, the grey values for aluminium in Figure 4.10 exceed a value of 60 for 90 projections. The air holes result in a grey value between 5 and 10. In contrast to that, the grey values for aluminium along the yellow line in Figure 4.12 (60 projections) are a little bit smaller and the grey value for air holes lies between 10 and 20. This effect can only be seen for some small structures, however, it was the reason why further reconstructions were still performed with 90 projections.

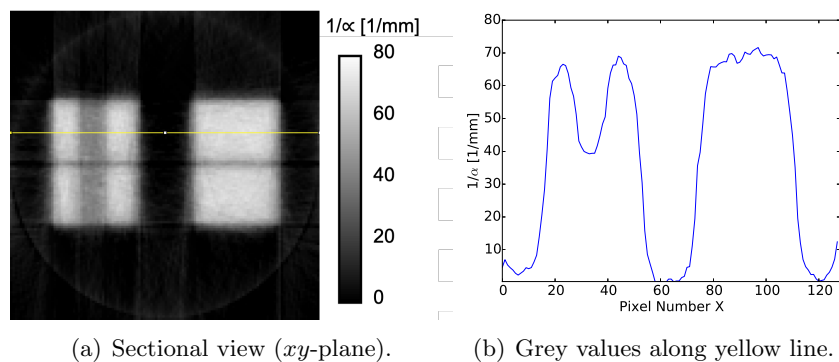


Figure 4.15: 60 projections using 5×10^5 primary protons \rightarrow OS-SART algorithm, slice $z = 60$.

4.3 Determination of the stopping power

Section 4.1 and Section 4.2 already showed that the OS-SART with 5 iterations and a blocksize of 10 can - in combination with 90 projections generated from $5 \cdot 10^5$ primary protons - be used to successfully reconstruct the irradiated object and calculating

the reciprocal of α in the right scale. This principle was now applied to really simple cylindrical phantoms that will in the following replace the Pololu mounting hubs. From the results, the material parameter and in the following the approximate stopping power of the material (according to Equation (2.6)) was calculated. In Section 4.3.1 only phantoms made of one material are analyzed. In Section 4.3.2, cylindrical phantoms of different materials are put in succession and irradiated together. Imaging parameters such as detector size or the image size remained the same as before.

4.3.1 Phantoms made of one material

As a first step, three cylindrical phantoms of water, plastic (Nylon 66) and aluminium with a radius of 10 mm and a length of 10 mm were created in Geant4. Each of them was irradiated in the simulation with an initial proton energy of 100 MeV.

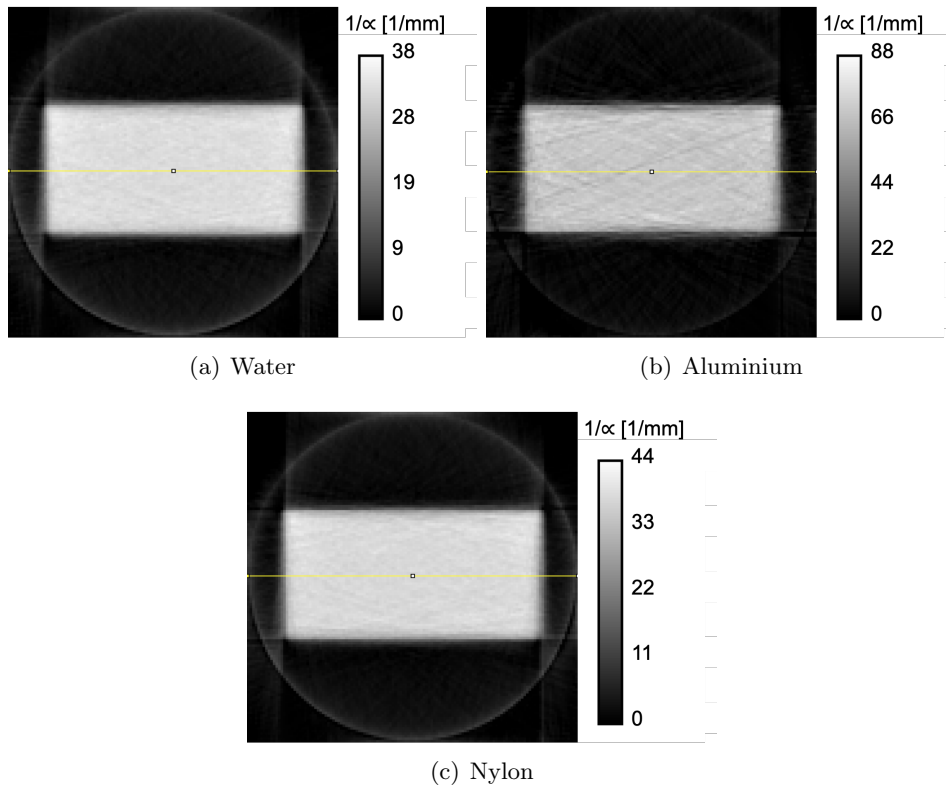


Figure 4.16: Phantoms 1-3 - Cylindrical phantoms made of one material (Slice $z = 64$).

The reconstructed images are represented by their central intensity profile ($z = 64$), which can be seen in Figure 4.16. It can be seen that - similar to the mounting hubs before - the cylinders were lying in beam direction (y -axis in ImageJ) which results in a rectangle in the xy -view. Although these intensity profiles look very much alike for all of the phantoms, a difference can be seen if the range of the colour bars in Figure

4.16 and - in more detail - if the grey values along the yellow line in the middle of the object are analyzed (see Figure 4.17). Even for water and Nylon 66, which have a similar stopping power, a slight difference in the grey values can be seen. While for water, $1/\alpha$ fluctuates around a value slightly below 35, it fluctuates around a value slightly above 35 for nylon. This then again results in a higher stopping power. The exact results of the stopping power calculation - resulting from an average value of $1/\alpha$ - can be found in Table 2 and Table 3.

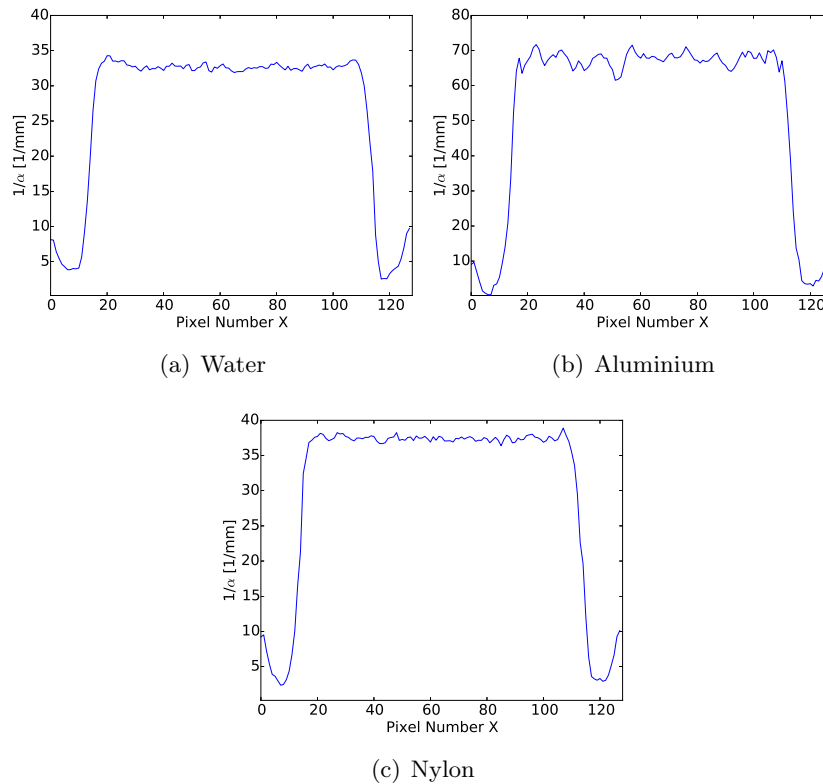


Figure 4.17: Grey values along $y = 64$ and $z = 64$.

To investigate the influence of the initial proton energy on the resulting stopping power calculation, a cylindrical phantom with a length and a radius of 10 mm was created and irradiated at different energies (from 75 MeV to 175 MeV in 25 MeV steps). This time, the phantom was made of tissue-equivalent plastic (which is used for biological phantoms). The resulting stopping power can be found in Figure 4.18 in comparison to the literature values at the respective energy or in numbers in Table 2 and Table 3. As it was expected, the difference to the literature value [60] decreases with increasing energy.

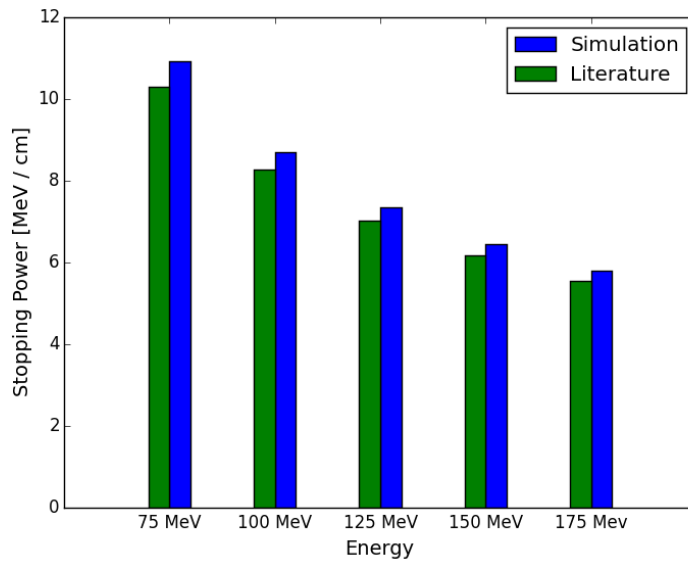


Figure 4.18: Phantom 4 - Tissue material ($l = 10$ mm, $r = 10$ mm) irradiated at different energies.

Next, other cylindrical phantoms of tissue-equivalent plastic were generated in Geant4 to see the influence of the object size in the calculation of the stopping power. Due to the smaller size of the objects they were irradiated with 75 MeV protons. The exact sizes of the object can be seen in Figure 4.19, where again the sectional views of $z = 64$ are depicted. The results for the stopping power calculation from the grey values can again be found in Table 2 and Table 3. As it could already be assumed, the calculation becomes more accurate with a smaller object size. The reason therefore is that the stopping power changes over the proton path through an object (since the proton energy changes). If a thinner object is irradiated, the stopping power changes less than over a thicker object resulting in a more accurate calculation.

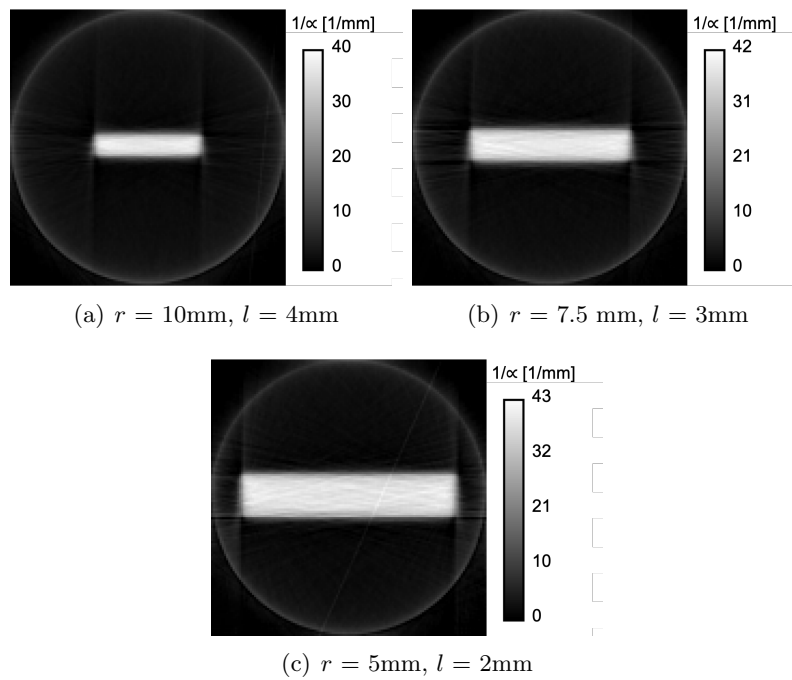


Figure 4.19: Phantoms 5-7 - Tissue material phantoms with different sizes.

For better comparison, Table 2 shows the dimensions and materials of all the one-material phantoms irradiated. Table 3 shows the value of $1/\alpha$ that was obtained through the reconstruction and the resulting stopping power compared to the literature value (taken from [60]).

Phantom Nr.	Material	Radius [mm]	Length [mm]
1	Water	10	10
2	Aluminium	10	10
3	Nylon	10	10
4	Tissue	10	10
5	Tissue	10	4
6	Tissue	7.5	3
7	Tissue	5	2

Table 2: Parameters of phantoms made of one material

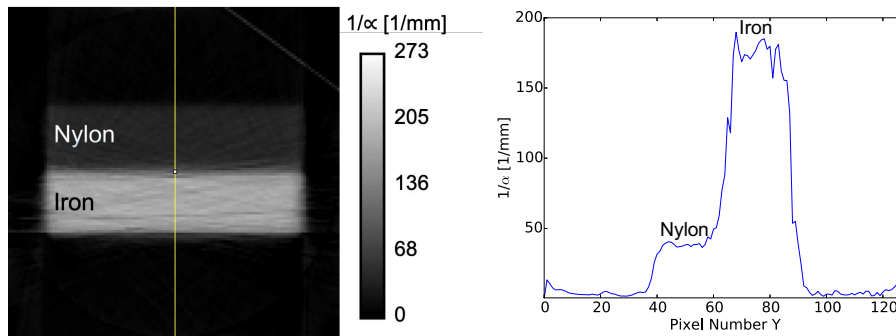
It can be seen that the calculated values show a deviation from the literature value that is less than 7 %. The largest deviations could be found for materials with a high stopping power or at low energies. Furthermore, the dimensions of the phantom have an influence on the result - it could be seen that generally, the calculated stopping power of a smaller phantom corresponds better with the literature value as it was already explained with Figure 4.19.

Phantom Nr.	Initial ion energy [MeV]	$1/\alpha$ [1/mm]	dE/dx [MeV/cm]	dE/dx [MeV/cm] Literature	Deviation from Literature [%]
1	100	32.74	7.67	7.29	3.39
2	100	67.62	15.84	15.32	5.21
3	100	37.45	8.77	8.37	4.78
4	75	38.13	10.92	10.29	6.12
4	100	37.18	8.71	8.27	5.32
4	125	36.76	7.36	7.02	4.84
4	150	36.55	6.44	6.17	4.38
4	175	36.64	5.80	5.56	4.32
5	75	38.41	11.00	10.29	6.90
6	75	37.98	10.88	10.29	5.73
7	75	35.98	10.31	10.29	0.19

Table 3: Results of stopping power calculations for phantoms made of one material

4.3.2 Phantoms made of multiple materials

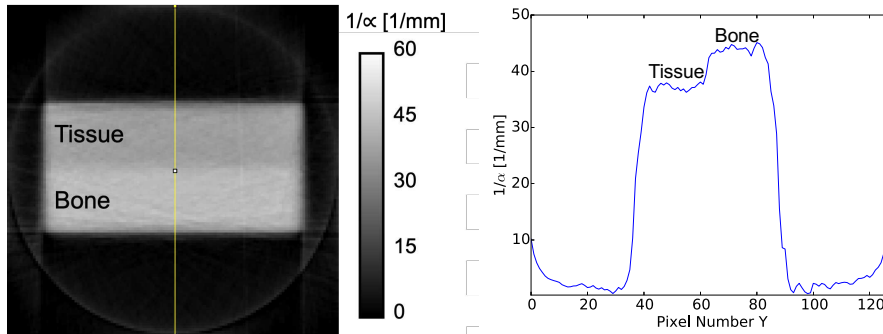
Since it could be seen that an approximate calculation of the stopping power is possible with phantoms made of one material in the last Section, the setup was extended to phantoms made of two or three materials. Again, cylindrical phantoms with a radius of 10 mm were created, each slice had a length of 5 mm. Again the grey values ($1/\alpha$) were taken from the reconstructed images and an average was used to further calculate the stopping power.



(a) Sectional view (xy -plane, slice $z = 64$) - material labels have been added after the reconstruction. (b) Grey values along yellow line.

Figure 4.20: Phantom 8 - Iron and nylon.

At first, a phantom of iron and nylon was created in Geant4 (irradiation with 200 MeV protons) since the stopping power of these materials is very different. In contrast, a phantom made of bone- and tissue-equivalent plastic was created (irradiation with 100 MeV protons) because these materials have a very similar stopping power. The results of the reconstruction can be seen in Figure 4.20 and Figure 4.21. In the sectional view for the iron and nylon phantom (Figure 4.20 (a)), the nylon can hardly be identified since the stopping power of iron is much higher than the one of nylon. The result is a significantly higher grey value for iron compared to nylon. However, regarding Figure 4.20 (b), it can be seen that the nylon slice of the phantom can nevertheless be identified and distinguished from the background, since the grey value for nylon is different than the one for air.

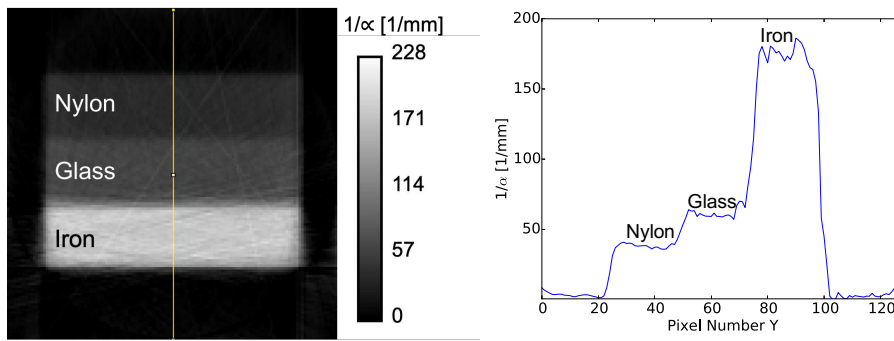


(a) Sectional view (xy -plane, slice $z = 64$) - material labels have been added after the reconstruction. (b) Grey values along yellow line.

Figure 4.21: Phantom 9 - Bone- and tissue equivalent plastic.

Regarding the bone and tissue phantom, a small difference in the grey values can already be seen in the sectional view (Figure 4.21 (a)). It can be illustrated more clearly by considering the grey values in Figure 4.21 (b) where an increase of the grey value can be seen at the transition from tissue (top in Figure 4.21 (a)) to bone (bottom in Figure 4.21 (a)).

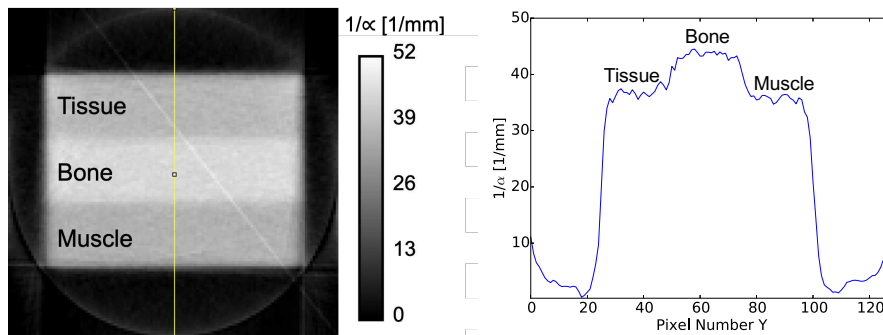
The stopping power that was calculated for these phantoms can be found in Table 4 and Table 5.



(a) Sectional view (xy -plane, slice $z = 64$) - material labels have been added after the reconstruction. (b) Grey values along yellow line.

Figure 4.22: Phantom 10 - Iron, glass and nylon.

As a next step, phantoms made of three materials were generated and irradiated with 220 MeV protons in Geant4. Again, one phantom was made of three very different materials, namely iron, glass and nylon. The reconstruction of the respective projections can be found in Figure 4.22, where (a) again displays the sectional view of the xy -plane in the center of the phantom ($z = 64$) and (b) displays the grey values along the yellow line in y -direction.



(a) Sectional view (xy -plane, slice $z = 64$) - material labels have been added after the reconstruction. (b) Grey values along yellow line.

Figure 4.23: Phantom 11 - Tissue, bone and muscle equivalent plastic.

Like before, projections of a phantom made of three very similar materials (tissue, bone and muscle equivalent plastic) were generated too (irradiation with 120 MeV protons). The reconstruction can be seen in Figure 4.23. It can be seen that the grey value for bone is again higher than the one for muscle and tissue. However, a difference between tissue and muscle can hardly be found in the cross-sectional view and even in the curve of the grey values. Nevertheless, the calculation of the average α showed a small difference

between the materials which can therefore be distinguished in the image.

The exact results of the stopping power calculations of multiple-material phantoms can be found in Table 4 (phantom dimensions and materials) and Table 5 (α and stopping power at respective energy).

Phantom Nr.	Material	Radius [mm]	Length per material slice [mm]
8	Iron-Nylon	10	5
9	Tissue-Bone	10	5
10	Iron-Glass-Nylon	10	5
11	Tissue-Bone-Muscle	10	5

Table 4: Parameters of phantoms made of several materials

It can be seen that the deviation from the literature values (taken from [60]) is smaller than 10 % for each phantom material. The largest deviations can be seen for phantoms made of very different materials (regarding their stopping power). In that case, the calculation for the material with the smaller stopping power (in this case nylon and glass in comparison to iron) shows a larger deviation from the literature value. The effect that the calculated stopping power is closer to the literature value for the materials with a higher stopping power in a mixed phantom can also be seen for the tissue/bone and tissue/bone/muscle phantom, although the effect is smaller for these phantom compositions.

Phantom Nr. & Slice material	Initial ion energy [MeV]	$1/\alpha$ [1/mm]	dE/dx [MeV/cm]	dE/dx [MeV/cm] Literature	Deviation from Literature [%]
8 (Iron)	200	177.82	25.63	24.83	3.22
8 (Nylon)	200	39.21	5.65	5.15	9.71
9 (Tissue)	100	37.43	8.77	8.27	6.05
9 (Bone)	100	44.23	10.36	9.87	4.96
10 (Iron)	220	179.21	24.17	23.40	3.29
10 (Glass)	220	62.11	8.38	7.87	6.48
10 (Nylon)	220	38.26	5.16	4.85	6.39
11 (Tissue)	120	37.21	7.67	7.23	6.09
11 (Bone)	120	43.94	9.06	8.63	4.98
11 (Muscle)	120	36.00	7.42	7.00	6.00

Table 5: Results of stopping power calculations for phantoms made of several materials

4.4 Image reconstruction with carbon ions

Although the focus of this thesis is on proton CT reconstruction, one reconstruction of a carbon ion CT of the Pololu mounting hubs has been performed as comparison.

Due to their high mass, the straight line approach is more accurate for carbon ions. The projections have again been defined according to 3.14, except that the exponent had to be changed to 1.5 for this ion type (see [25]). The initial ion energy was set to 150 MeV/u.

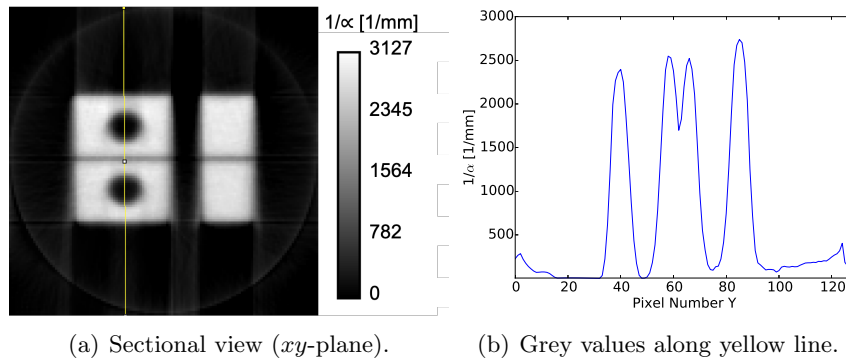


Figure 4.24: Reconstruction with carbon ions: OS-SART, slice $z = 36$.

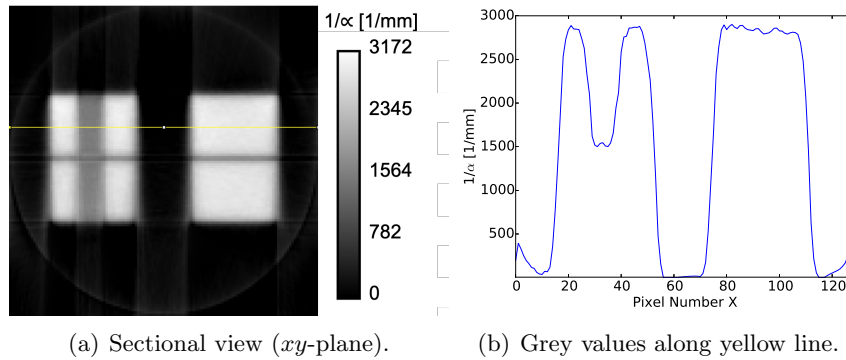


Figure 4.25: Reconstruction with carbon ions: OS-SART, slice $z = 60$.

The sectional views and curves of grey values (Figure 4.24 and Figure 4.25) show very well the substructures of the mounting hub as well as the different materials. Since the term $1/\alpha$ is higher for carbon ions than for protons, also the image contrast is enhanced. Regarding the 3D view (Figure 4.26) of the mounting hubs, it can also be seen that the side effect that image values are increased at the edges has a smaller contribution than for protons.

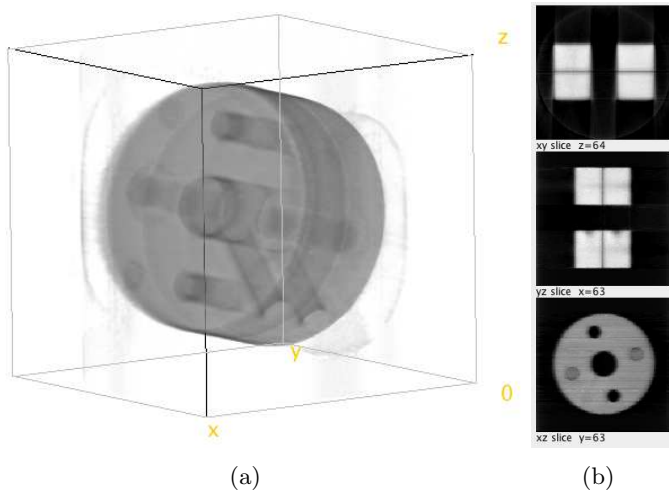


Figure 4.26: 3D representation (a) and sectional views (b) of OS-SART reconstruction of carbon ion CT (created with ImageJ Volume Viewer).



Die approbierte gedruckte Originalversion dieser Diplomarbeit ist an der TU Wien Bibliothek verfügbar.
The approved original version of this thesis is available in print at TU Wien Bibliothek.

5 Conclusion and Outlook

In the scope of this thesis, a simple ion CT setup was simulated using Geant4 and the projection data were reconstructed using TIGRE. It could be demonstrated that with these data, reproducible and usable results can be generated.

As a first step, the projections were created using a simple straight line approach that was applied to the simulation data. The simulated projection data of the initial phantom (Pololu mounting hub) were then reconstructed with different algorithms that were already implemented in TIGRE. The results were stored in a DICOM file and displayed in ImageJ.

Compared to SART and FDK algorithm, it could be seen that the OS-SART generates a very good image quality using only a few iterations (taking about 20 seconds per reconstruction with 90 projections). For that reason, this algorithm was used for further reconstructions. As a next step, the number of initial particles and the number of projections used were varied. It could be demonstrated that using 500 thousand primary protons are enough to generate a usable image. Small structures of the reconstructed object could be seen better with a larger number of projections (comparison of 90 and 60 projections was given), which is why the number of projections was not cut for further reconstructions.

With this preparatory work, the initial phantom was finally changed to simple cylindrical phantoms of one or more materials. Using the Bragg-Kleeman law, the stopping power of the materials has been determined from the reconstructed images. Although this approach is only based on a simple straight line approximation of the ion path, it could be seen that the deviation from the literature values is smaller than 10 % and decreases with a higher ion energy.

The results and findings of this thesis will be used for the ion CT setup at MedAustron which is currently being improved. When the new setup is completely installed, the simulation will have to be adapted accordingly. This also includes a more realistic representation of the energy measurement in the simulations. Within this thesis, it was regarded as ideal, since there hasn't been an energy measurement device installed at the MedAustron setup yet.

Although the straight line approach that was used within this thesis already offers good results for image quality and approximate stopping power, it will have to be changed to a more realistic ion path for even more accurate results. Therefore the MLP or a cubic spline approach will have to be implemented to the reconstruction framework. This can again be the TIGRE framework (especially since there is already a Python implementation of the framework) or any other reconstruction framework that allows the implementation of own algorithms. This subject also includes the determination of the convex hull of an object, which was not covered in the reconstruction process in this thesis.

As it has already been stated, the reconstruction using the straight line approach generates a good initial assumption for a material stopping power and could therefore be used as initial image for iterative reconstruction algorithms in the future.

Another open issue is the image reconstruction using other ions than protons, such as

helium or carbon ions (only one reconstruction using carbon ions was performed in the scope of this thesis, see Section 4.4). Furthermore, in the long run, the small phantoms that have already and will be irradiated in the real setup will have to be changed to human-like phantoms or biological material. This has then again to be implemented in the Geant4 simulations (e.g. using voxelized phantoms as for example used in [61]).

To conclude, it can be said that the image reconstruction of an ion CT can be successfully performed using TIGRE if the ion path is approximated with a straight line. Although there are some improvements to be implemented to the reconstruction process, the quality of the reconstructed images allow already to use them as comparison for real data or as an initial image for an iterative reconstruction algorithm.



Die approbierte gedruckte Originalversion dieser Diplomarbeit ist an der TU Wien Bibliothek verfügbar.
The approved original version of this thesis is available in print at TU Wien Bibliothek.

6 Acknowledgements

First of all, I would like to thank Dr. Thomas Bergauer, Dr. Albert Hirtl and Prof. Jochen Schieck for making this thesis possible with their expertise and support. Furthermore, I would like to thank DI Alexander Burkner and DI Felix Ulrich-Pur from TU Wien and HEPHY, who were always open for a discussion and helped me to get started with the Geant4 software framework.

I would like to thank the members of the MedUni Center for Medical Physics and Biomedical Engineering, Dr. Wolfgang Birkfellner, Dr. Michael Figl and Sepideh Hatamikia, MSc. for introducing me to the TIGRE software framework and supporting me with my questions.

Furthermore, I would like to thank all other people who supported me on a personal level, encouraged me and kept me motivated during my studies. I would like to thank my parents, Helmut and Sabina, for always listening to my concerns and providing me the best possible environment so that I could stay focused on my goals. A huge thank you to my sister, Elisabeth, for our lovely lunches and our deep conversations. I would like to thank my aunt, Brigitte, for her exceptional interest and her thoughtful questions not only regarding my field of study but also all other aspects of my life. Thank you, Florian, for supporting me, listening to my problems throughout my studies and for being the person who could always cheer me up. Finally, I would like to thank my friends Claudia, Felicia, Lisa, Marlene and Michael for letting me talk about physics - but also for not letting me forget that there are other important aspects in life.



Die approbierte gedruckte Originalversion dieser Diplomarbeit ist an der TU Wien Bibliothek verfügbar.
The approved original version of this thesis is available in print at TU Wien Bibliothek.

Appendix

Projection data

Figure 6.1 to Figure 6.3 show projections at 0° , 45° and 90° using different values for $t_{x,y}$ as it was described in Section 3.3.1 and Section 3.3.3.

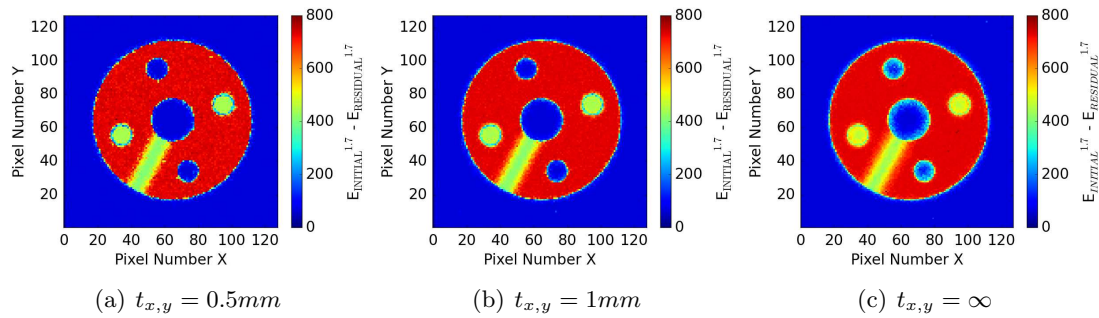


Figure 6.1: Projections with 10^6 protons at 100 MeV at 0° using different values for $t_{x,y}$ (projections according to Equation (3.14)).

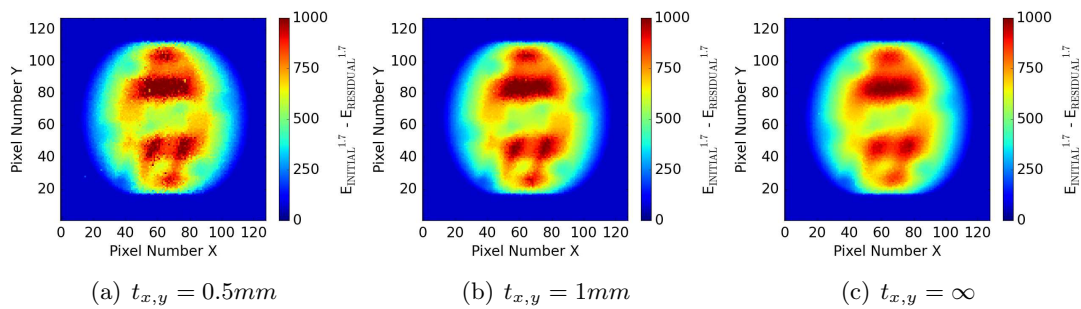


Figure 6.2: Projections with 10^6 protons at 100 MeV at 45° using different values for $t_{x,y}$ (projections according to Equation (3.14)).

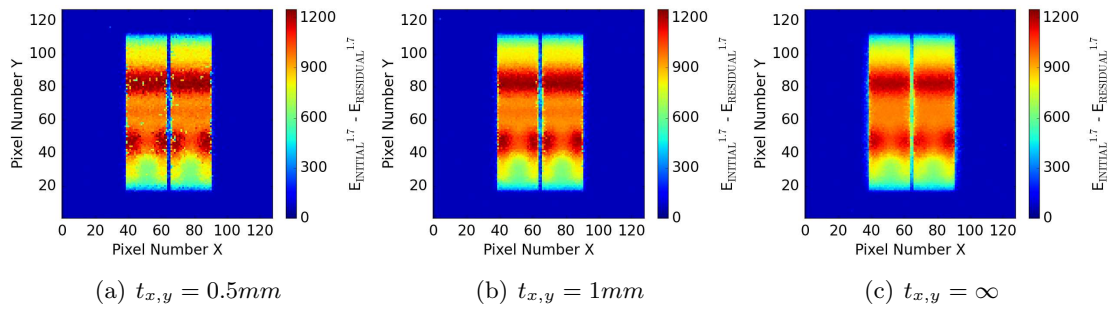


Figure 6.3: Projections with 10^6 protons at 100 MeV at 90° using different values for $t_{x,y}$ (projections according to Equation (3.14)).

Figure 6.4 to Figure 6.6 show projections at 0° , 45° and 90° using different values for the initial particle energy as it was already shown in Section 3.3.3. The projection values are defined by Equation (3.14).

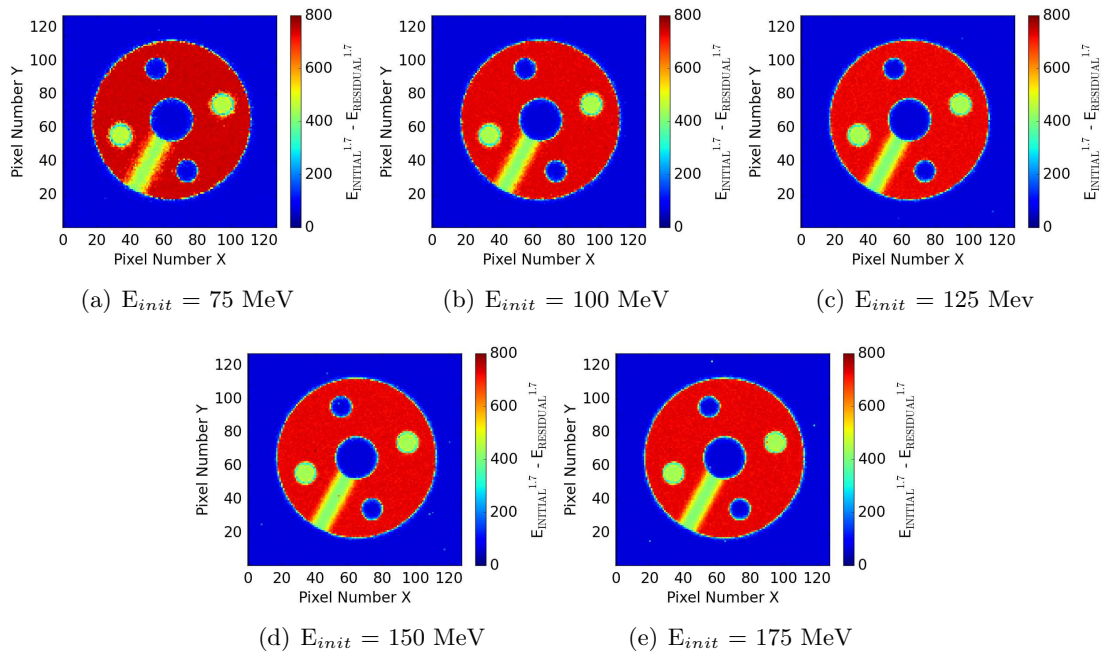


Figure 6.4: Projections with 10^6 protons at 0° ($t_{x,y} = 1$ mm, projections according to Equation (3.14)).

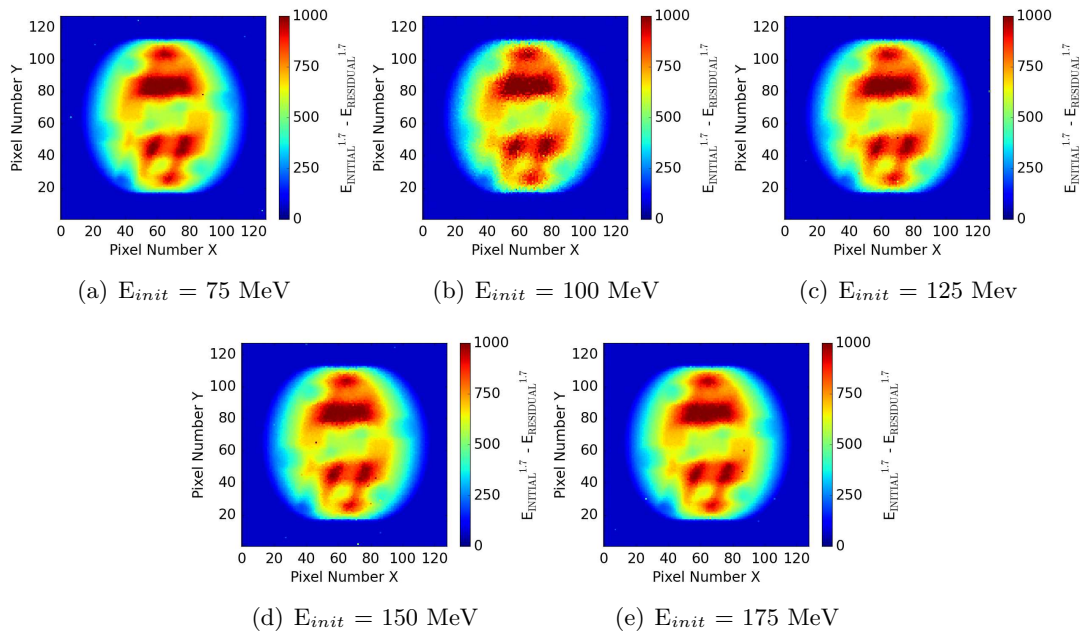


Figure 6.5: Projections with 10^6 protons at 45° ($t_{x,y} = 1$ mm, projections according to Equation (3.14)).

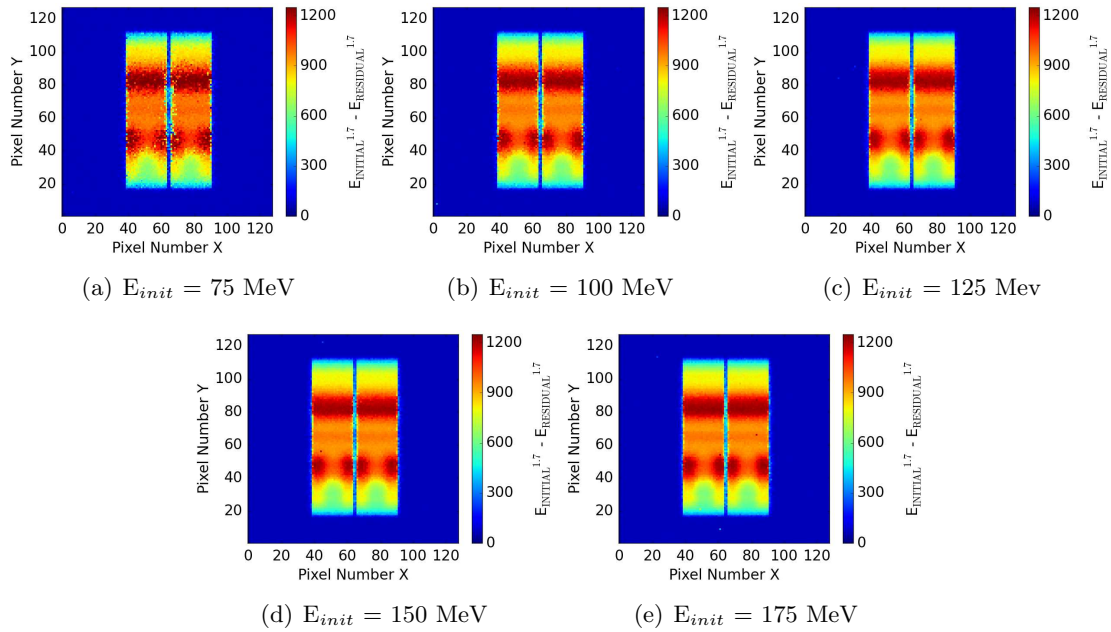


Figure 6.6: Projections with 10^6 protons at 90° ($t_{x,y} = 1$ mm, projections according to Equation (3.14)).

Figure 6.7 to Figure 6.9 show projections at 0° , 45° and 90° using different values for the initial particle energy and using the relative particle energy loss for the definition of the projection value as it was already shown in Section 3.3.3.

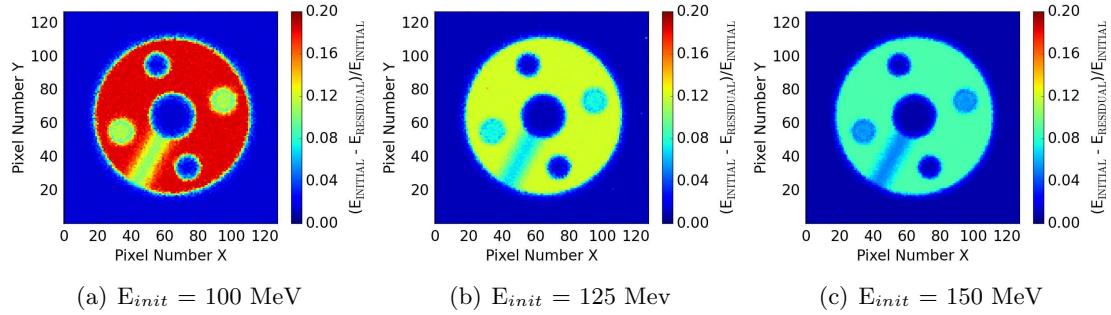


Figure 6.7: Projections with 10^6 protons at 0° ($t_{x,y} = 1$ mm, projections according to Equation (3.15)).

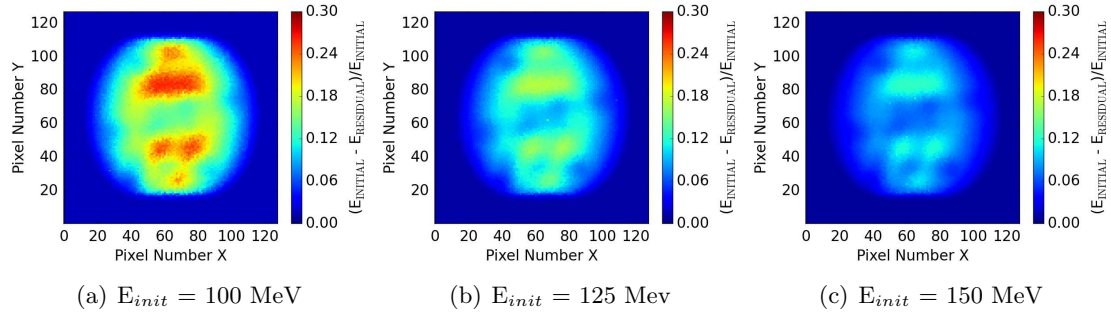


Figure 6.8: Projections with 10^6 protons at 45° ($t_{x,y} = 1$ mm, projections according to Equation (3.15)).

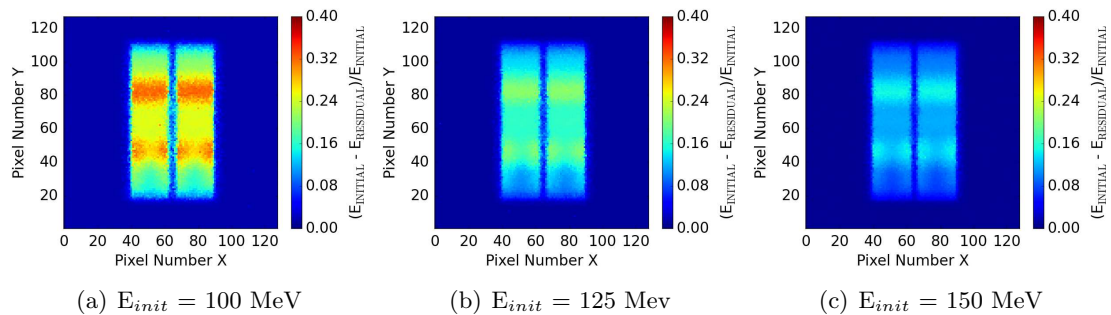


Figure 6.9: Projections with 10^6 protons at 90° ($t_{x,y} = 1$ mm, projections according to Equation (3.15)).

Variation of SART iterations

Figure 6.10 and Figure 6.11 show sectional views of an image of the Pololu mounting hubs that were created by reconstruction with SART in 20 iterations. Although the object can still be recognized in the xy -planes, the curves for the grey values are a lot more uneven than the ones shown in Section 4.1 (Figure 4.4 and Figure 4.5), which makes it difficult to determine the borders of the object and its substructures. Furthermore the algorithm needed about 35s per additional iteration, which is why this reconstruction was not used any further in this thesis.

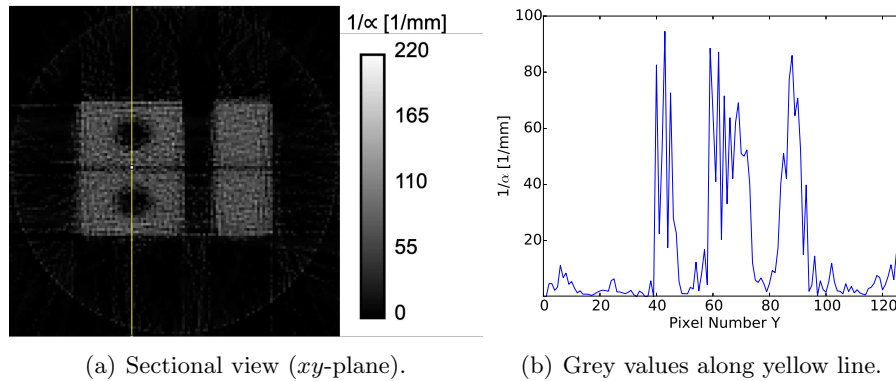


Figure 6.10: SART with 20 iterations, slice $z = 36$.

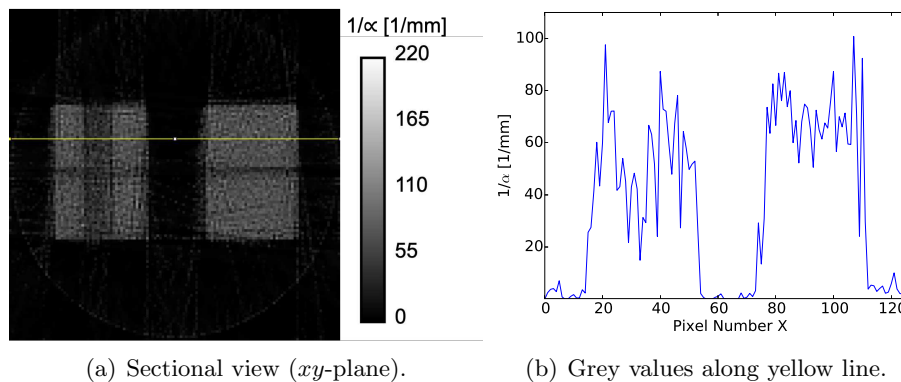


Figure 6.11: SART with 20 iterations, slice $z = 60$.

Variation of OS-SART iterations and blocksize

The OS-SART not only offers the possibility to change the number of iterations but also the blocksize used. Therefore three additional parameter compositions were made: 20 iterations with blocksize 10, 20 iterations with blocksize 5 and 5 iterations with blocksize 5.

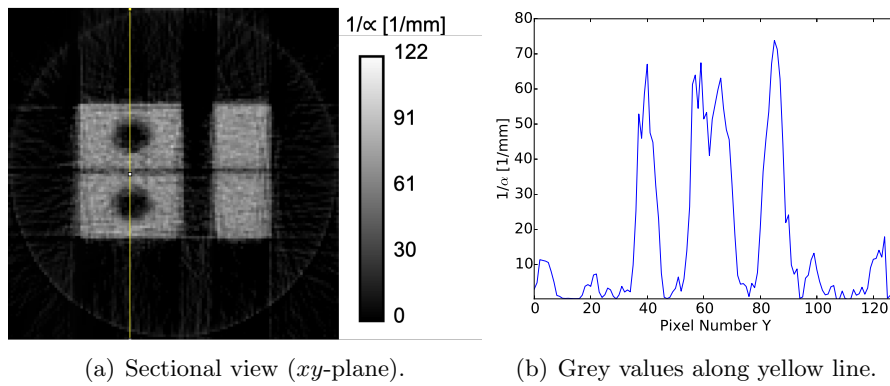


Figure 6.12: OS-SART with 20 iterations and blocksize 10, slice $z = 36$.

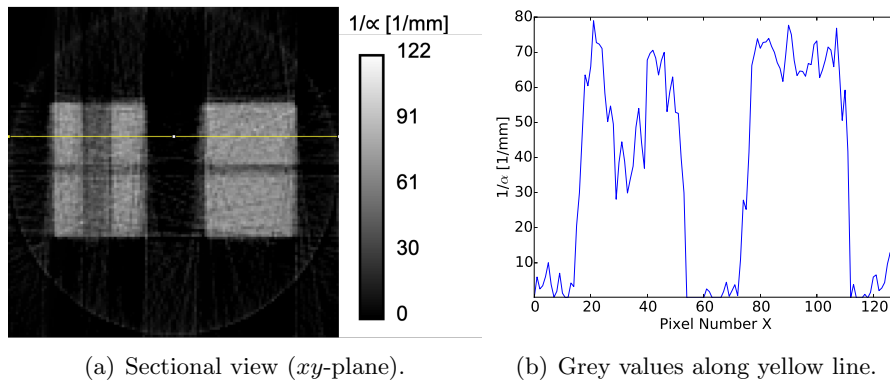


Figure 6.13: OS-SART with 20 iterations and blocksize 10, slice $z = 60$.

Figure 6.12 and Figure 6.12) show the respective sectional views for 20 iterations and a blocksize of 10, which means that in comparison to Figure 4.7 and 4.7 in Section 4.1, only the number of iterations has been changed. As it could be already seen for the SART algorithm, this step results in more uneven curves for the grey values and of course a longer computation time for the reconstruction which is again why this configuration was not used any further.

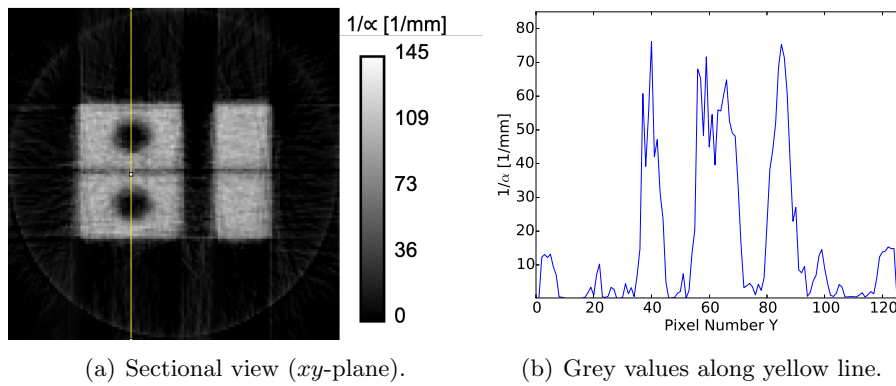


Figure 6.14: OS-SART with 20 iterations and blocksize 5, slice $z = 36$.

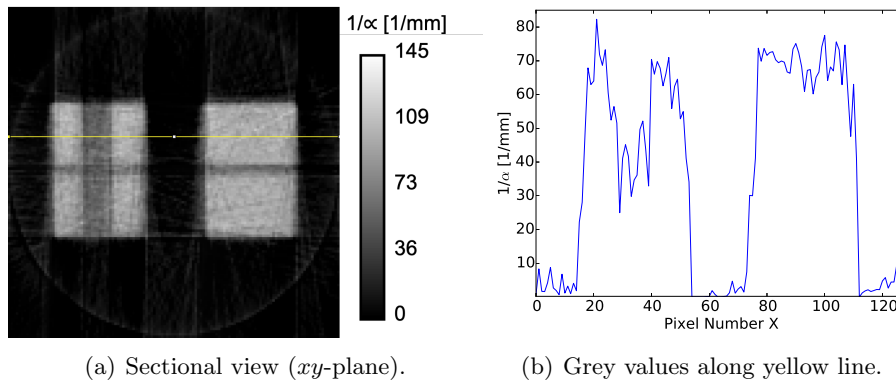


Figure 6.15: OS-SART with 20 iterations and blocksize 5, slice $z = 60$.

If, as a next step, the block size is reduced to 5, the result can be seen in Figure 6.12 and Figure 6.12). It looks similar to the result before but with the curves of the grey values being even a little more uneven. The decrease of the blocksize again increases the reconstruction time. A blocksize equal to 1 would result in the same outcome as SART with the same number of iterations.

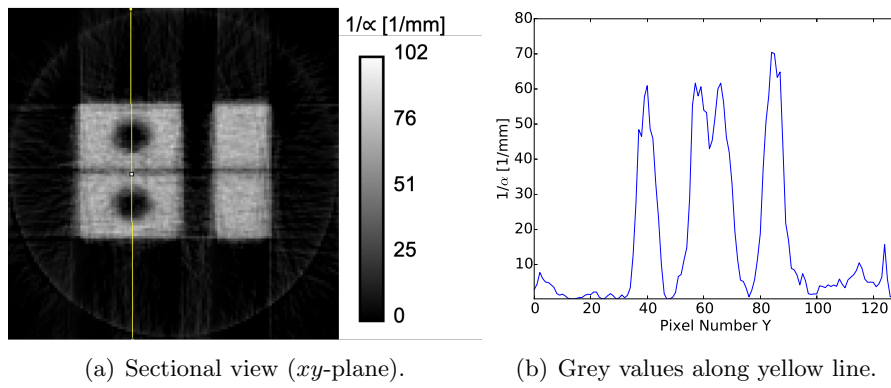


Figure 6.16: OS-SART with 20 iterations and blocksize 5, slice $z = 36$.

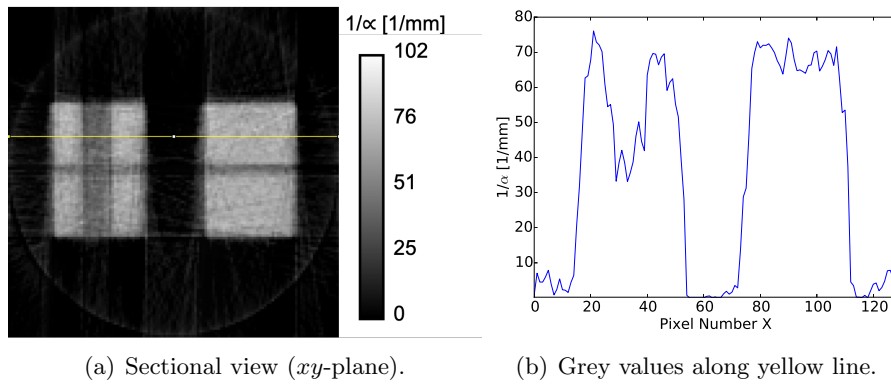


Figure 6.17: OS-SART with 20 iterations and blocksize 5, slice $z = 60$.

The last parameter configuration was to only use 5 iterations but again with the smaller blocksize of 5. As expected, the resulting curves for the grey values look smoother than with 20 iterations but still more uneven than the result shown in Section 4.1, since these parameters generate a result which is closer to the SART result.

List of Figures

1.1	Dose distribution of proton radiotherapy (left) compared to X-ray radiotherapy (right) of a brain tumour [4].	5
1.2	Hadron therapy facilities in Europe in 2016 [5].	6
2.1	Interaction mechanisms of protons and matter [7]: (a) inelastic Coulomb interaction, (b) elastic Coulomb scattering with nucleus, (c) non-elastic nuclear reactions.	9
2.2	Parameters for the calculation of the Bethe-Formula [8].	10
2.3	Bragg peak shape for protons [7].	14
2.4	SOBP [7].	16
2.5	Demonstration of water equivalent thickness [7].	17
2.6	Percentage error of the mass stopping power ratio of 200 MeV and energy E for air and bone compared to that of water [21].	18
2.7	Schematic overview of ion imaging setup (PSD - Position Sensitive Detector, RERD - Residual Energy Resolving Detector) [17].	19
2.8	Overview on some possible path estimates (red) compared to the real ion path (black) from [14] (adapted): (a) SL using only one hit position of a rear detector, (b) SL using hit position from a front and a rear detector, (c) several SLs using hit positions and particle directions in front of and behind the phantom and (d) a most likely path approach using positions and directions before and after the phantom.	22
2.9	For the definition of the MLP: Entry point A and exit point D of the proton are known. The probability of the proton passing the intermediate point C is to be estimated [21].	23
2.10	Comparison of different path estimates [29] (adapted): RMS deviation from real path to MLP - most likely path, CSP - cubic spline path and SLP - straight line path.	24
2.11	An object is irradiated at an angle φ relative to the x -axis and an orthogonal distance r to the origin [30].	25
2.12	Radon transform (right) of a disc (left). The abscissa represents the different radii (from 1 to 128), the ordinate represents the different values of φ (from 0 to 179 degrees) [30].	25
2.13	Projection slice theorem for $\varphi = 0$ [30].	26
3.1	MedAustron facility [37].	31
3.2	Experimental setup at MedAustron [39].	31
3.3	Geant4 structure [42].	33
3.4	Structure of TIGRE [51].	37
3.5	ImageJ Volume Viewer.	39
3.6	Overview of image reconstruction process.	40
3.7	Initial phantom in the Geant4 simulation.	41
3.8	Experimental setup in Geant4.	43
3.9	Projections with 10^6 protons at 100 MeV at 0° using different values for $t_{x,y}$ (projections according to Equation (3.14)).	45

3.10	Projections with 10^6 protons at different energies at 0° ($t_{x,y} = 1$ mm, projections according to Equation (3.14)).	46
3.11	Projections with 10^6 protons at different energies at 0° ($t_{x,y} = 1$ mm, projections according to Equation (3.15)).	47
3.12	Geometry definition in TIGRE.	48
4.1	FDK algorithm, slice $z = 36$	53
4.2	FDK algorithm, slice $z = 60$	53
4.3	3D representation (a) and sectional views (b) of FDK reconstruction (created with ImageJ Volume Viewer).	54
4.4	SART, slice $z = 36$	55
4.5	SART, slice $z = 60$	55
4.6	3D representation (a) and sectional views (b) of SART reconstruction (created with ImageJ Volume Viewer).	56
4.7	OS-SART, slice $z = 36$	56
4.8	OS-SART, slice $z = 60$	57
4.9	3D representation (a) and sectional views (b) of OS-SART reconstruction (created with ImageJ Volume Viewer).	57
4.10	90 projections using 10^6 primary protons \rightarrow OS-SART, slice $z = 36$	58
4.11	90 projections using 10^6 primary protons \rightarrow OS-SART, slice $z = 60$	58
4.12	60 projections using 10^6 primary protons \rightarrow OS-SART algorithm, slice $z = 36$	59
4.13	60 projections using 10^6 primary protons \rightarrow OS-SART algorithm, slice $z = 60$	59
4.14	60 projections using 5×10^5 primary protons \rightarrow OS-SART algorithm, slice $z = 36$	60
4.15	60 projections using 5×10^5 primary protons \rightarrow OS-SART algorithm, slice $z = 60$	60
4.16	Phantoms 1-3 - Cylindrical phantoms made of one material (Slice $z = 64$).	61
4.17	Grey values along $y = 64$ and $z = 64$	62
4.18	Phantom 4 - Tissue material ($l = 10$ mm, $r = 10$ mm) irradiated at different energies.	63
4.19	Phantoms 5-7 - Tissue material phantoms with different sizes.	64
4.20	Phantom 8 - Iron and nylon.	65
4.21	Phantom 9 - Bone- and tissue equivalent plastic.	66
4.22	Phantom 10 - Iron, glass and nylon.	67
4.23	Phantom 11 - Tissue, bone and muscle equivalent plastic.	67
4.24	Reconstruction with carbon ions: OS-SART, slice $z = 36$	69
4.25	Reconstruction with carbon ions: OS-SART, slice $z = 60$	69
4.26	3D representation (a) and sectional views (b) of OS-SART reconstruction of carbon ion CT (created with ImageJ Volume Viewer).	70
6.1	Projections with 10^6 protons at 100 MeV at 0° using different values for $t_{x,y}$ (projections according to Equation (3.14)).	77
6.2	Projections with 10^6 protons at 100 MeV at 45° using different values for $t_{x,y}$ (projections according to Equation (3.14)).	77

6.3	Projections with 10^6 protons at 100 MeV at 90° using different values for $t_{x,y}$ (projections according to Equation (3.14)).	78
6.4	Projections with 10^6 protons at 0° ($t_{x,y} = 1$ mm, projections according to Equation (3.14)).	78
6.5	Projections with 10^6 protons at 45° ($t_{x,y} = 1$ mm, projections according to Equation (3.14)).	79
6.6	Projections with 10^6 protons at 90° ($t_{x,y} = 1$ mm, projections according to Equation (3.14)).	79
6.7	Projections with 10^6 protons at 0° ($t_{x,y} = 1$ mm, projections according to Equation (3.15)).	80
6.8	Projections with 10^6 protons at 45° ($t_{x,y} = 1$ mm, projections according to Equation (3.15)).	80
6.9	Projections with 10^6 protons at 90° ($t_{x,y} = 1$ mm, projections according to Equation (3.15)).	80
6.10	SART with 20 iterations, slice $z = 36$	81
6.11	SART with 20 iterations, slice $z = 60$	81
6.12	OS-SART with 20 iterations and blocksize 10, slice $z = 36$	82
6.13	OS-SART with 20 iterations and blocksize 10, slice $z = 60$	82
6.14	OS-SART with 20 iterations and blocksize 5, slice $z = 36$	83
6.15	OS-SART with 20 iterations and blocksize 5, slice $z = 60$	83
6.16	OS-SART with 20 iterations and blocksize 5, slice $z = 36$	84
6.17	OS-SART with 20 iterations and blocksize 5, slice $z = 60$	84

Acronyms

- ART** Algebraic Reconstruction Technique. 27
- CT** Computed Tomography. 1, 6, 17–20, 23–25, 31, 37, 38, 40, 48, 52, 69, 70, 72, 73, 86
- FBP** Filtered Backprojection. 23, 26, 27, 37, 52
- FDK** Feldkamp, David and Kress. 37, 38, 52–56, 72, 86
- HEPHY** Institute of High Energy PHYSics. 43
- HU** Hounsfield Units. 17, 18
- IR** Irradiation Room. 30
- Linac** Linear Accelerator. 30
- MCS** Multiple Coulomb Scattering. 6, 12, 14, 17, 19, 21, 27
- MLP** Most Likely Path. 1, 22, 23, 72, 85
- OS-SART** Ordered Subset SART. 27, 28, 52, 56–60, 69, 70, 72, 81–84, 86, 87
- RMS** Root-Mean Square. 23, 24, 85
- RSP** Relative Stopping Power. 18, 27
- SART** Simultaneous Algebraic Reconstruction Technique. 27, 28, 52, 54–57, 72, 81–84, 86, 87
- SL** Straight Line. 1, 2, 9, 12, 20–23, 27, 37, 41, 42, 46, 48, 85
- SOBP** Spread-Out Bragg Peak. 15, 16, 85
- WET** Water-Equivalent Thickness. 16, 17

References

- [1] World Health Organization, “Cancer Key Facts.” <https://www.who.int/news-room/fact-sheets/detail/cancer>, 2018. [Online; accessed 11-July-2019].
- [2] International Agency for Research on Cancer, “Latest global cancer data: Cancer burden rises to 18.1 million new cases and 9.6 million cancer deaths in 2018,” 2018.
- [3] M. Durante and H. Paganetti, “Nuclear physics in particle therapy: a review,” *Reports on Progress in Physics*, vol. 79, no. 9, p. 096702, 2016.
- [4] S. C. C. Alliance, “Protons & Childhood Cancer Treatment.” <https://www.sccaprotontherapy.com/cancers-treated/childhood-cancer-treatment>, 2017. [Online; accessed 11-July-2019].
- [5] C. Courier, “European hadron therapy facilities in operation or under construction in 2016.” <https://home.cern/news/news/knowledge-sharing/exploring-future-medical-accelerators-cancer-treatment>, 2018. [Online; accessed 11-July-2019].
- [6] “MedAustron.” <https://www.medaustron.at>, 2018. [Online; accessed 2-July-2019].
- [7] W. D. Newhauser and R. Zhang, “The physics of proton therapy,” *Physics in Medicine & Biology*, vol. 60, no. 8, p. R155, 2015.
- [8] W. Demtröder, *Experimentalphysik. 4. Kern-, Teilchen-und Astrophysik: mit 68 Tabellen, zahlreichen durchgerechneten Beispielen und 104 Übungsaufgaben mit ausführlichen Lösungen*. Springer, 2010.
- [9] Geant4 Collaboration, “Physics reference manual,” *Version: geant4*, vol. 10, no. 9, 2016.
- [10] W. H. Bragg and R. Kleeman, “XXXIX. On the α particles of radium, and their loss of range in passing through various atoms and molecules,” *The London, Edinburgh, and Dublin Philosophical Magazine and Journal of Science*, vol. 10, no. 57, pp. 318–340, 1905.
- [11] R. M. Sternheimer, “The density effect for the ionization loss in various materials,” *Physical Review*, vol. 88, no. 4, p. 851, 1952.
- [12] D. Groom and S. K. LBNL, “27. PASSAGE OF PARTICLES THROUGH MATTER,” 1999.
- [13] M. Thomson, *Modern particle physics*. Cambridge University Press, 2013.
- [14] C. Bopp, *The proton as a dosimetric and diagnostic probe*. PhD thesis, Université de Strasbourg, 2014.

- [15] G. R. Lynch and O. I. Dahl, "Approximations to multiple Coulomb scattering," *Nuclear Instruments and Methods in Physics Research Section B: Beam Interactions with Materials and Atoms*, vol. 58, no. 1, pp. 6–10, 1991.
- [16] W. Levin, H. Kooy, J. Loeffler, and T. DeLaney, "Proton beam therapy," *British journal of Cancer*, vol. 93, no. 8, p. 849, 2005.
- [17] G. Poludniowski, N. Allinson, and P. Evans, "Proton radiography and tomography with application to proton therapy," *The British journal of radiology*, vol. 88, no. 1053, p. 20150134, 2015.
- [18] P. Suetens, *Fundamentals of medical imaging*. Cambridge university press, 2017.
- [19] W. D. Newhauser, J. D. Fontenot, A. Mahajan, D. Kornguth, M. Stovall, Y. Zheng, P. J. Taddei, D. Mirkovic, R. Mohan, J. D. Cox, *et al.*, "The risk of developing a second cancer after receiving craniospinal proton irradiation," *Physics in Medicine & Biology*, vol. 54, no. 8, p. 2277, 2009.
- [20] U. Schneider, E. Pedroni, and A. Lomax, "The calibration of CT Hounsfield units for radiotherapy treatment planning," *Physics in Medicine & Biology*, vol. 41, no. 1, p. 111, 1996.
- [21] D. Wang, T. R. Mackie, and W. A. Tomé, "On the use of a proton path probability map for proton computed tomography reconstruction," *Medical physics*, vol. 37, no. 8, pp. 4138–4145, 2010.
- [22] K. Hanson, J. Bradbury, T. Cannon, R. Hutson, D. Laubacher, R. Macek, M. Paciotti, and C. Taylor, "The application of protons to computed tomography (IEEE Transactions on Nuclear Science)," in *Proceedings of the Nuclear Science Symposium*, 1977.
- [23] R. W. Schulte, V. Bashkirov, M. C. Loss Klock, T. Li, A. J. Wroe, I. Evseev, D. C. Williams, and T. Satogata, "Density resolution of proton computed tomography," *Medical physics*, vol. 32, no. 4, pp. 1035–1046, 2005.
- [24] C. Civinini, D. Bonanno, M. Brianzi, M. Carpinelli, G. Cirrone, G. Cuttone, D. L. Presti, G. Maccioni, S. Pallotta, N. Randazzo, *et al.*, "Proton Computed Tomography: iterative image reconstruction and dose evaluation," *Journal of Instrumentation*, vol. 12, no. 01, p. C01034, 2017.
- [25] R. Zhang, P. J. Taddei, M. M. Fitzek, and W. D. Newhauser, "Water equivalent thickness values of materials used in beams of protons, helium, carbon and iron ions," *Physics in Medicine & Biology*, vol. 55, no. 9, p. 2481, 2010.
- [26] T. M. Buzug, "Computed tomography," in *Springer Handbook of Medical Technology*, pp. 311–342, Springer, 2011.

- [27] T. Li, Z. Liang, J. V. Singanallur, T. J. Satogata, D. C. Williams, and R. W. Schulte, “Reconstruction for proton computed tomography by tracing proton trajectories: A Monte Carlo study,” *Medical physics*, vol. 33, no. 3, pp. 699–706, 2006.
- [28] B. Rossi and K. Greisen, “Cosmic-ray theory,” *Reviews of Modern Physics*, vol. 13, no. 4, p. 240, 1941.
- [29] D. Wang, T. R. Mackie, and W. A. Tomé, “Bragg peak prediction from quantitative proton computed tomography using different path estimates,” *Physics in Medicine & Biology*, vol. 56, no. 3, p. 587, 2011.
- [30] W. Birkfellner, *Applied medical image processing: a basic course*. CRC Press, 2016.
- [31] R. N. Bracewell and A. Riddle, “Inversion of fan-beam scans in radio astronomy,” *The Astrophysical Journal*, vol. 150, p. 427, 1967.
- [32] S. Penfold and Y. Censor, “Techniques in iterative proton CT image reconstruction,” *Sensing and Imaging*, vol. 16, no. 1, p. 19, 2015.
- [33] A. C. Kak, M. Slaney, and G. Wang, “Principles of computerized tomographic imaging,” *Medical Physics*, vol. 29, no. 1, pp. 107–107, 2002.
- [34] “MedAustron Centre.” <https://www.medaustron.at/en/center>, 2018. [Online; accessed 2-July-2019].
- [35] M. Stock, D. Georg, A. Ableitinger, A. Zechner, A. Utz, M. Mumot, G. Kragl, J. Hopfgartner, J. Gora, T. Böhlen, *et al.*, “The technological basis for adaptive ion beam therapy at MedAustron: status and outlook,” *Zeitschrift für Medizinische Physik*, vol. 28, no. 3, pp. 196–210, 2018.
- [36] “MedAustron Technology.” <https://www.medaustron.at/en/technology>, 2018. [Online; accessed 2-July-2019].
- [37] M. Stock, P. Georg, R. Mayer, T. T. Böhlen, and S. Vatnitsky, “Development of clinical programs for carbon ion beam therapy at MedAustron,” *International Journal of Particle Therapy*, vol. 2, no. 3, pp. 474–477, 2015.
- [38] A. Burker, T. Bergauer, A. Hirtl, C. Irmler, S. Kaser, P. Paulitsch, V. Teufelhart, F. Ulrich-Pur, and M. Valenta, “Imaging with ion beams at MedAustron,” *Nuclear Instruments and Methods in Physics Research Section A: Accelerators, Spectrometers, Detectors and Associated Equipment*, 2019. DOI: <https://doi.org/10.1016/j.nima.2019.05.087>.
- [39] A. Burker, “Photo of Experimental Setup at MedAustron,” 2018.
- [40] S. Agostinelli, J. Allison, K. a. Amako, J. Apostolakis, H. Araujo, P. Arce, M. Asai, D. Axen, S. Banerjee, G. . Barrant, *et al.*, “GEANT4—a simulation toolkit,” *Nuclear instruments and methods in physics research section A: Accelerators, Spectrometers, Detectors and Associated Equipment*, vol. 506, no. 3, pp. 250–303, 2003.

- [41] L. L. Carter and E. D. Cashwell, “Particle-transport simulation with the Monte Carlo method,” tech. rep., Los Alamos Scientific Lab., N. Mex.(USA), 1975.
- [42] Geant4 Collaboration, “Book for application developers release 10.5,” *Rev1. 0: March 5th*, 2019.
- [43] R. Brun, A. McPherson, P. Zancarini, M. Maire, and F. Bruyant, “GEANT 3: user’s guide Geant 3.10, Geant 3.11,” tech. rep., CERN, 1987.
- [44] “ROOT a Data analysis Framework.” <https://root.cern.ch>, 2018. [Online; accessed 4-July-2019].
- [45] “CERN NA49 experiment.” <http://na49info.web.cern.ch/na49info/>, 1997. [Online; accessed 4-July-2019].
- [46] R. Brun and F. Rademakers, “ROOT—an object oriented data analysis framework,” *Nuclear Instruments and Methods in Physics Research Section A: Accelerators, Spectrometers, Detectors and Associated Equipment*, vol. 389, no. 1-2, pp. 81–86, 1997.
- [47] R. Brun, F. Rademakers, S. Panacek, I. Antcheva, and D. Buskulic, “The ROOT Users Guide,” *CERN*, <http://root.cern.ch>, 2003.
- [48] “TIGRE/MATLAB at master.” <https://github.com/CERN/TIGRE/tree/master/MATLAB>, 2019. [Online; accessed 3-July-2019].
- [49] “NVIDIA.” <https://www.nvidia.com/de-at/>, 2019. [Online; accessed 27-September-2019].
- [50] J. Sanders and E. Kandrot, *CUDA by example: an introduction to general-purpose GPU programming*. Addison-Wesley Professional, 2010.
- [51] A. Biguri, M. Dosanjh, S. Hancock, and M. Soleimani, “TIGRE: a MATLAB-GPU toolbox for CBCT image reconstruction,” *Biomedical Physics & Engineering Express*, vol. 2, no. 5, p. 055010, 2016.
- [52] R. L. Siddon, “Fast calculation of the exact radiological path for a three-dimensional CT array,” *Medical physics*, vol. 12, no. 2, pp. 252–255, 1985.
- [53] “TIGRE/Python at master.” <https://github.com/CERN/TIGRE/tree/master/Python>, 2019. [Online; accessed 3-July-2019].
- [54] W. Rasband, “ImageJ: Image processing and analysis in Java,” *Astrophysics Source Code Library*, 2012.
- [55] T. Ferreira and W. Rasband, “ImageJ user guide,” *ImageJ/Fiji*, vol. 1, pp. 155–161, 2012.

- [56] J. Schindelin, I. Arganda-Carreras, E. Frise, V. Kaynig, M. Longair, T. Pietzsch, S. Preibisch, C. Rueden, S. Saalfeld, B. Schmid, *et al.*, “Fiji: an open-source platform for biological-image analysis,” *Nature methods*, vol. 9, no. 7, p. 676, 2012.
- [57] S. Kaser, “Validation of Detector Misalignment using Geant4 Simulations and EU-Telescope,” 2018.
- [58] “Pololu Mounting hub.” <https://www.pololu.com/product/1079>, 2019. [Online; accessed 3-July-2019].
- [59] G. A. P. Cirrone, M. Bucciolini, M. Bruzzi, G. Candiano, C. Civinini, G. Cuttone, P. Guarino, D. L. Presti, S. E. Mazzaglia, S. Pallotta, *et al.*, “Monte Carlo evaluation of the Filtered Back Projection method for image reconstruction in proton computed tomography,” *Nuclear Instruments and Methods in Physics Research Section A: Accelerators, Spectrometers, Detectors and Associated Equipment*, vol. 658, no. 1, pp. 78–83, 2011.
- [60] M. Berger, J. Coursey, M. Zucker, and J. Chang, “Stopping-power and range tables for electrons, protons, and helium ions, NIST Standard Reference Database 124,” 2017.
- [61] P. Yepes, S. Randeniya, P. J. Taddei, and W. D. Newhauser, “Monte Carlo fast dose calculator for proton radiotherapy: application to a voxelized geometry representing a patient with prostate cancer,” *Physics in Medicine & Biology*, vol. 54, no. 1, p. N21, 2008.